Separation and Purification Technology 355 (2025) 129553

Contents lists available at ScienceDirect

Separation and Purification Technology

journal homepage: www.elsevier.com/locate/seppur

Non-Idealities in adsorption thermodynamics for CO_2 capture from humid natural gas using CALF-20

Rajamani Krishna *, Jasper M. van Baten

Van 't Hoff Institute for Molecular Sciences University of Amsterdam, Science Park 904, 1098 XH Amsterdam, the Netherlands

ARTICLE INFO

Keywords:
CO_2 capture
Natural gas
Relative humidity
Thermodynamic non-idealities
Segregated adsorption
Hydrogen bonding
Activity coefficients

ABSTRACT

The focus of this article is on CO_2 capture from natural gas under humid conditions using CALF-20. Configurational-Bias Monte Carlo (CBMC) simulations are used to investigate adsorption of $CO_2/CH_4/H_2O$ mixtures in CALF-20 with varying relative humidities in the bulk gas phase. The CBMC simulations reveal that the mixture adsorption equilibrium shows strong deviations from the estimations of the Ideal Adsorbed Solution Theory (IAST). CBMC simulations for mixture adsorption of the constituent binary pairs, CH_4/H_2O, and CO_2/H_2O, reveal that the origin of thermodynamic non-idealities stem from segregated nature of the adsorbed phase and inhomogeneous distribution of guest adsorbates within the pore landscape of CALF-20. The extent and nature of the segregation depends strongly on the % relative humidity of the bulk gas mixture.

The important message that emerges from this investigation is the need to incorporate the Real Adsorbed Solution Theory (RAST) for quantitative modelling of fixed-bed adsorbers in natural gas purification with CALF-20.

1. Introduction

The use of zinc-based Calgary Framework 20 (CALF-20) for CO_2 capture from humid flue gases has garnered a lot of attention in the published literature [1–6]. More recently, Peng et al. [7] have demonstrated the efficacy of CALF-20 to purify C_2H_4 from a seven-component cracking gas mixture (C_2H_4, C_2H_2, C_2H_6, CO_2, C_3H_4, C_3H_6, and C_3H_8) by one-step separation even under conditions of 74 % relative humidity. Based on the unary isotherm data of Peng et al. [7] (see Figure S1), it appears that CALF-20 has the potential for CO_2 capture from natural gas streams. For natural gas purification, CALF-20 should be expected to provide stiff competition to other reported MOFs [8–15], especially under humid conditions. The primary objective of this article is to investigate the salient aspects of CO_2 capture from natural gas, taken to be primarily CH_4, under varying conditions of relative humidity.

Towards this end, Configurational-Bias Monte Carlo (CBMC) simulations for adsorption of $CO_2/H_2O/CH_4$ mixtures in pristine CALF-20 crystals were undertaken. The simulation methodologies are the same as detailed in earlier publications [16–22]. The CALF-20 structure was considered to be rigid in the simulations. The unit cell dimensions of CALF-20 crystals are $a = 8.9138$ Å; $b = 9.6935$ Å; $c = 9.4836$ Å with angles $\alpha = 90°$; $\beta = 115.895°$; $\gamma = 90°$; see pore landscape in Figure S2. The simulation box for conducting CBMC simulations consisted of $5 \times 3 \times 5 = 75$ unit cells. The interactions between adsorbed molecules are described with Lennard-Jones terms together with electrostatic interactions. For the atoms in the host metal organic framework (see Figure S3), the generic DREIDING [23] force fields were used. The framework atomic charges are from Gopalsamy et al.[4]; see Table S1.

CH_4 molecules are described with a united atom model, in which each molecule is treated as a single interaction center [24,25]. CO_2 was described by a 3-site charged Lennard-Jones model as reported by Garcia-Sánchez et al. [26]. Water is modeled using the four-site TIP4P-Ew potential [27]; TIP4P=4-site transferable intermolecular potential (TIP4P) and Ew = Ewald technique. Further simulation details are provided in the Supplementary Material.

2. CBMC simulations of mixture adsorption equilibrium

Fig. 1a presents the CBMC simulations for unary isotherms for CO_2, H_2O, and CH_4. The continuous solid lines are unary isotherm fits; the parameters are provided in Table S2. Particularly noteworthy is the steepness of the unary water isotherm, that is indicative of strong hydrogen bonding between molecule pairs [28]. Fig. 1b presents component loadings, q_i, for $CO_2(1)/CH_4(2)$ mixture adsorption in CALF-20 at 298 K with varying total fugacity f_t, maintaining the mole fraction

* Corresponding author.
E-mail address: r.krishna@uva.nl (R. Krishna).

https://doi.org/10.1016/j.seppur.2024.129553
Received 30 July 2024; Received in revised form 25 August 2024; Accepted 4 September 2024
Available online 7 September 2024

Nomenclature

Latin alphabet

A	surface area per kg of framework, m^2 kg^{-1}
c_i	molar concentration of species i, mol/m^{-3}
c_{i0}	molar concentration of species i in fluid mixture at inlet to adsorber, mol/m^{-3}
C	constant used in eq (3), kg mol^{-1}
f_i	partial fugacity of species i, Pa
f_t	total fugacity of bulk gas phase mixture, Pa
G^{ex}	excess Gibbs free energy, J/mol
m_{ads}	mass of adsorbent packed in fixed bed, kg
p_2^{sat}	saturation vapor pressure of water, Pa
P_i^0	sorption pressure, Pa
q_i	component molar loading of species i, mol kg^{-1}
Q_0	volumetric flow rate of gas mixture at inlet to fixed bed, m^3/s
%RH	% relative humidity, dimensionless
R	gas constant, 8.314 J/mol K^{-1}
$S_{ads} = \frac{q_1/q_2}{f_1/f_2}$	adsorption selectivity, dimensionless
t	time, s
T	absolute temperature, K
x_i	mole fraction of species i in adsorbed phase, dimensionless
y_i	mole fraction of species i in bulk fluid mixture, dimensionless

Greek alphabet

α	NRTL parameters, dimensionless
γ_i	activity coefficient of component i in adsorbed phase, dimensionless
π	spreading pressure, N/m
τ_{ij}	NRTL parameters, dimensionless
Φ	surface potential, mol kg^{-1}

of CO_2 in the bulk gas mixture at a constant value $y_2 = f_2/f_t = 0.05$. The dashed lines are the IAST estimations of the component loadings. The corresponding values of the adsorption selectivity, $S_{ads} = \frac{q_1/q_2}{f_1/f_2}$, plotted as function of the bulk gas phase fugacity, f_t, in Fig. 1c. The dashed lines in Fig. 1b,c are the IAST estimates; these estimates are in good agreement with the CBMC data.

We now turn our attention to CO_2 capture from humid gas mixtures. Fig. 2a presents CBMC simulations of component loadings, q_i, for $CO_2(1)/H_2O(2)/CH_4(3)$ mixture adsorption in CALF-20 at 298 K at a total fugacity $f_t = f_1 + f_2 + f_3 = 500$ kPa and partial fugacity of $CH_4(3)$ $f_3 = 400$ kPa, plotted as a function of % RH = % Relative Humidity $= \frac{f_2}{p_2^{sat}} \times 100$ where f_2 is the partial fugacity of water in the bulk gas phase, and p_2^{sat} is the saturation vapor pressure of water. At 298 K, p_2^{sat} is determined from the Antoine equation: $p_2^{sat} = 3150$ Pa. The mole fraction of H_2O in the bulk gas mixture, $y_2 = f_2/f_t$, is varied. Fig. 2b,c,d plots the mole fractions of CO_2, H_2O, and CH_4 in the adsorbed phase mixture, x_i, as a function of % RH. The dashed lines are the IAST estimations. The steepness of the uptakes at % RH $\approx$ 38% is caused by corresponding sharpness in the unary water isotherm (cf. Fig. 1a). We note that for % RH $<$ 38%, the adsorbed phase is considerably richer in both $CO_2(1)$, and $CH_4(3)$ but poorer in $H_2O(2)$ than anticipated by the IAST. In contrast, for % RH $>$ 38% , the adsorbed phase is considerably poorer in both $CO_2(1)$, and $CH_4(3)$ but richer in $H_2O(2)$ than anticipated by the IAST, implying the suppression of CO_2, and CH_4 uptakes due to presence of H_2O in the adsorbed phase.

The CBMC mixture simulation data in Fig. 1 and Fig. 2 would lead us to conclude that it is the presence of H_2O is in the bulk gas phase mixture that is the root cause of thermodynamic non-idealities. To investigate the origins of thermodynamic non-idealities, we also examined adsorption of the constituent binary CH_4/H_2O and CO_2/H_2O mixtures.

Fig. 3a shows CBMC simulations of component loadings, q_i, for $CH_4(1)/H_2O(2)$ mixture adsorption in CALF-20 at 298 K at a total fugacity = 500 kPa. The mole fraction of H_2O in the bulk gas mixture, $y_2 = f_2/f_t$, is varied. The loadings are plotted against % RH. The IAST estimates of the component loadings are indicated by the dashed lines. We note that the CH_4/H_2O binary mixture adsorption exhibits significant departures from thermodynamic idealities. Noteworthily, the activity coefficients of both components in the adsorbed phase exceed unity, $\gamma_i > 1$ (see Fig. 3c); this characteristics is distinctly different for non-idealities for CO_2 capture in cation-exchanged zeolites, such as NaX and LTA-4A, for which the activity coefficients, $\gamma_i < 1$; see published works [29–32].

Another way to demonstrate the non-idealities is to plot the mole fraction of CH_4 in the adsorbed phase mixture, $x_1 = \frac{q_1}{q_t}$; $q_t = q_1 + q_2$ as a function of the % RH; see Fig. 3b. We note that for % RH $<$ 33%; $x_1 > 0.2$, the adsorbed phase mixture is richer in CH_4, i.e. poorer in H_2O, than is anticipated by the IAST. On the other hand, for % RH $>$ 33%; $x_1 < 0.2$, the adsorbed phase mixture is poorer in CH_4, i.e. richer in H_2O, than is anticipated by the IAST.

The IAST description of mixture adsorption equilibrium relies on a number of basic tenets [6,29–35]: (a) homogeneous distribution of guest adsorbates, (b) no preferential locations of any guest species within the pore landscape, and (c) adsorption enthalpies and surface areas of the adsorbed molecules do not change upon mixing with other guests. The occurrence of molecular clustering and hydrogen bonding should be expected to invalidate tenet (c) because the surface area occupied by a molecular cluster is different from that of each of the un-clustered guest molecules in the adsorbed phase.

To investigate the possibility of non-homogeneous distribution of adsorbate guests, CBMC simulation data on the spatial locations of the guest molecules were sampled to determine the inter-molecular distances; these distances are determined from the center of gravity of each guest molecule. By sampling a total of 10^6 simulation steps, the radial distribution functions (RDF) were determined for CH_4-CH_4, CH_4-H_2O, and H_2O-H_2O separation distances. Fig. 4a,b plots the RDFs of center-to-center distances of molecular pairs of guest CH_4 and H_2O pairs in CALF-20 at 298 K; the total fugacity in the bulk gas phase is 500 kPa with partial fugacities $f_1 = 499.1$ kPa, and $f_2 = 0.9$ kPa, and $y_2 = \frac{f_2}{f_1+f_2} = 0.0018$.

If we compare the first peaks, it is noteworthy that H_2O-H_2O pairs are close together at typical distances of about 3 Å. The CH_4-CH_4 pairs are typically 6.5 Å apart, occupying adjacent adsorption sites of CALF-20. The CH_4-H_2O pairs are typically 8 Å apart, occupying adjacent adsorption sites. This implies that the CH_4 molecules face a less severe competitive adsorption with H_2O than is anticipated by the IAST. The

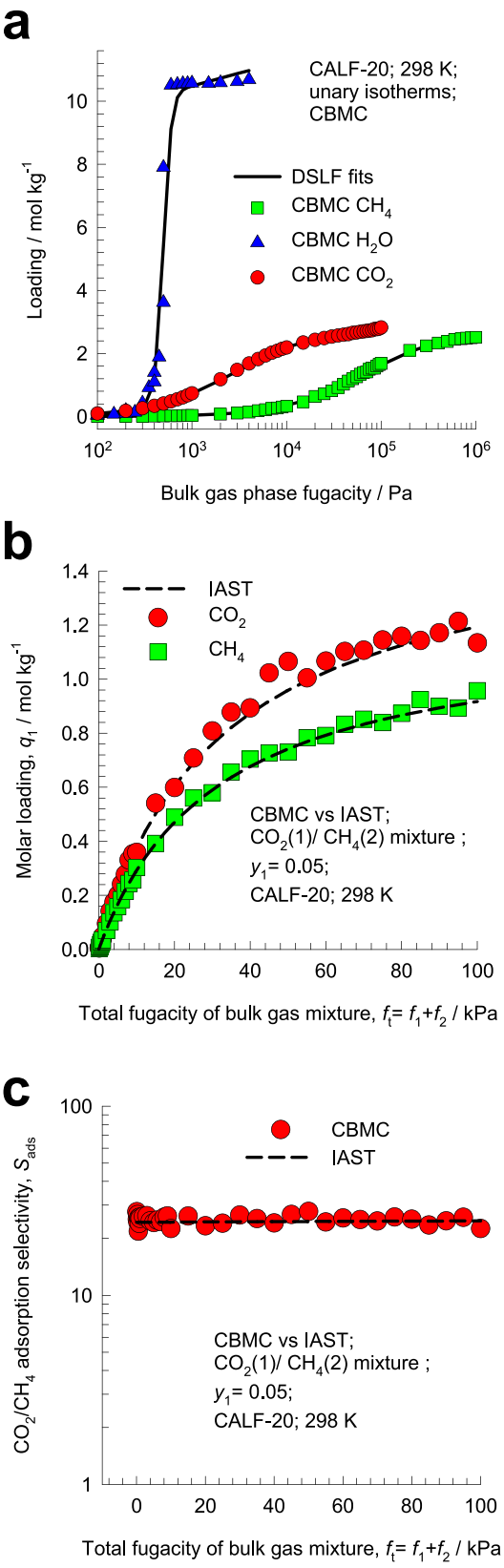

Fig. 1. (a) CBMC simulations of unary isotherms for CO_2, H_2O, and CH_4. The continuous solid lines are unary isotherm fits; the parameters are provided in Table S2. (b) Component loadings, q_i, for $CO_2(1)/CH_4(2)$ mixture adsorption in CALF-20 at 298 K with varying total fugacity f_t, maintaining the mole fraction of CO_2 in the bulk gas mixture at a constant value $y_2 = f_2/f_t = 0.05$. The dashed lines are the IAST estimations of the component loadings. (c) The adsorption selectivity, $S_{ads} = \frac{q_1/q_2}{f_1/f_2}$, plotted as function of the bulk gas phase fugacity, f_t. All calculation details and input data are provided in the Supplementary Material accompanying this publication.

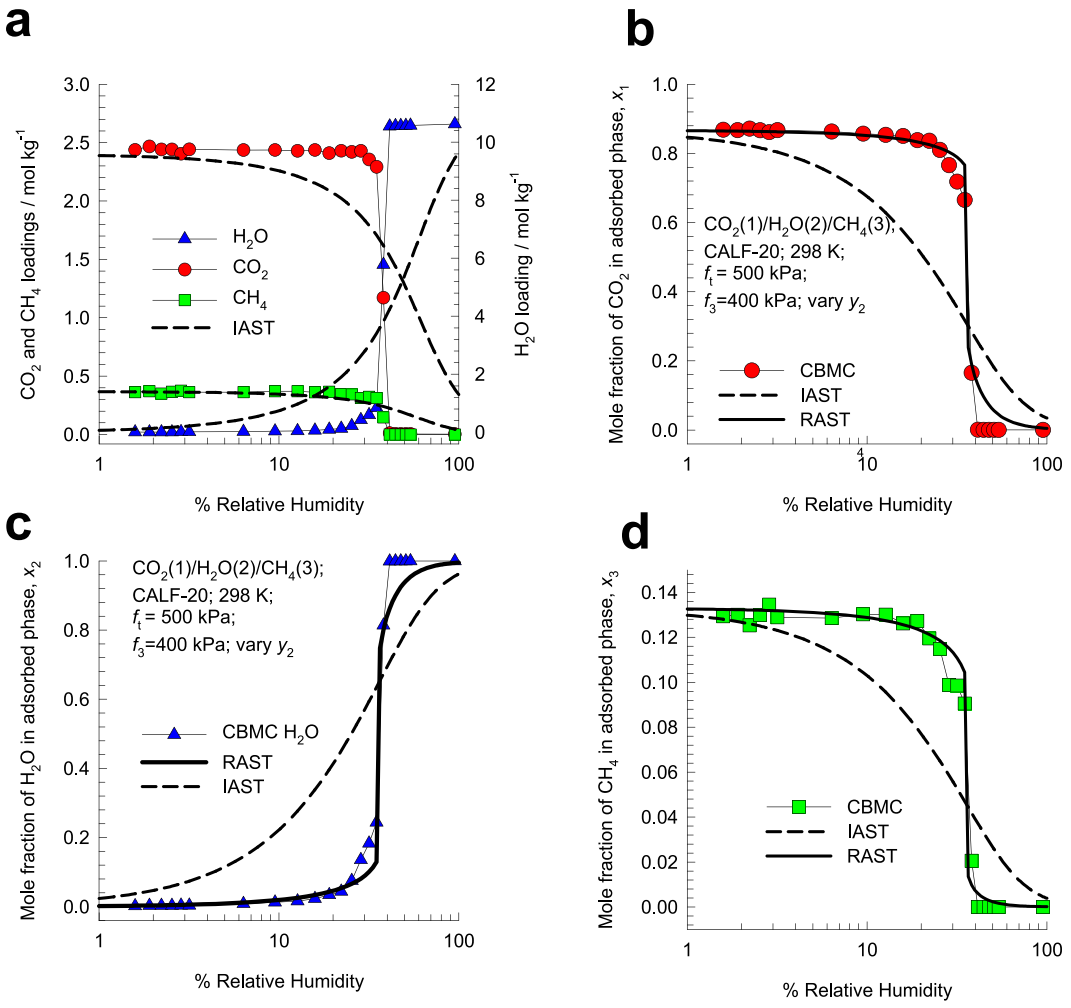

Fig. 2. (a) CBMC simulations of component loadings, q_i, for $CO_2(1)/H_2O(2)/CH_4(3)$ mixture adsorption in CALF-20 at 298 K at a total fugacity $f_t = f_1 + f_2 + f_3 =$ 500 kPa, and partial fugacity $CH_4(3)$ $f_3 =$ 400 kPa, of plotted as a function of % RH. The mole fraction of H_2O in the bulk gas mixture, $y_2 = f_2/f_t$, is varied. (b, c, d) Plot of the mole fractions of CO_2, H_2O, and CH_4 in the adsorbed phase mixture, x_i, as a function of % RH. The dashed lines are the IAST estimations.

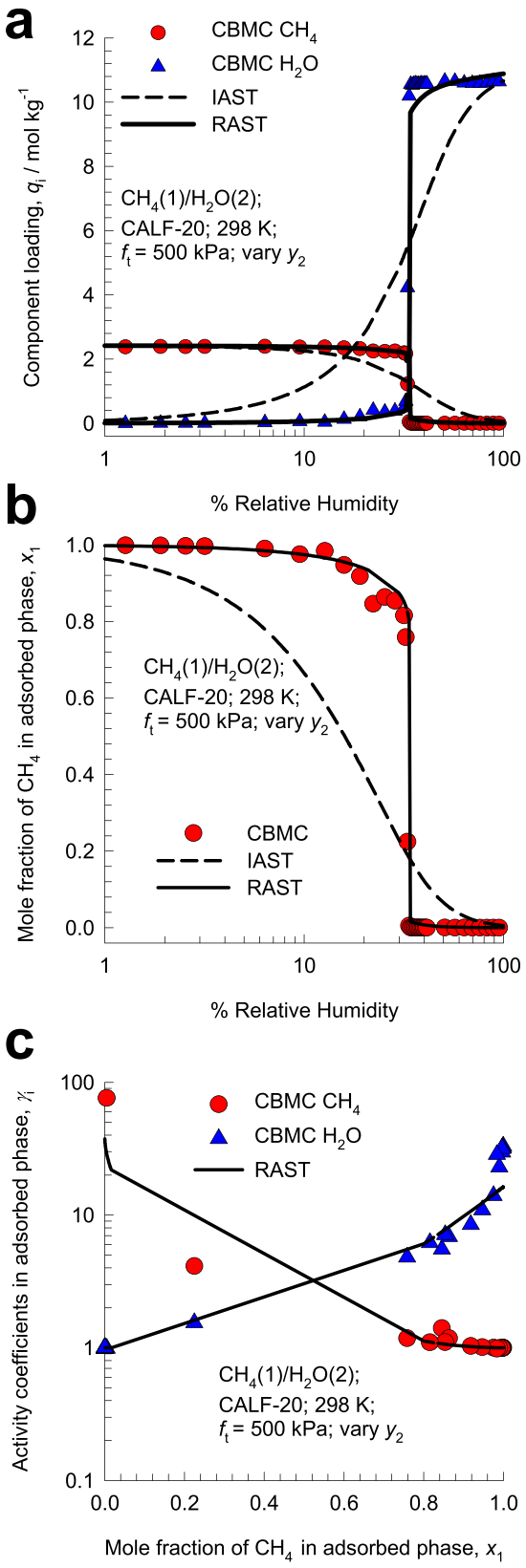

Fig. 3. (a) CBMC simulations of component loadings, q_i, for $CH_4(1)/H_2O(2)$ mixture adsorption in CALF-20 at 298 K at a total fugacity $f_t = 500$ kPa, plotted as a function of % RH. The mole fraction of H_2O in the bulk gas mixture, $y_2 = f_2/f_t$, is varied. (b) Plot of the mole fraction of CH_4 in the adsorbed phase mixture, x_1, as a function of the % RH. (c) Plot of the activity coefficients in the adsorbed phase mixture, γ_i, as a function of the mole fraction of CH_4 in the adsorbed phase mixture, x_1. The continuous solid lines are the RAST calculations; the dashed lines are the IAST estimations. All calculation details and input data are provided in the Supplementary Material accompanying this publication.

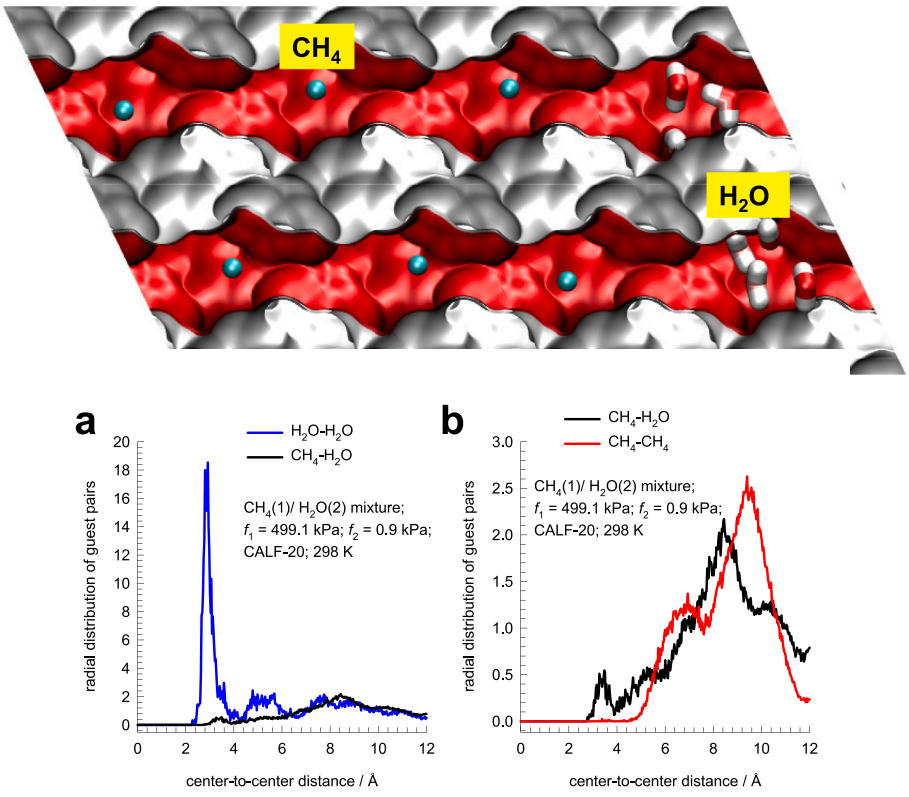

Fig. 4. (a, b) Radial Distribution Function (RDF) of center-to-center distances of CH_4-CH_4, CH_4-H_2O, and H_2O-H_2O pairs, determined from CBMC simulations for adsorption of $CH_4(1)/H_2O(2)$ mixture adsorption in CALF-20 at 298 K. guest CH_4 and H_2O molecules in CALF-20 at at 298 K. total fugacity in the bulk gas phase is 500 kPa with partial fugacities $f_1 = 499.1$ kPa, and $f_2 = 0.9$ kPa. The plotted RDF data has been normalized such that the area under each of the curves is identical to one another.

segregated nature of adsorbate locations is evident in the computational snapshots in Fig. 4. This explains the finding in Fig. 3b that % RH $<$ 33%; $x_1 > 0.2$, i.e. the adsorbed phase mixture is richer in CH_4 than is anticipated by the IAST; this is a direct consequence of the fact that CH_4 faces negligible competition with H_2O.

To investigate the reasons behind the fact that in Fig. 3b with % RH $>$ 33%; $x_1 < 0.2$, the adsorbed phase mixture is poorer in CH_4 than is anticipated by the IAST, we determined the RDF for center-to-center and O···H distances for adsorption of $CH_4(1)/H_2O(2)$ mixture adsorption; the total fugacity in the bulk gas phase is 500 kPa with partial fugacities $f_1 = 498.96$ kPa, and $f_2 = 1.04$ kPa. and $y_2 = 0.00208$.

Fig. 5a presents the data on RDF for center-to-center distances of CH_4-H_2O, and H_2O-H_2O pairs. We note that the first peaks for both CH_4-H_2O, and H_2O-H_2O pairs occur at distances of about 3 Å. This implies that CH_4 faces stiffer competitive adsorption with partner H_2O molecules because of the preponderance of H_2O within the framework; see snapshots in Fig. 5.

Fig. 5b presents the data on RDF for O···H distances of H_2O-H_2O pairs. We note the first peak in the RDFs for H_2O-H_2O pairs occurs at a distance of 2 Å, that is characteristic of hydrogen bonding [28,36]. Strong hydrogen bonding manifests for H_2O-H_2O pairs and serves to suppress the uptake of CH_4 below values anticipated by the IAST that does not cater for molecular clustering due to hydrogen bonding. This explains the fact that for % RH $>$ 33%; $x_1 < 0.2$, the adsorbed phase mixture is poorer in CH_4 than is anticipated by the IAST.

3. The RAST for mixture adsorption equilibrium

To quantify the deviations from the IAST, the activity coefficients of the guest components, γ_i, are determined from

$$\gamma_i = \frac{f_i}{P_i^0 x_i} \tag{1}$$

In eq (1), P_i^0 are the sorption pressures which yields the same spreading pressure, π for each of the pure components, as that for the n-component mixture:

$$\frac{\pi A}{RT} \equiv \Phi = \int_0^{p_1^0} \frac{q_1^0(f)}{f} df = \int_0^{p_2^0} \frac{q_2^0(f)}{f} df = \ldots = \int_0^{p_n^0} \frac{q_n^0(f)}{f} df \tag{2}$$

In Eq. (2), $q_i^0(f)$ is the *pure* component adsorption isotherm. The quantity A is the surface area per kg of framework, with units of m^2 per kg of the framework of the crystalline material; since the surface area A is not directly accessible from experimental data, the surface potential, Φ, with the units mol kg^{-1}, serves as a convenient and practical proxy for the spreading pressure π [37–40].

The continuous solid lines in Fig. 3 are the RAST calculations using NRTL model fits of the activity coefficients of each component

$$\ln(\gamma_i) = \left[\frac{\sum_{j=1}^n x_j \tau_{ji} G_{ji}}{\sum_{k=1}^n x_k G_{ki}} + \sum_{j=1}^n \frac{x_j G_{ij}}{\sum_{k=1}^n x_k G_{kj}} \left(\tau_{ij} - \frac{\sum_{l=1}^n x_l \tau_{lj} G_{lj}}{\sum_{k=1}^n x_k G_{kj}}\right)\right] (1 - \exp(-C\Phi))$$

$$G_{ij} = \exp(-\alpha_{ij}\tau_{ij});\ \alpha_{ij} = \alpha_{ji};\ \tau_{ii} = 0;\ G_{ii} = 1 \tag{3}$$

The values of the fitted NRTL parameters C; τ_{12}; τ_{21}; $\alpha_{12} = \alpha_{21}$ are tabulated in Table S3. The inclusion of the correction factor $(1 - \exp(-C\Phi))$ imparts the correct limiting behaviors for the activity coefficients in the Henry regime at vanishingly small pore occupancies

$$\Phi \to 0; \quad \gamma_i \to 1 \tag{4}$$

Our earlier works [6,34] have underscored the need for including the correction factor $(1 - \exp(-C\Phi))$ in RAST modelling, though this

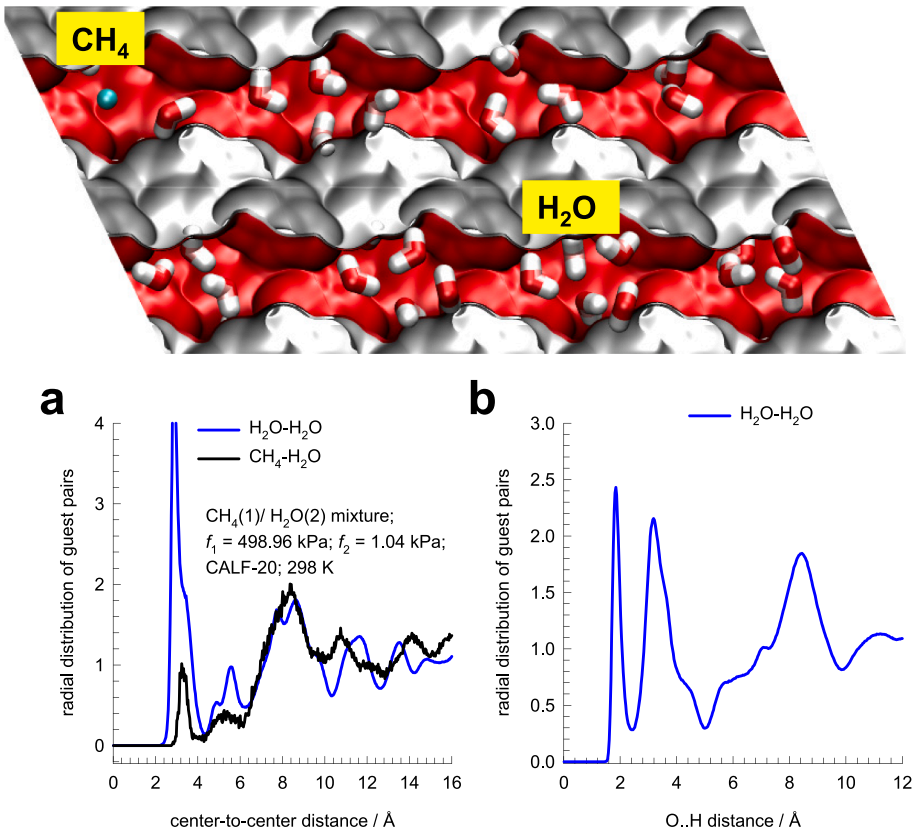

Fig. 5. Radial Distribution Function (RDF) of (a) center-to-center distances, and (b) O···H of CH_4-H_2O, and H_2O-H_2O pairs, determined from CBMC simulations for adsorption of $CH_4(1)/H_2O(2)$ mixture adsorption in CALF-20 at 298 K. The total fugacity in the bulk gas phase is 500 kPa with partial fugacities $f_1 = 498.96$ kPa, and $f_2 = 1.04$ kPa. The plotted RDF data has been normalized such that the area under each of the curves is identical to one another.

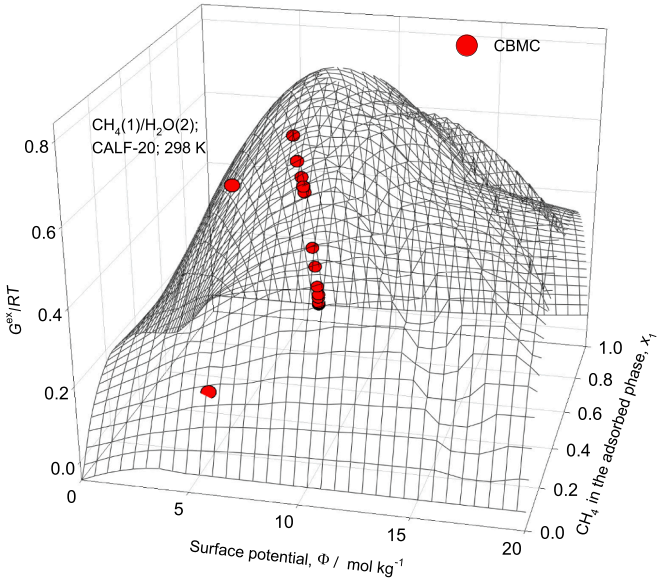

Fig. 6. 3D plots of CBMC data on excess Gibbs free energy G^{ex}/RT for $CH_4(1)/H_2O(2)$ mixture adsorption in CALF-20 at a total fugacity $f_t = 500$ kPa, plotted as function of the surface potential, Φ, and the mole fraction of CH_4 in the adsorbed phase mixture, x_1. The 3D mesh is constructed using the NRTL parameters provided in Table S3.

correction is often ignored in many published works [41–44].

To underscore the need for the correction factor, the CBMC data in Fig. 3 are used to determine the excess Gibbs free energy

$$\frac{G^{ex}}{RT} = x_1 \ln(\gamma_1) + x_2 \ln(\gamma_2) \tag{5}$$

The CBMC values are plotted in 3D space as function of Φ and x_1; see Fig. 6. The CBMC data set resides on a 3D surface mesh determined from the fitted NRTL parameters in Table S3. The 3D surface plot clearly shows that $\Phi \to 0$; $\gamma_i \to 1$; $G^{ex}/RT \to 0$. Also, for a fixed value of the surface potential, Φ we have the limiting characteristics: $x_i \to 1$; $\gamma_i \to 1$ $G^{ex}/RT \to 0$.

Fig. 7a,b shows CBMC simulations of component loadings, q_i, and adsorbed phase mole fractions of CO_2, x_1, for $CO_2(1)/H_2O(2)$ mixture adsorption in CALF-20 at 298 K at a total fugacity = 15 kPa. The dashed lines in Fig. 7a are the IAST estimations. We note that for % RH < 20%; $y_2 < 0.05$; $x_1 > 0.3$, the adsorbed phase mixture is richer in CO_2, i.e. poorer in H_2O, than is anticipated by the IAST. On the other hand, for % RH > 20%; $y_2 > 0.05$; $x_1 < 0.3$, the adsorbed phase mixture is poorer in CO_2, i.e. richer in H_2O, than is anticipated by the IAST. The explanations for the failure of the IAST are precisely analogous to those provided in the foregoing for CH_4/H_2O mixture adsorption, as detailed elsewhere [6]. The continuous solid lines in Fig. 7a,b are RAST calculations with NRTL parameters listed in Table S3.

Additionally, CBMC simulations for $CO_2(1)/H_2O(2)$ mixture adsorption in CALF-20 at 298 K were determined for varying total fugacity f_t, maintaining the mole fraction of H_2O in the bulk gas mixture at a constant value $y_2 = f_2/f_t = 0.05$. Fig. 8 presents 3D plots of CBMC data on excess Gibbs free energy $\frac{G^{ex}}{RT}$ for $CO_2(1)/H_2O(2)$ mixture

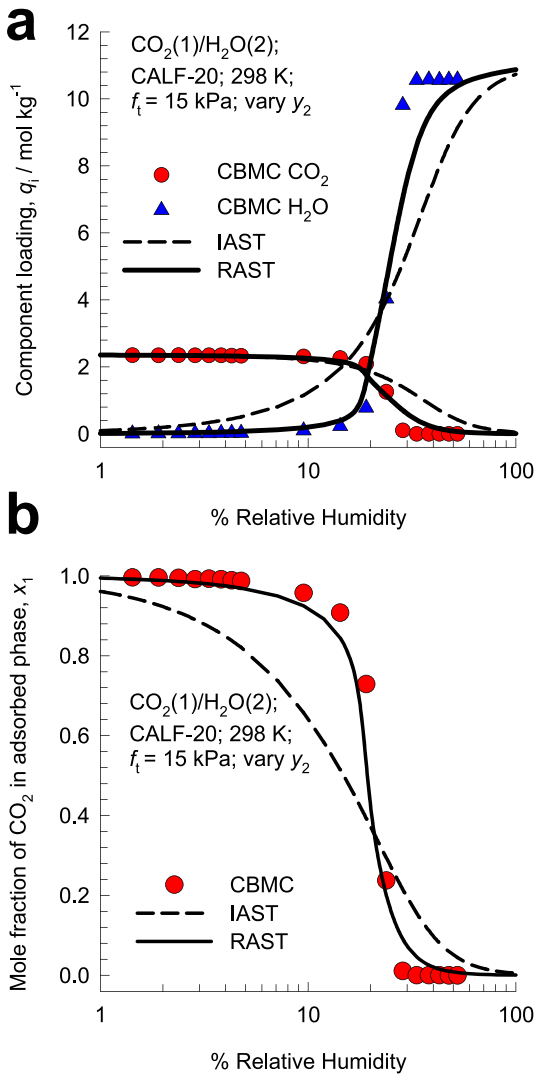

Fig. 7. (a) CBMC simulations of component loadings, q_i, for $CO_2(1)/H_2O(2)$ mixture adsorption in CALF-20 at 298 K at a total fugacity $f_t = 15$ kPa, plotted as a function of % RH. (b) Plot of the mole fraction of CO_2 in the adsorbed phase mixture, x_1, as a function of the % RH. The continuous solid lines are the RAST calculations; the fitted NRTL parameters are specified in Table S3. The dashed lines are the IAST estimations. All calculation details and input data are provided in the Supplementary Material accompanying this publication.

adsorption in CALF-20 at 298 K for two different campaigns, plotted as function of the surface potential, Φ, and the mole fraction of CO_2 in the adsorbed phase mixture, x_1. The 3D mesh is constructed using the NRTL parameters provided in Table S3. Both CBMC campaigns rest on the 3D surface mesh, underscoring the dependence of $\frac{G^{ex}}{RT}$ on both Φ, and x_1.

The continuous solid lines in Fig. 2b,c,d are the RAST calculations using eq (3) in which the NRTL parameters for the constituent binary pairs $\tau_{ij}, \tau_{ji}, \alpha_{ij} = \alpha_{ji}$ are taken from the fitted values for the constituent binary pairs: $CO_2(1)/H_2O(2)$, and $H_2O(2)/CH_4(3)$. Noteworthily, since the binary $CO_2(1)/CH_4(3)$ behaves ideally (cf. Fig. 1), we assert that $\tau_{13} = 0; \quad \tau_{31} = 0$. The ternary NRTL model provides a reasonably good estimation of the mole fractions of the three guests in the adsorbed phase as function of the % RH.

4. RAST modelling of transient breakthroughs in fixed-bed adsorber

To underscore the significance of thermodynamic non-idealities in the transient breakthroughs in fixed bed adsorbers, transient break-

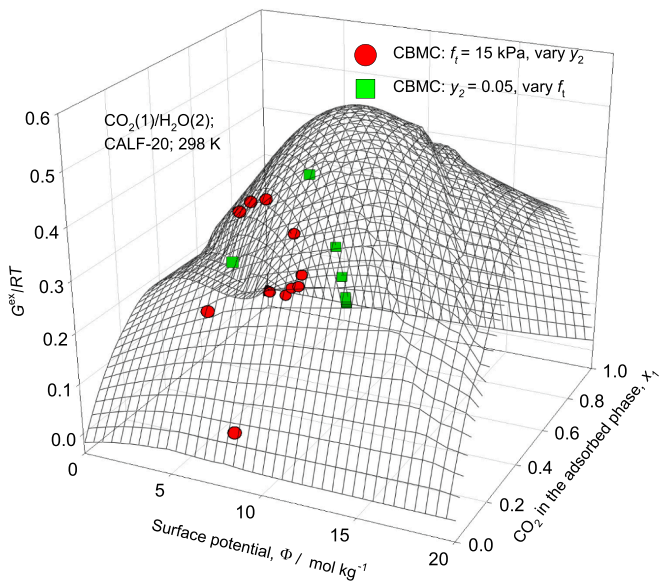

Fig. 8. 3D plots of CBMC data on excess Gibbs free energy G^{ex}/RT for $CO_2(1)/H_2O(2)$ mixture adsorption in CALF-20 at 298 K for two different campaigns, plotted as function of the surface potential, Φ, and the mole fraction of CO_2 in the adsorbed phase mixture, x_1. The 3D mesh is constructed using the NRTL parameters provided in in Table S3.

through simulations were performed for separation of humid gaseous mixtures, using the methodology described in earlier works [45–48]; the details are summarized in the Supplementary Material. Our earlier work [6] provides validation of the simulations methodology by comparison with experimental breakthrough data of Nguyen et al.[2] on the influence of % RH on transient CO_2/H_2O mixture breakthroughs in a laboratory scale fixed bed packed with CALF-20 composites (80 % MOF:20 % polysulfone).

Fig. 9a,b,c compares breakthrough simulations using RAST (continuous colored lines) and IAST (dashed lines) for CH_4/H_2O mixtures at 298 K and total fugacity $f_t = 500$ kPa, with three different values of % RH. The transient breakthrough data for the dimensionless concentrations at the exit of the fixed bed, c_i/c_{i0}, are plotted as a function of a modified time parameter defined by

$$\frac{(Q_0 \ = \ \text{flow rate L s}^{-1}) \times (\text{time in s})}{(\text{kg CALF-20 packed in tube})} = \frac{Q_0 t}{m_{ads}} = \text{L kg}^{-1} \tag{6}$$

Noteworthily, the breakthrough characteristics of H_2O are particularly sensitive to thermodynamic non-idealities. To accentuate the differences between the IAST and RAST calculations of breakthroughs, the spatially-averaged component loadings in the bed are plotted in Fig. 9d, e,f as function of $\frac{Q_0 t}{m_{ads}}$. For % RH = 5 %, and 25 % the RAST anticipates the adsorbed phase to be significantly richer in CH_4, i.e. poorer in H_2O, than predicted by the IAST. For % RH = 40 %, the RAST anticipates the adsorbed phase to be significantly poorer in CH_4, i.e. richer in H_2O, than predicted by the IAST. These findings are consistent with the data plotted in Fig. 3.

Fig. 10 compares breakthrough simulations using RAST (continuous colored lines) and IAST (dashed lines) for CO_2/H_2O mixtures at 298 K and total fugacity $f_t = 100$ kPa, with three different values of % Relative Humidity. For % RH = 5 %, and 25 % the RAST anticipates the adsorbed phase to be significantly richer in CO_2, i.e. poorer in H_2O, than predicted by the IAST. For % RH = 40 %, the RAST anticipates the adsorbed phase to be significantly poorer in CO_2, i.e. richer in H_2O, than predicted by the IAST. These findings are consistent with the data plotted in Fig. 7.

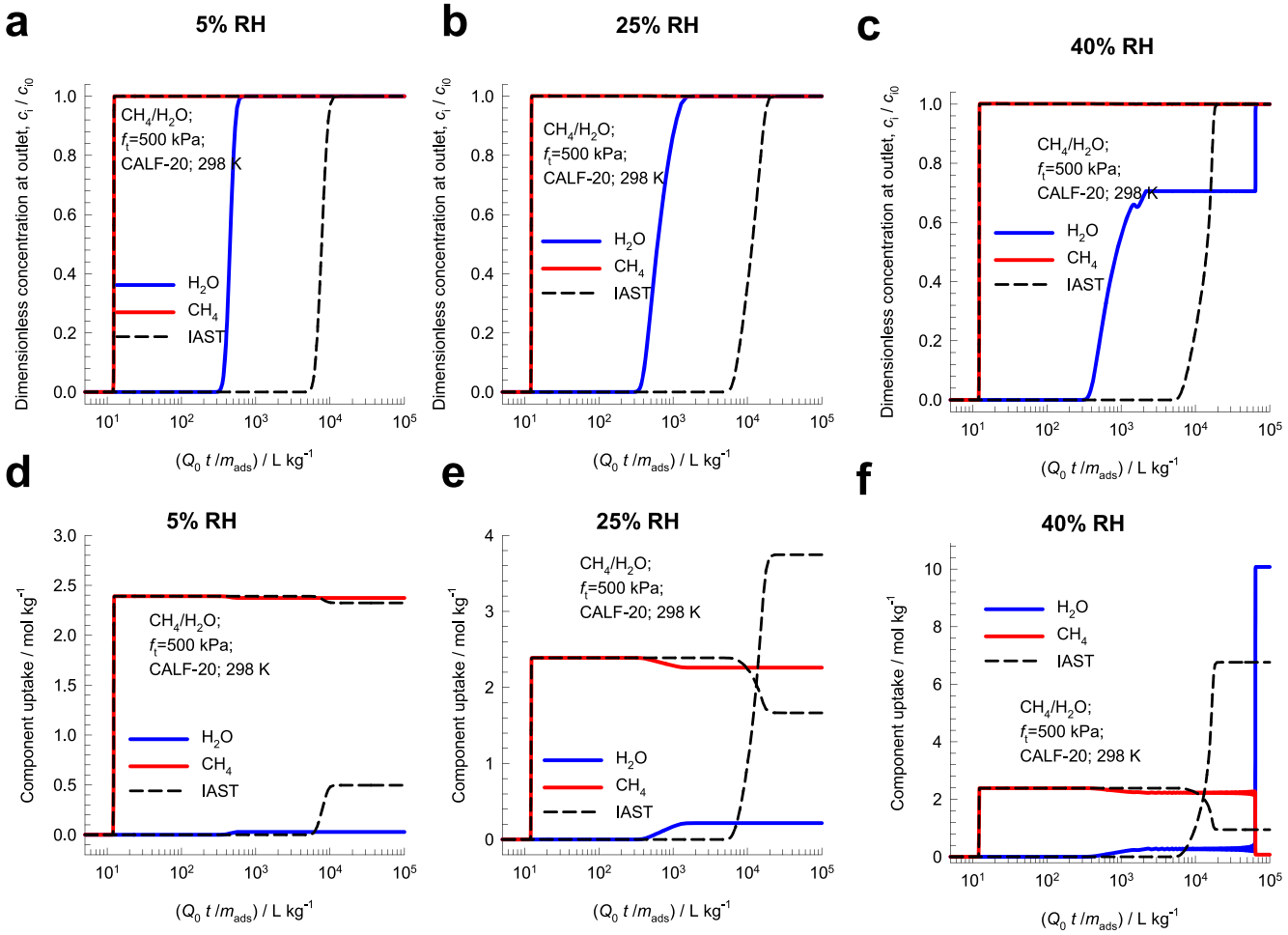

Fig. 9. Comparison of breakthrough simulations using RAST (continuous colored lines) and IAST (dashed lines) for CH_4/H_2O mixtures at a total fugacity = 500 kPa, and temperature 298 K. Three different values of % RH are considered.

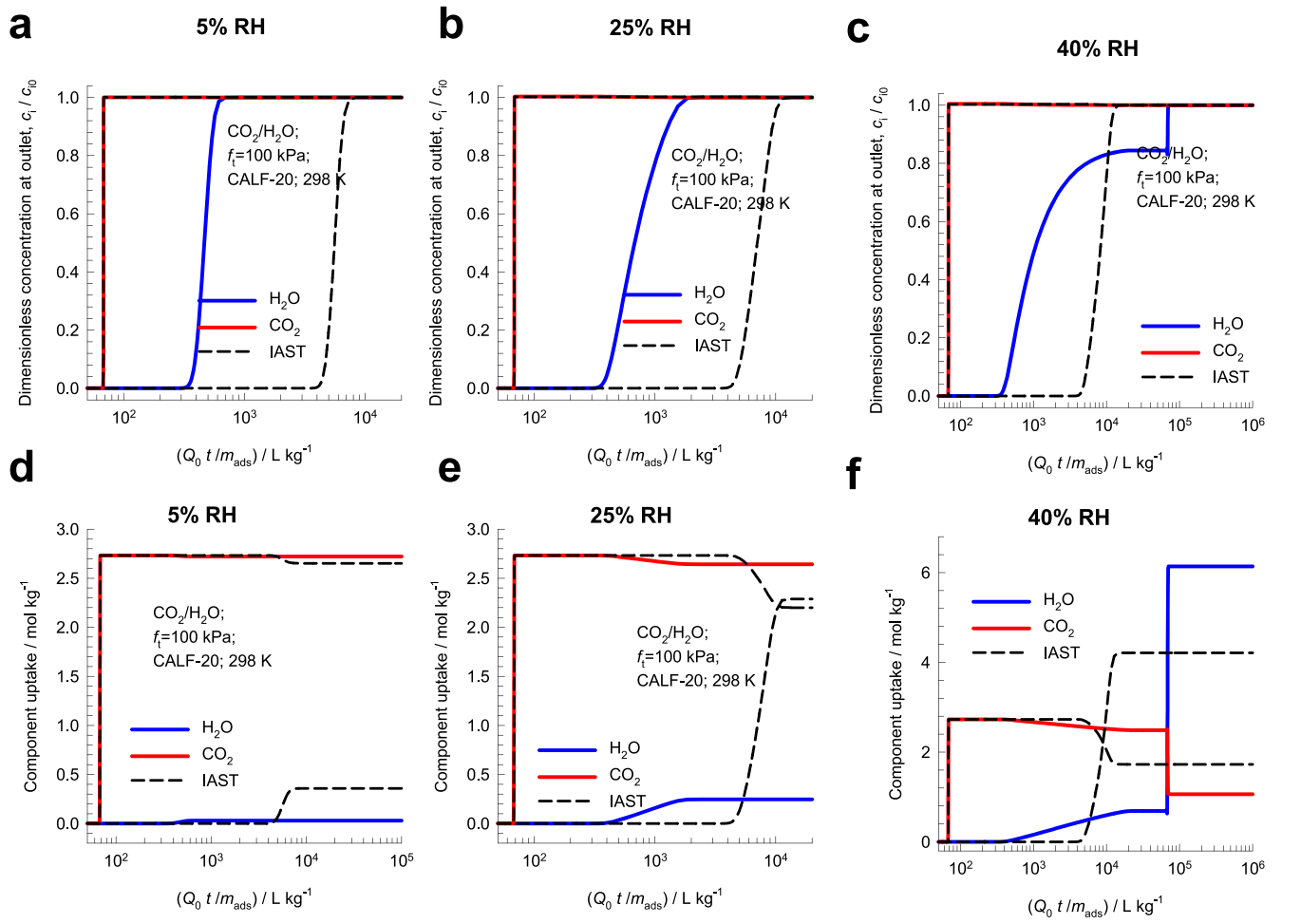

Fig. 10. Comparison of breakthrough simulations using RAST (continuous colored lines) and IAST (dashed lines) for CO_2/H_2O mixtures at a total fugacity = 100 kPa, and temperature 298 K. Three different values of % RH are considered.

5. Conclusions

CBMC simulations of $CO_2/CH_4/H_2O$, CH_4/H_2O, and CO_2/H_2O mixture adsorption in CALF-20 mixture adsorption in CALF-20 reveal strong thermodynamic non-idealities. The deviations from the IAST estimations follow two different scenarios, depending on the values of % RH. For low %RH values, the loadings of CO_2 and CH_4 in the adsorbed phase are significantly higher than anticipated by the IAST. For high % RH values, the CO_2 and CH_4 loadings in the adsorbed phase are significantly lower than anticipated by the IAST. Radial Distribution Functions (RDFs) of intermolecular distances of molecular pairs reveal that failure of the IAST can be traced to the phenomenon of segregated adsorption prevails at low values of %RH. CH_4 (and CO_2) locates at sites that are distant from H_2O; consequently, CH_4 (and CO_2) faces less severe competition from H_2O than anticipated by the IAST, that mandates a homogeneous distribution of adsorbates within CALF-20 pores. For high values of %RH, the CH_4 (and CO_2) molecules are compelled to share same adsorption site with pairs of H_2O molecules that are hydrogen-bonded with each other. Consequently, the competition faced by CH_4 (and CO_2) is significantly higher than anticipated by the IAST, resulting in significantly lower CH_4 and CO_2 uptakes. The IAST does not cater for molecular clustering resulting from hydrogen bonding between pairs of water molecules.

It is evident the design and development of adsorption processes using CALF-20 for CO_2 capture from humid natural gas mixtures must use the RAST for description of mixture adsorption equilibrium. The inclusion of the correction factor $(1-\exp(-C\Phi))$ is of vital importance in order to ensure the proper limiting characteristics $\Phi\to 0$; $\gamma_1\to 1$; $\gamma_2\to 1$; $G^{ex}\to 0$, as evidenced in Fig. 6 and Fig. 8. The ternary NRLT RAST model (eq (3)) allows calculations of the ternary mixture adsorption equilibrium using parameter inputs of the constituent binary pairs.

The inclusion of thermodynamic non-idealities in mixture has a significant influence on component breakthroughs and dynamic uptakes in fixed bed adsorbers.

Declaration of competing interest

The authors declare that they have no known competing financial interests or personal relationships that could have appeared to influence the work reported in this paper.

Data availability

All data is provided in the Supplementary Material

Appendix A. Supplementary data

Supplementary data to this article can be found online at https://doi.org/10.1016/j.seppur.2024.129553.

References

[1] J.-B. Lin, T.T.T. Nguyen, R. Vaidhyanathan, J. Burner, J.M. Taylor, H. Durekova, F. Akhtar, R.K. Mah, O. Ghaffari-Nik, S. Marx, N. Fylstra, S.S. Iremonger, K.

W. Dawson, P. Sarkar, P. Hovington, A. Rajendran, T.K. Woo, G.K.H. Shimizu, A scalable metal-organic framework as a durable physisorbent for carbon dioxide capture, Science 374 (2021) 1464–1469. https://www.science.org/doi/abs/10.1126/science.abi7281.

[2] T.T.T. Nguyen, B.M. Balasubramaniam, N. Fylstra, R.P.S. Huynh, G.K.H. Shimizu, A. Rajendran, Competitive CO_2/H_2O Adsorption on CALF-20, Ind. Eng. Chem. Res. 63 (2024) 3265–3281, https://doi.org/10.1021/acs.iecr.3c04266.

[3] J.C. Moreton, R. Krishna, J.M. Van Baten, N. Fylstra, M. Chen, T. Carr, K. Fielder, K. Chan, G.K.H. Shimizu, S. Yamamoto, A Thin Film Approach to Rapid, Quantitative Measurements of Mixed-Gas Adsorption Equilibrium in Nanoporous Materials, ChemRxiv (2024) 1–20, https://doi.org/10.26434/chemrxiv-2024-0mhg1.

[4] K. Gopalsamy, D. Fan, N.S.Y. Magnin, G. Maurin, Engineering of an Iso-Reticular Series of CALF-20 MOF for CO2 Capture, ACS Appl. Eng. Mater. 2 (2024) 96–103, https://doi.org/10.1021/acsaenm.3c00622.

[5] C.-H. Ho, F. Paesani, Elucidating the Competitive Adsorption of H_2O and CO_2 in CALF-20: New Insights for Enhanced Carbon Capture Metal−Organic Frameworks ACS Appl, Mater. Interfaces 15 (2023) 48287–48295, https://doi.org/10.1021/acsami.3c11092.

[6] R. Krishna, J.M. Van Baten, Elucidating the Failure of the Ideal Adsorbed Solution Theory for CO_2/H_2O Mixture Adsorption in CALF-20, Sep. Purif. Technol. 352 (2025) 128269, https://doi.org/10.1016/j.seppur.2024.128269.

[7] X. Peng, L. Zhao, Y.-L. Peng, C. Deng, Y.H. Andaloussi, H. Pan, Y.-J. Tian, J.-S. Zou, R. Krishna, B. Liu, C. Deng, P. Xiao, C. Sun, M.J. Zaworotko, G. Chen, Z. Zhang, One-Step Ethylene Purification from a Seven-Component Cracking Gas Mixture with Sorbent-Sorbate Induced-fit, CCS Chem. xx (2024) xx. Doi: 10.31635/ccschem.024.202403977.

[8] X.-Z. Guo, B. Li, G.-Z. Xiong, B. Lin, L.-C. Gui, X.-X. Zhang, Z. Qiu, R. Krishna, X. Wang, X. Yan, S.-S. Chen, A stable ultramicroporous Cd-MOF with accessible oxygen sites for efficient separation of light hydrocarbons with high methane production, Sep. Purif. Technol. 334 (2024), https://doi.org/10.1016/j.seppur.2023.125987.

[9] Y. Chen, Y. Jiang, J. Li, X. Hong, H. Ni, L. Wang, N. Ma, Tong, M., R. Krishna, Y. Zhang, Optimizing cask effect in multi-component natural gas purification with high methane productivity, A.I.Ch.E.J. 70 (2024) e18320. Doi: 10.1002/aic.18320.

[10] Q. Zhang, X. Lian, R. Krishna, S.-Q. Yang, T.-L. Hu, An ultramicroporous metal-organic framework based on octahedral-like cages showing high-selective methane purification from a six-component C1/C2/C3 hydrocarbons mixture, Sep. Purif. Technol. 304 (2023) 122312, https://doi.org/10.1016/j.seppur.2022.122312.

[11] Y. Hu, Y. Chen, W. Yang, J. Hu, X. Li, L. Wang, Y. Zhang, Efficient carbon dioxide capture from flue gas and natural gas by a robust metal–organic framework with record selectivity and excellent granulation performance, Sep. Purif. Technol. 343 (2024) 127099, https://doi.org/10.1016/j.seppur.2024.127099.

[12] W. Sun, J. Hu, S. Duttwyler, L. Wang, R. Krishna, Y. Zhang, Highly selective gas separation by two isostructural boron cluster pillared MOFs, Sep. Purif. Technol. 283 (2022) 120220, https://doi.org/10.1016/j.seppur.2021.120220.

[13] Y. Hu, Y. Jiang, J. Li, L. Wang, M. Steiner, R.F. Neumann, B. Luan, Y. Zhang, New-Generation Anion-Pillared Metal-Organic Frameworks with Customized Cages for Highly Efficient CO2 Capture, Adv. Funct. Mater. 33 (2023) 2213915, https://doi.org/10.1002/adfm.202213915.

[14] Y. Jiang, Y. Hu, B. Luan, L. Wang, R. Krishna, H. Ni, X. Hu, Y. Zhang, Benchmark Single-Step Ethylene Purification from Ternary Mixtures by a Customized Fluorinated Anion Embedded MOF, Nat. Commun. 14 (2023) 401, https://doi.org/10.1038/s41467-023-35984-5.

[15] Y. Chen, Z. Wu, L. Fan, R. Krishna, H. Huang, Y. Wang, Q. Xiong, Jinping, J. Li, L. Li, Direct Ethylene Purification from Cracking Gas via a Metal-Organic Framework through Pore Geometry Fitting, Engineering xx (2024) 122635. Doi: 10.1016/j.eng.2024.01.024.

[16] R. Krishna, J.M. van Baten, In silico screening of metal-organic frameworks in separation applications, Phys. Chem. Chem. Phys. 13 (2011) 10593–10616, https://doi.org/10.1039/C1CP20282K.

[17] R. Krishna, J.M. van Baten, In Silico Screening of Zeolite Membranes for CO_2 Capture, J. Membr. Sci. 360 (2010) 323–333, https://doi.org/10.1016/j.memsci.2010.05.032.

[18] R. Krishna, J.M. van Baten, Describing Mixture Diffusion in Microporous Materials under Conditions of Pore Saturation, J. Phys. Chem. C 114 (2010) 11557–11563.

[19] R. Krishna, J.M. van Baten, Diffusion of alkane mixtures in zeolites. Validating the Maxwell-Stefan formulation using MD simulations, J. Phys. Chem. B 109 (2005) 6386-6396.

[20] R. Krishna, J.M. van Baten, Insights into diffusion of gases in zeolites gained from molecular dynamics simulations, Microporous Mesoporous Mater. 109 (2008) 91–108.

[21] R. Krishna, Describing the Diffusion of Guest Molecules inside Porous Structures, J. Phys. Chem. C 113 (2009) 19756–19781, https://doi.org/10.1021/jp906879d).

[22] R. Krishna, Diffusion in Porous Crystalline Materials, Chem. Soc. Rev. 41 (2012) 3099–3118, https://doi.org/10.1039/C2CS15284C.

[23] S.L. Mayo, B.D. Olafson, W.A. Goddard, DREIDING: A Generic Force Field for Molecular Simulations, J. Phys. Chem. 94 (1990) 8897–8909.

[24] J.P. Ryckaert, A. Bellemans, Molecular dynamics of liquid alkanes, Faraday Discuss. Chem. Soc. 66 (1978) 95–106.

[25] D. Dubbeldam, S. Calero, T.J.H. Vlugt, R. Krishna, T.L.M. Maesen, B. Smit, United Atom Forcefield for Alkanes in Nanoporous Materials, J. Phys. Chem. B 108 (2004) 12301–12313.

[26] A. García-Sánchez, C.O. Ania, J.B. Parra, D. Dubbeldam, T.J.H. Vlugt, R. Krishna, S. Calero, Development of a Transferable Force Field for Carbon Dioxide Adsorption in Zeolites, J. Phys. Chem. C 113 (2009) 8814–8820, https://doi.org/10.1021/jp810871f.

[27] H.W. Horn, W.C. Swope, J.W. Pitera, J.D. Madura, T.J. Dick, G.L. Hura, T. Head-Gordon, Development of an improved four-site water model for biomolecular simulations: TIP4P-Ew, J. Chem. Phys. 120 (2004) 9665–19578, https://doi.org/10.1063/1.1683075.

[28] R. Krishna, J.M. van Baten, Hydrogen Bonding Effects in Adsorption of Water-alcohol Mixtures in Zeolites and the Consequences for the Characteristics of the Maxwell-Stefan Diffusivities, Langmuir 26 (2010) 10854–10867, https://doi.org/10.1021/la100737c.

[29] R. Krishna, J.M. Van Baten, How Reliable is the Ideal Adsorbed Solution Theory for Estimation of Mixture Separation Selectivities in Microporous Crystalline Adsorbents? ACS Omega 6 (2021) 15499–15513, https://doi.org/10.1021/acsomega.1c02136.

[30] R. Krishna, J.M. Van Baten, Using Molecular Simulations for Elucidation of Thermodynamic Non-Idealities in Adsorption of CO_2-containing Mixtures in NaX Zeolite, ACS Omega 5 (2020) 20535–20542, https://doi.org/10.1021/acsomega.0c02730.

[31] R. Krishna, J.M. Van Baten, Elucidation of Selectivity Reversals for Binary Mixture Adsorption in Microporous Adsorbents, ACS Omega 5 (2020) 9031–9040, https://doi.org/10.1021/acsomega.0c01051.

[32] R. Krishna, J.M. Van Baten, Investigating the Non-idealities in Adsorption of CO_2-bearing Mixtures in Cation-exchanged Zeolites, Sep. Purif. Technol. 206 (2018) 208–217, https://doi.org/10.1016/j.seppur.2018.06.009).

[33] R. Krishna, J.M. van Baten, R. Baur, Highlighting the Origins and Consequences of Thermodynamic Nonidealities in Mixture Separations using Zeolites and Metal-Organic Frameworks, Microporous Mesoporous Mater. 267 (2018) 274–292. (https://doi.org/10.1016/j.micromeso.2018.03.013.

[34] R. Krishna, J.M. van Baten, Fundamental Insights into the Variety of Factors that Influence Water/Alcohol Membrane Permeation Selectivity, J. Membr. Sci. 698 (2024) 122635, https://doi.org/10.1016/j.memsci.2024.122635.

[35] R. Krishna, J.M. Van Baten, Water/Alcohol Mixture Adsorption in Hydrophobic Materials: Enhanced Water Ingress caused by Hydrogen Bonding, ACS Omega 5 (2020) 28393–28402, https://doi.org/10.1021/acsomega.0c04491.

[36] C. Zhang, X. Yang, Molecular dynamics simulation of ethanol/water mixtures for structure and diffusion properties, Fluid Phase Equilib. 231 (2005) 1–10.

[37] O. Talu, A.L. Myers, Rigorous Thermodynamic Treatment of Gas-Adsorption, A.I. Ch.E.J. 34 (1988) 1887–1893.

[38] F.R. Siperstein, A.L. Myers, Mixed-Gas Adsorption, A.I, Ch.E.J. 47 (2001) 1141–1159, https://doi.org/10.1002/aic.690470520).

[39] R. Krishna, Thermodynamic Insights into the Characteristics of Unary and Mixture Permeances in Microporous Membranes, ACS Omega 4 (2019) 9512–9521, https://doi.org/10.1021/acsomega.9b00907.

[40] R. Krishna, J.M. Van Baten, Using Molecular Simulations to Unravel the Benefits of Characterizing Mixture Permeation in Microporous Membranes in Terms of the Spreading Pressure, ACS Omega 5 (2020) 32769–32780, https://doi.org/10.1021/acsomega.0c05269.

[41] S. Sochard, N. Fernandes, J.-M. Reneaume, Modeling of Adsorption Isotherm of a Binary Mixture with Real Adsorbed Solution Theory and Nonrandom Two-Liquid Model, A.I.Ch.E.J. 56 (2010) 3109–3119.

[42] N. Mittal, P. Bai, I. Siepmann, P. Daoutidis, M. Tsapatsis, Bioethanol Enrichment using Zeolite Membranes: Molecular Modeling, Conceptual Process Design and Techno-Economic Analysis, J. Membr. Sci. 540 (2017) 464–476.

[43] G. Calleja, A. Jimenez, J. Pau, L. Domínguez, P. Pérez, Multicomponent Adsorption Equilibrium of Ethylene, Propane, Propylene and CO_2 on 13X Zeolite, Gas Sep. Purif. 8 (1994) 247–256.

[44] H. Kaur, B.D. Marshall, Real adsorbed solution theory model for the adsorption of CO_2 from humid gas on CALF-20, ChemRxiv (2023) 1–18, https://doi.org/10.26434/chemrxiv-2023-2cp2c.

[45] R. Krishna, Highlighting the Influence of Thermodynamic Coupling on Kinetic Separations with Microporous Crystalline Materials, ACS Omega 4 (2019) 3409–3419, https://doi.org/10.1021/acsomega.8b03480.

[46] R. Krishna, Metrics for Evaluation and Screening of Metal-Organic Frameworks for Applications in Mixture Separations, ACS Omega 5 (2020) 16987–17004, https://doi.org/10.1021/acsomega.0c02218.

[47] R. Krishna, Synergistic and Antisynergistic Intracrystalline Diffusional Influences on Mixture Separations in Fixed Bed Adsorbers, Precision, Chemistry 1 (2023) 83–93, https://doi.org/10.1021/prechem.2c00003.

[48] R. Krishna, Fundamental Insights into Intra-Crystalline Diffusional Influences on Mixture Separations in Fixed Bed Adsorbers, Chem Bio Eng. 1 (2024) 53–66, https://doi.org/10.1021/cbe.3c00057.

Supplementary Material

Non-Idealities in Adsorption Thermodynamics for CO_2 Capture from Humid Natural Gas using CALF-20

Rajamani Krishna* and Jasper M. van Baten

Van 't Hoff Institute for Molecular Sciences

University of Amsterdam

Science Park 904

1098 XH Amsterdam, The Netherlands

email: r.krishna@uva.nl; r.krishna@contact.uva.nl

ORCID 0000-0002-4784-8530

Contents

1 Preamble

The Supplementary Material accompanying our article *Non-Idealities in Adsorption Thermodynamics for CO_2 Capture from Humid Natural Gas using CALF-20* provides (a) structural details of CALF-20, (b) details of the CBMC simulation methodology, (b) details of the IAST, and Real Adsorbed Solution Theory (RAST) calculations for mixture adsorption equilibrium, (c) unary isotherm fit parameters, (d) NRTL parameters fits for thermodynamic non-idealities, (e) Plots of CBMC simulation data and comparisons with IAST/RAST estimates, and (f) RAST modelling of fixed bed adsorbers.

For ease of reading, the Supplementary Material is written as a stand-alone document; as a consequence, there is some overlap of material with the main manuscript.

2 Hydrocarbon separations with CALF-20

Industrial purification processes for ethylene from steam pyrolysis or cracking gases generally employ multiple energy-intensive steps to remove C_2H_2, C_2H_6, CO_2, and C3 hydrocarbons. Peng et al.[1] have demonstrated the efficacy of ultramicroporous crystalline physisorbent CALF-20 (= Calgary Framework 20) to purify C_2H_4 from a seven-component cracking gas mixture (C_2H_4, C_2H_2, C_2H_6, CO_2, C_3H_4, C_3H_6, and C_3H_8) by one-step separation with remarkable performance. Figure S1a presents experimental data of Peng et al.[1] for the unary isotherms for C_2H_4, C_2H_2, C_2H_6, CO_2, C_3H_4, C_3H_6, and C_3H_8 in CALF-20 at 298 K. The breakthrough experiments reported by Peng et al.[1] demonstrate that C_2H_4 (>99.99%) can be recovered from not only binary C_2H_6/C_2H_4 (50/50), ternary $C_2H_2/C_2H_4/C_2H_6$ (33/33/33) and quaternary $C_2H_2/C_2H_4/C_2H_6/CO_2$ (25/25/25/25) mixtures, but also a typical seven-component gas cracking mixture of 0.6/62/10/0.3/0.6/26/0.5 $C_2H_2/C_2H_4/C_2H_6/CO_2/C_3H_4/C_3H_6/C_3H_8$ mixtures even at the high humidity of 74%.

Figure S1b compares the unary isotherms for CH_4, C_2H_6, CO_2, and C_3H_8 in CALF-20 at 298 K; the unary CH_4 isotherm data are CBMC simulations reported in this work. These unary isotherm data seem to suggest that CALF-20 has the potential for one-step separation of ternary $CH_4/C_2H_6/C_3H_8$ and quaternary $CH_4/C_2H_6/CO_2/C_3H_8$ mixtures to produce purified CH_4 with high productivities. For natural gas purification, CALF-20 should be expected to provide stiff competition to other reported MOFs,[2-4] especially under humid conditions.

2.1 List of Figures for Hydrocarbon separations with CALF-20

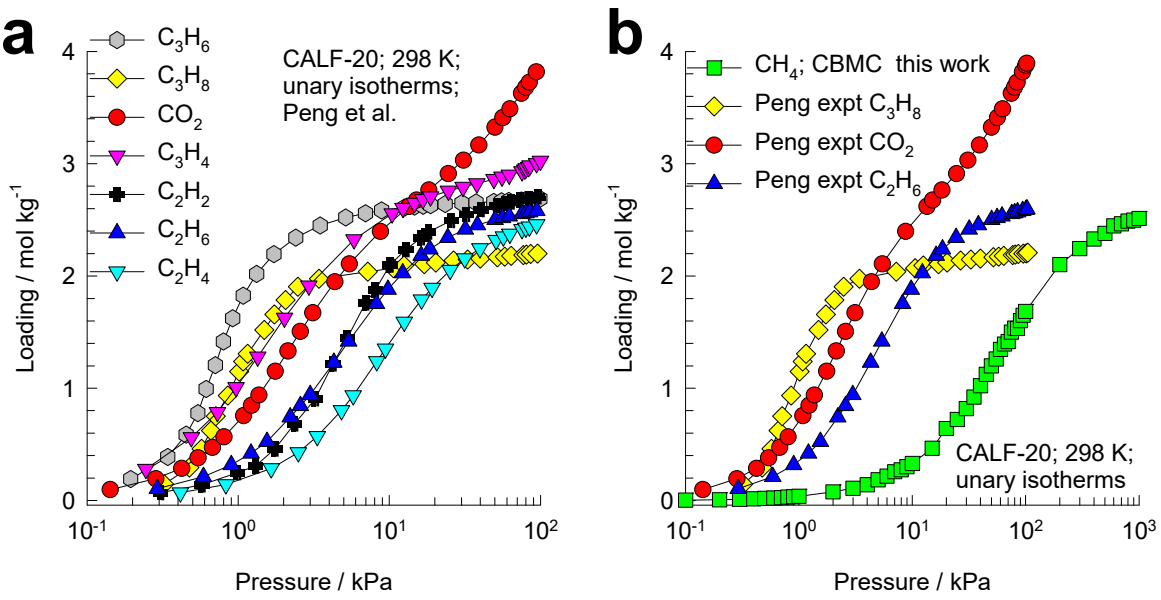

Figure S1. (a) Experimental data of Peng et al.[1] for unary isotherms for C_2H_4, C_2H_2, C_2H_6, CO_2, C_3H_4, C_3H_6, and C_3H_8 in CALF-20 at 298 K. (b) Unary isotherms for CH_4, C_2H_6, CO_2, and C_3H_8 in CALF-20 at 298 K. The unary CH_4 isotherm data are CBMC simulations reported in this work.

3 The Ideal Adsorbed Solution Theory

We provide a brief outline of the Ideal Adsorbed Solution Theory for calculation of mixture adsorption equilibrium.

3.1 Gibbsian thermodynamics of mixture adsorption

The Gibbs adsorption equation[5] in differential form is

$$Ad\pi = \sum_{i=1}^{n} q_i d\mu_i \tag{S1}$$

The quantity A is the surface area per kg of framework, with units of m^2 per kg of the framework of the crystalline material; q_i is the molar loading of component i in the adsorbed phase with units moles per kg of framework; μ_i is the molar chemical potential of component i. The spreading pressure π has the same units as surface tension, i.e. N m^{-1}.

The chemical potential of any component in the adsorbed phase, μ_i, equals that in the bulk fluid phase. If the partial fugacities in the bulk fluid phase are f_i, we have

$$d\mu_i = RTd\ln f_i \tag{S2}$$

where R is the gas constant (= 8.314 J mol^{-1} K^{-1}).

Briefly, the basic equation of Ideal Adsorbed Solution Theory (IAST) theory of Myers and Prausnitz[6] is the analogue of Raoult's law for vapor-liquid equilibrium, i.e.

$$f_i = P_i^0 x_i; \quad i = 1, 2, ...n \tag{S3}$$

where x_i is the mole fraction in the adsorbed phase

$$x_i = \frac{q_i}{q_1 + q_2 + ...q_n} \tag{S4}$$

and P_i^0 is the pressure for sorption of every component i, which yields the same spreading pressure, π for each of the pure components, as that for the mixture:

$$\frac{\pi A}{RT} \equiv \Phi = \int_0^{P_1^0} \frac{q_1^0(f)}{f} df = \int_0^{P_2^0} \frac{q_2^0(f)}{f} df = \int_0^{P_3^0} \frac{q_3^0(f)}{f} df = ... \tag{S5}$$

where $q_i^0(f)$ is the *pure* component adsorption isotherm. The units of $\Phi \equiv \frac{\pi A}{RT}$, also called the surface potential, [7-11] are mol kg^{-1}.

The unary isotherm may be described by say the 1-site Langmuir isotherm

$$q^0(f) = q_{sat} \frac{bf}{1+bf}; \quad \theta = \frac{bf}{1+bf} \tag{S6}$$

where we define the fractional *occupancy* of the adsorbate molecules, $\theta = q^0(f)/q_{sat}$. The superscript 0 is used to emphasize that $q^0(f)$ relates the *pure component* loading to the bulk fluid fugacity. For unary isotherms described by the dual-site Langmuir-Freundlich (DSLF) model

$$q^0(f) = q_{A,sat} \frac{b_A f^{\nu A}}{1+b_A f^{\nu A}} + q_{B,sat} \frac{b_B f^{\nu B}}{1+b_B f^{\nu B}} \tag{S7}$$

each of the integrals in eq (S5) can be evaluated analytically. The integration yields for component *i*,

$$\begin{aligned} \Phi \equiv \frac{\pi A}{RT} &= \int_{f=0}^{P_i^0} \frac{q_i^0(f)}{f} df = \frac{q_{A,sat}}{\nu_A} \ln\left(1+b_A\left(P_i^0\right)^{\nu_A}\right) + \frac{q_{B,sat}}{\nu_B} \ln\left(1+b_B\left(P_i^0\right)^{\nu_B}\right); \\ \Phi \equiv \frac{\pi A}{RT} &= \int_{f=0}^{P_i^0} \frac{q_i^0(f)}{f} df = \frac{q_{A,sat}}{\nu_A} \ln\left(1+b_A\left(\frac{f_i}{x_i}\right)^{\nu_A}\right) + \frac{q_{B,sat}}{\nu_B} \ln\left(1+b_B\left(\frac{f_i}{x_i}\right)^{\nu_B}\right) \end{aligned} \tag{S8}$$

The right hand side of eq (S8) is a function of P_i^0. For multicomponent mixture adsorption, each of the equalities on the right hand side of Eq (S5) must be satisfied. These constraints may be solved using a suitable equation solver, to yield the set of values of , P_2^0, P_3^0,.. P_n^0, each of which satisfy eq (S5). The corresponding values of the integrals using these as upper limits of integration must yield the same value of Φ for each component; this ensures that the obtained solution is the correct one.

In the IAST, the adsorbed phase mole fractions x_i are then determined from

$$x_i = \frac{f_i}{P_i^0}; \quad i = 1, 2, ...n \tag{S9}$$

The applicability of eqs (S3) and (S9) mandates that all of the adsorption sites within the microporous material are equally accessible to each of the guest molecules, implying a homogeneous distribution of guest adsorbates within the pore landscape, with no preferential locations of any guest species. The circumstances in which this mandate is not fulfilled are highlighted in recent works.[9, 10, 12, 13]

A further key assumption of the IAST is that the adsorption enthalpies and surface areas of the adsorbed molecules do not change upon mixing.[14] If the total mixture loading is q_t, the area covered by the adsorbed mixture is $\frac{A}{q_t}$ with units of m^2 (mol mixture)$^{-1}$. Therefore, the assumption of no surface area change due to mixture adsorption translates as $\frac{A}{q_t} = \frac{Ax_1}{q_1^0\left(P_1^0\right)} + \frac{Ax_2}{q_2^0\left(P_2^0\right)} + \cdots \frac{Ax_n}{q_n^0\left(P_n^0\right)}$; the total mixture loading is q_t is calculated from

$$q_t = q_1 + q_2 ... + q_n = \frac{1}{\frac{x_1}{q_1^0(P_1^0)} + \frac{x_2}{q_2^0(P_2^0)} + ... + \frac{x_n}{q_n^0(P_n^0)}} \tag{S10}$$

in which $q_1^0(P_1^0)$, $q_2^0(P_2^0)$,… $q_n^0(P_n^0)$ are determined from the unary isotherm fits, using the sorption pressures for each component P_1^0, P_2^0, P_3^0,.. P_n^0 that are available from the solutions to equations Eqs (S5), and (S8).

The occurrence of molecular clustering and hydrogen bonding should be expected to applicability of eq (S10) because the surface area occupied by a molecular cluster is different from that of each of the un-clustered guest molecules in the adsorbed phase; see published literature for details.[11, 13, 15]

The entire set of eqs (S3) to (S10) need to be solved numerically to obtain the loadings, q_i of the individual components in the mixture.

In a number of publications on CO_2 capture from mixtures containing N_2, CH_4, C_2H_4, C_2H_6, C_3H_8, and H_2O using cation-exchanged zeolites,[9, 10, 12, 14, 16-21] the IAST has been shown to fail due to non-compliance with one or more of the afore-mentioned tenets.

For further explanation on the numerical techniques for solving the IAST, fitting of isotherms, the tenets of the IAST, the concept of the surface potential, watch the presentations titled **The IAST for Mixture Adsorption Equilibrium, Dependence of Adsorption Selectivity on Mixture Composition, Adsorption Selectivity vs Total Pressure, Significance of the Spreading Pressure Concept, Hydrogen Bonding Influences on Adsorption, Langmuir Model for Binary Mixture Adsorption, Reversals in Adsorption Selectivity, Competitive CO_2/H_2O Mixture Adsorption in CALF-20** on YouTube https://www.youtube.com/@rajamanikrishna250/videos

3.2 The fractional pore occupancy

From knowledge of the surface potential, Φ , the fractional pore occupancy θ for mixture adsorption is then calculated using

$$\theta = 1 - \exp\left(-\frac{\pi A}{q_{sat,mix} RT}\right) = 1 - \exp\left(-\frac{\Phi}{q_{sat,mix}}\right) \tag{S11}$$

For binary mixtures the saturation capacity $q_{sat,mix}$ is calculated from the saturation capacities of the constituent guests

$$\frac{1}{q_{sat,mix}} = \frac{x_1}{q_{1,sat}} + \frac{x_2}{q_{2,sat}}; \quad q_{i,sat} = q_{i,A,sat} + q_{i,B,sat}; \quad i = 1,2 \tag{S12}$$

Where x_i are the mole fractions in the adsorbed mixture. The fundamental justification of eq (S12) is provided by invoking eq (S10).

4 The Real Adsorbed Solution Theory (RAST)

To quantify non-ideality effects in mixture adsorption, we introduce activity coefficients γ_i into eq (S3) as [6, 13, 14]

$$f_i = P_i^0 x_i \gamma_i \tag{S13}$$

Following the approaches of Myers, Talu, and Siperstein[7, 8, 22] we model the excess Gibbs free energy for n-component mixtures adsorption as follows

$$G^{ex}/RT = \sum_{i=1}^{n} x_i \ln(\gamma_i) \tag{S14}$$

For calculation of the total mixture loading $q_t = q_1 + q_2$ we need to replace eq (S10) by

$$\frac{1}{q_t} = \frac{x_1}{q_1^0(P_1^0)} + \frac{x_2}{q_2^0(P_2^0)} + \left(\frac{1}{q_t}\right)^{ex} \tag{S15}$$

The excess reciprocal loading for the mixture can be related to the partial derivative of the Gibbs free energy with respect to the surface potential at constant composition

$$\left(\frac{1}{q_t}\right)^{ex} = \left.\frac{\partial\left(G^{ex}/RT\right)}{\partial\Phi}\right|_{T,x} \tag{S16}$$

Models such as those of Margules, Wilson, and NRTL may be used for quantifying the dependence of the activity coefficients on the composition of the adsorbed mixture and the pore occupancy θ.

4.1 Wilson model for activity coefficients

The Wilson model for activity coefficients are given for binary mixtures by

$$\begin{aligned}
\ln(\gamma_1) &= \left(1 - \ln(x_1\Lambda_{11} + x_2\Lambda_{12}) - \frac{x_1\Lambda_{11}}{x_1\Lambda_{11} + x_2\Lambda_{12}} - \frac{x_2\Lambda_{21}}{x_2 + x_1\Lambda_{21}}\right)\left(1 - \exp\left(-C\Phi\right)\right) \\
\ln(\gamma_2) &= \left(1 - \ln(x_1\Lambda_{21} + x_2\Lambda_{22}) - \frac{x_1\Lambda_{12}}{x_1\Lambda_{11} + x_2\Lambda_{12}} - \frac{x_2\Lambda_{22}}{x_1\Lambda_{21} + x_2\Lambda_{22}}\right)\left(1 - \exp\left(-C\Phi\right)\right)
\end{aligned} \tag{S17}$$

In eq (S17), $\Lambda_{11} \equiv 1; \quad \Lambda_{22} \equiv 1$, and C is a constant with the units kg mol^{-1}. The choice of $\Lambda_{12} = \Lambda_{21} = 1$ in eq (S17), yields unity values for the activity coefficients. The introduction of $\left(1-\exp\left(-C\Phi\right)\right)$ imparts the correct limiting behaviors $\Phi \to 0; \quad \theta \to 0; \quad \gamma_i \to 1$ for the activity coefficients in the Henry regime, $f_t \to 0; \quad \Phi \to 0$, as the pore occupancy tends to vanishingly small values. As pore saturation conditions are approached, this correction factor tends to unity: $\left(1-\exp\left(-C\Phi\right)\right) \to 1$. We note, in passing, that this correction factor $\left(1-\exp\left(-C\Phi\right)\right)$ is often ignored in the RAST implementations in some published works.[23-26]

Krishna and van Baten[27] have established the need for inclusion of the correction factor $\left(1-\exp\left(-C\Phi\right)\right)$ in the RAST modelling of CO_2/H_2O mixture adsorption in CALF-20. Watch the presentations titled **Thermodynamic Non-Idealities for Mixture Adsorption in CALF-20** on YouTube https://www.youtube.com/@rajamanikrishna250/videos

For further details of the RAST calculations and the need for inclusion of the $\left(1-\exp\left(-C\Phi\right)\right)$ correction factor watch the presentations titled **Dependence of Adsorption Selectivity on Mixture Composition, Hydrogen Bonding Influences on Adsorption, How Reliable is the IAST?, The Real Adsorbed Solution Theory, Co-operative Mixture Adsorption in Zeolites & MOFs, Azeotropic Adsorption, What is Azeotropic Adsorption, Water/Alcohol Azeotropic Adsorption, Segregation and Congregation Effects in CO_2 capture, Thermodynamic Non-Idealities in CO_2 Capture with CALF-20: Parts I, II, III, IV, V, and VI**

on YouTube https://www.youtube.com/@rajamanikrishna250/videos

The excess reciprocal loading for the mixture can be related to the partial derivative of the Gibbs free energy with respect to the surface potential at constant composition

$$\left(\frac{1}{q_t}\right)^{ex} = \left.\frac{\partial\left(G^{ex}/RT\right)}{\partial\Phi}\right|_{T,x} = \left[-x_1\ln(x_1+x_2\Lambda_{12}) - x_2\ln\left(x_2+x_1\Lambda_{21}\right)\right]C\exp\left(-C\Phi\right) \qquad \text{(S18)}$$

For calculation of the total mixture loading we need to replace Eq (S10) by

$$\frac{1}{q_t}=\frac{x_1}{q_1^0(P_1^0)}+\frac{x_2}{q_2^0(P_2^0)}+\left[-x_1\ln(x_1+x_2\Lambda_{12})-x_2\ln\left(x_2+x_1\Lambda_{21}\right)\right]C\exp\left(-C\Phi\right) \tag{S19}$$

The parameters $C;\ \Lambda_{12};\ \Lambda_{21}$ are fitted to match the experimental or CBMC data on mixture adsorption.

The extension of eq (S17) to *n*-component mixtures is

$$\ln(\gamma_i)=\left(1-\ln\left(\sum_{j=1}^{n}x_j\Lambda_{ij}\right)-\sum_{k=1}^{n}x_k\frac{\Lambda_{ki}}{\sum_{l=1}^{n}x_l\Lambda_{kl}}\right)\left(1-\exp\left(-C\Phi\right)\right);\quad \Lambda_{ii}\equiv 1;\qquad i=1,2,...n \tag{S20}$$

4.2 NRTL model for activity coefficients

The NRTL model for activity coefficients are given for binary mixtures by

$$\begin{aligned}
\ln(\gamma_1)&=x_2^2\left(\tau_{21}\left(\frac{G_{21}}{x_1+x_2G_{21}}\right)^2+\frac{\tau_{12}G_{12}}{\left(x_2+x_1G_{12}\right)^2}\right)\left(1-\exp\left(-C\Phi\right)\right)\\
\ln(\gamma_2)&=x_1^2\left(\tau_{12}\left(\frac{G_{12}}{x_2+x_1G_{12}}\right)^2+\frac{\tau_{21}G_{21}}{\left(x_1+x_2G_{21}\right)^2}\right)\left(1-\exp\left(-C\Phi\right)\right)\\
G_{12}&=\exp\left(-\alpha_{12}\tau_{12}\right);\quad G_{21}=\exp\left(-\alpha_{21}\tau_{21}\right);\quad \alpha_{12}=\alpha_{21}
\end{aligned} \tag{S21}$$

In eq (S21) *C* is a constant with the units kg mol^{-1}. The choice of $\tau_{12}=\tau_{21}=0$ in eq (S21), yields unity values for the activity coefficients.

The extension of eq (S21) to *n*-component mixtures is

$$\ln(\gamma_i)=\left[\frac{\sum_{j=1}^{n}x_j\tau_{ji}G_{ji}}{\sum_{k=1}^{n}x_kG_{ki}}+\sum_{j=1}^{n}\frac{x_jG_{ij}}{\sum_{k=1}^{n}x_kG_{kj}}\left(\tau_{ij}-\frac{\sum_{l=1}^{n}x_l\tau_{lj}G_{lj}}{\sum_{k=1}^{n}x_kG_{kj}}\right)\right]\left(1-\exp\left(-C\Phi\right)\right) \tag{S22}$$

$$G_{ij}=\exp\left(-\alpha_{ij}\tau_{ij}\right);\quad \alpha_{ij}=\alpha_{ji};\quad \tau_{ii}=0;\quad G_{ii}=1$$

5 Configurational-Bias Monte Carlo simulation methodology

Configurational-Bias Monte Carlo (CBMC) simulations were carried out to determine the adsorption isotherms for unary CO_2, CH_4, H_2O, N_2 guests at 298 K. Also simulated are CO_2/H_2O, CH_4/H_2O, N_2/H_2O, $CO_2/CH_4/H_2O$ mixtures in CALF-20 at 298 K. The simulation methodologies are the same as detailed in earlier publications.[27-34] The unit cell was constructed using the structural information obtainable from CCDC 2084733 at https://www.ccdc.cam.ac.uk/structures/Search?Ccdcid=CCDC%202084733&DatabaseToSearch=Published

The CALF-20 structure was considered to be rigid in the simulations.

The unit cell dimensions of CALF-20 crystals are $a = 8.9138$ Å; $b = 9.6935$ Å; $c = 9.4836$ Å with angles $\alpha = 90°$; $\beta = 115.895°$; $\gamma = 90°$; see Figure S2. The crystal framework density $\rho = 1598.868 \ \text{kg m}^{-3}$. The simulation box for conducting CBMC simulations consisted of $5 \times 3 \times 5 = 75$ unit cells.

The interactions between adsorbed molecules are described with Lennard-Jones terms together with electrostatic interactions. For the atoms in the host metal organic framework (see Figure S3), the generic DREIDING[35] force fields were used; the Lennard-Jones parameters $\sigma_{host}, \frac{\varepsilon_{host}}{k_B}$ values are specified in Table S1, along with the partial charges.[36]

CH_4 molecules are described with a united atom model, in which each molecule is treated as a single interaction center.[37, 38] The interaction between adsorbed molecules is described with Lennard-Jones terms; see Figure S4.

CO_2 molecules are taken linear and rigid with bond length C–O of 1.16 Å according to the 3LJ3CB.EPM2 model developed by Harris and Young.[39] CO_2 was represented by a 3-site charged Lennard-Jones model as described by Garcia-Sánchez et al.[40]

Water is modeled using the four-site TIP4P-Ew potential; [41] TIP4P = 4-site transferable intermolecular potential (TIP4P) and Ew = Ewald technique.

We use the 2LJ3CB.MSKM model for N_2 dumbbell molecules with a rigid interatomic bond of 1.098Å. [42, 43] The partial charges of N_2 and CO_2 are distributed around each molecule to reproduce experimental quadrupole moment.

The Lorentz-Berthelot mixing rules were applied for calculating the Lennard-Jones parameters describing guest-host interactions

$$\sigma_{guest-host} = \frac{\left(\sigma_{guest} + \sigma_{host}\right)}{2}$$
$$\frac{\varepsilon_{guest-host}}{k_B} = \sqrt{\frac{\varepsilon_{guest}}{k_B} \times \frac{\varepsilon_{host}}{k_B}} \qquad \text{(S23)}$$

The Lennard-Jones potentials are shifted and cut at 12 Å. The pore landscapes are shown in Figure S5.

5.1 CBMC code

All simulations reported in this work were carried out using an in-house BIGMAC code, originally developed by T.J.H. Vlugt. This code was modified to handle rigid molecular structures and charges. All CBMC simulations for CALF-20 reported in this work were conducted at a temperature T = 298 K.

5.2 Activity coefficients from CBMC data

Each CBMC simulation data point, with specified partial fugacities in the bulk fluid phase, f_1, f_2, yields the component loadings, $q_{1,CBMC}; q_{2,CBMC}$, and the total mixture loading $q_{t,CBMC} = q_{1,CBMC} + q_{2,CBMC}$. For each guest/host combination, CBMC simulations of the unary isotherms of the constituent guest molecules were also carried out.

For each CBMC mixture simulation campaign, the mole fractions of the adsorbed phase, $x_1 = \frac{q_{1,CBMC}}{q_{t,CBMC}}; x_2 = \frac{q_{2,CBMC}}{q_{t,CBMC}}; q_{t,CBMC} = q_{1,CBMC} + q_{2,CBMC}$ are determined. The sorption pressures P_1^0, P_2^0, each of which satisfying eq (S5), can be determined from using the unary isotherm fits for each of the components in the binary mixture.

The activity coefficients of the two components $\gamma_{1,CBMC}; \gamma_{2,CBMC}$ are determined from eq (S13):

$$\gamma_{1,CBMC} = \frac{f_1}{P_1^0 x_{1,CBMC}}; \gamma_{2,CBMC} = \frac{f_2}{P_2^0 x_{2,CBMC}} \tag{S24}$$

The activity coefficients of the two components $\gamma_{1,CBMC}; \gamma_{2,CBMC}$, determined using eq (S24) are subject to a degree of scatter that is inherent in the CBMC mixture simulation data.

For each mixture/host combination, the set of NRTL parameters $C;\ \tau_{12};\ \tau_{21};\ \alpha_{12} = \alpha_{21}$ that yield the minimum value for the objective function calculated as the sum of the mean-squared deviations between the CBMC simulated component loadings, and those predicted using RAST

$$\text{Objective Function} = \sum \left[\left(q_{1,CBMC} - q_{1,RAST} \right)^2 + \left(q_{2,CBMC} - q_{2,RAST} \right)^2 \right] \tag{S25}$$

The parameters $C;\ \tau_{12};\ \tau_{21};\ \alpha_{12} = \alpha_{21}$ were determined using the Excel solver function.

5.3 List of Tables for Configurational-Bias Monte Carlo simulation methodology

Table S1. Lennard-Jones parameters for host atoms in CALF-20. See Figure S3 for explanation of atom names. The partial charges were provided by kind courtesy of Gopalsamy and Maurin in a personal communication to R. Krishna.[36]

atom	σ_{host} Å	$\frac{\varepsilon_{host}}{k_B}$ K	Charge	Atom count
Zn	4.045	27.680	0.6677	8
N1	3.263	38.953	-0.25823	8
N2	3.263	38.953	-0.14998	4
O	3.033	48.163	-0.51209	8
C1	3.473	47.861	0.11239	8
H	2.846	7.650	0.15033	8
C2	3.473	47.861	0.49748	4

5.4 List of Figures for Configurational-Bias Monte Carlo simulation methodology

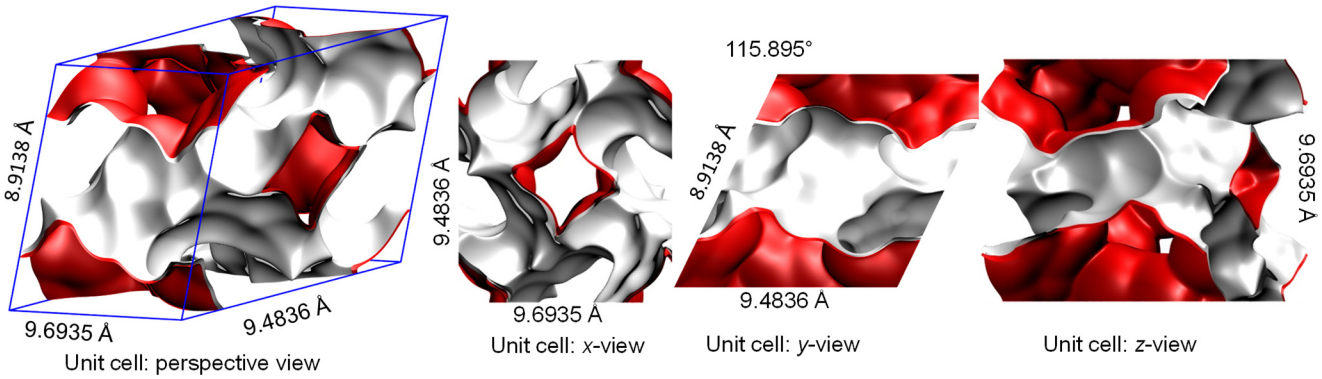

Figure S2. Unit cell of CALF-20.

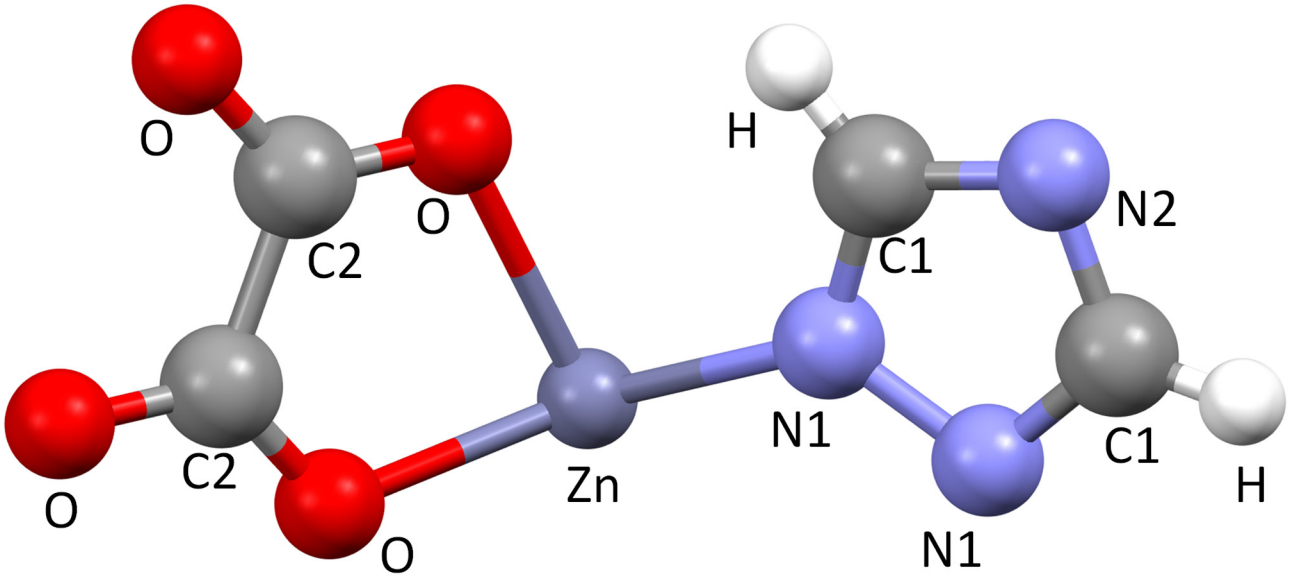

Figure S3. Atom labels used in the force field parameters for the secondary building unit (SBU) for CALF-20.

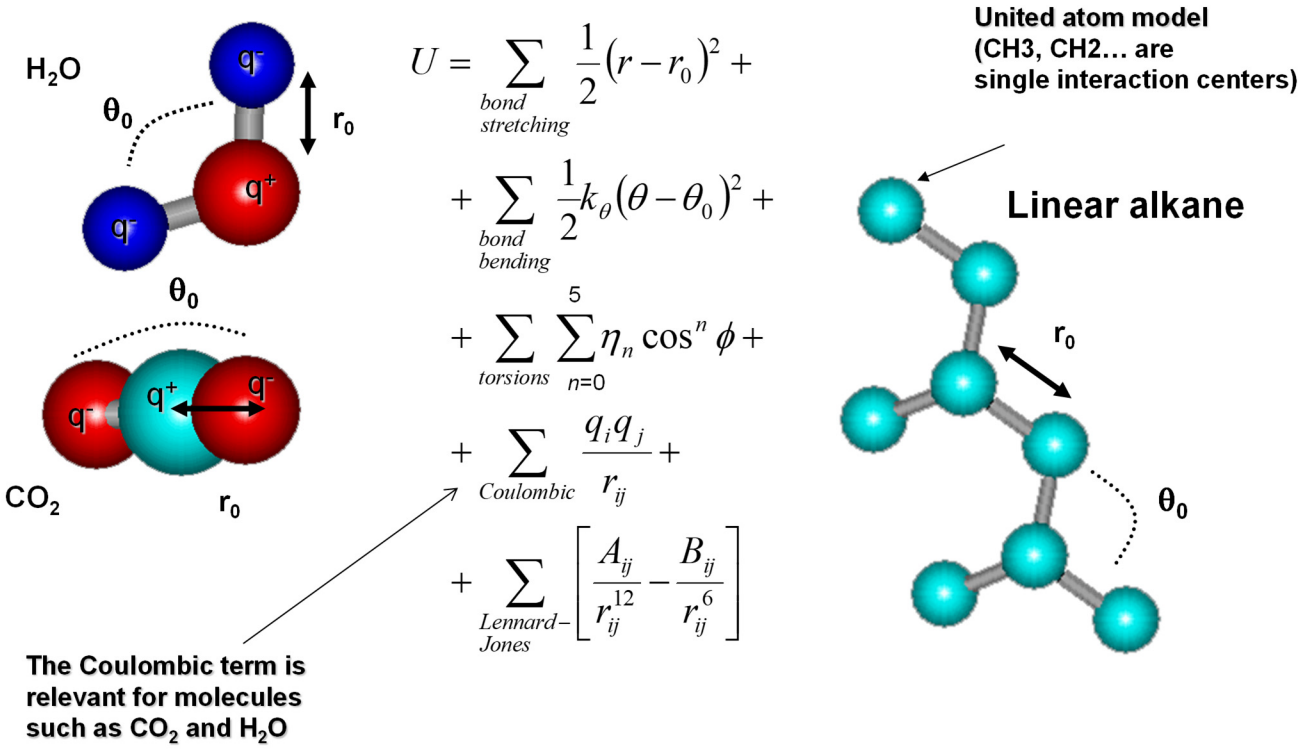

Figure S4. Potential for guest molecules.

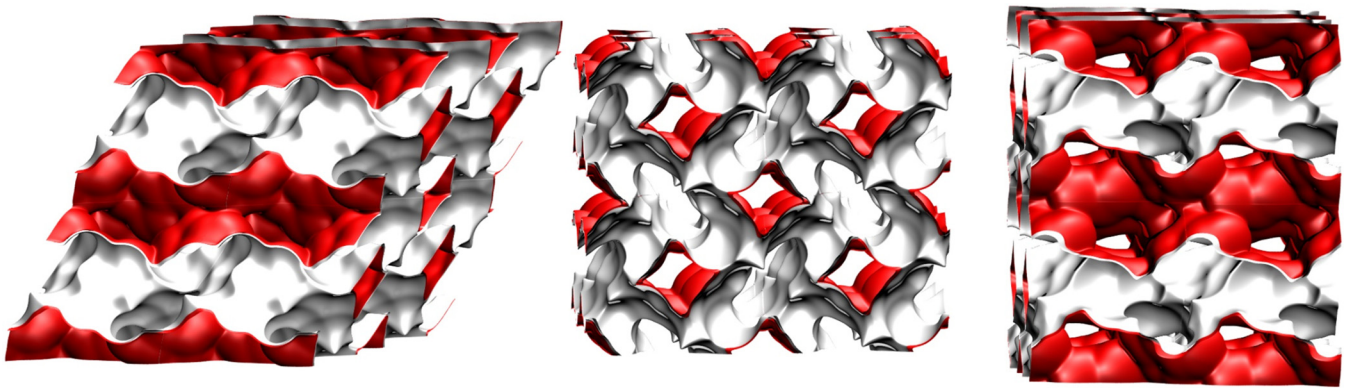

Figure S5. Pore landscapes of CALF-20.

6 CBMC Simulations in CALF-20

6.1 CBMC simulations of unary isotherms

Figure S6a,b presents the CBMC simulations conducted in this work for unary isotherms for CO_2, CH_4, N_2, and H_2O determined from fitting unary isotherms determined at 298K from CBMC simulations in CALF-20. These isotherms are fitted with the dual-site Langmuir-Freundlich model, with fit parameters as specified in Table S2.

6.2 CBMC simulations for CO_2/N_2 mixture adsorption

Figure S7b presents CBMC simulations of component loadings, q_i, for $CO_2(1)/N_2(2)$ mixture adsorption in CALF-20 at a total pressure of 100 kPa and 298 K; the mole fraction of $CO_2(1)$ in the bulk gas phase mixture, y_1, is varied from 0 to 1. The CBMC simulated loadings are in good agreement with the IAST estimations, indicated by the dashed lines. Figure S7c compares $CO_2(1)/N_2(2)$ adsorption selectivity from CBMC simulations with IAST estimates. The agreement is good, implying that none of the tenets demanded by the IAST are violated. The guest adsorbates are homogeneously distributed within the pore landscape, as is evident from the computational snapshot in Figure S8. In the experiments reported by Nguyen et al.[44] for $CO_2(1)/N_2(2)$ mixture adsorption in structured CALF-20 at 295 K, the experimental data for the N_2 loadings in their Figure S5 indicate small deviations from the IAST estimates. This deviation could be due to the fact that the mixture adsorption data of Nguyen et al.[44] are determined from breakthrough experiments that are not conducted under strict isothermal conditions.

Figure S7a presents CBMC simulations of component loadings, q_i, for $CO_2(1)/N_2(2)$ mixture adsorption in CALF-20 at 298 K with varying total fugacity f_t, maintaining the mole fraction of CO_2 in the bulk gas mixture at a constant value $y_2 = f_2/f_t = 0.05$. The dashed lines are the IAST estimations. We again note that the CBMC data for component loadings are in good agreement with the IAST

estimates. Also, the CBMC simulations for CO_2(1)/N_2(2) adsorption selectivity from CBMC simulations agree well with IAST estimates; see Figure S9b.

6.3 CBMC simulations for CO_2/CH_4 mixture adsorption

Figure S10a presents CBMC simulations of component loadings, q_i, for CO_2(1)/CH_4(2) mixture adsorption in CALF-20 at 298 K with varying total fugacity f_t, maintaining the mole fraction of CO_2 in the bulk gas mixture at a constant value $y_2 = f_2/f_t = 0.05$. The dashed lines are the IAST estimations. We again note that the CBMC data for component loadings are in good agreement with the IAST estimates. Also, the CBMC simulations for CO_2(1)/CH_4(2) adsorption selectivity, $S_{ads} = \frac{q_1/q_2}{f_1/f_2}$, from CBMC simulations agree well with IAST estimates; see Figure S10b.

6.4 CBMC simulations for CH_4/H_2O mixture adsorption

Figure S11a shows CBMC simulations of component loadings, q_i, for CH_4(1)/H_2O(2) mixture adsorption in CALF-20 at 298 K at a total fugacity = 500 kPa. The mole fraction of H_2O in the bulk gas mixture, $y_2 = f_2/f_t$, is varied. The loadings are plotted against $\%\text{RH} = \%\text{Relative Humidity} = \frac{f_2}{p_2^{sat}} \times 100$ where f_2 is the partial fugacity of water in the bulk gas phase, and p_2^{sat} is the saturation vapor pressure of water. At 298 K, p_2^{sat} is determined from the Antoine equation: $p_2^{sat} = 3150$ Pa. The IAST estimates of the component loadings are indicated by the dashed lines. We note that the CH_4/H_2O binary mixture adsorption exhibits significant departures from thermodynamic idealities. Another way to demonstrate the non-idealities is to plot the mole fraction of CH_4 in the adsorbed phase mixture, x_1, as a function of the $\%\text{RH}$, and the mole fraction of water in the bulk gas mixture, y_2 see Figure S11b, . We note that for $\%\text{RH} < 33\%; \quad y_2 < 0.002; \quad x_1 > 0.2$, the adsorbed phase mixture is richer in CH_4, i.e. poorer in H_2O,

than is anticipated by the IAST. On the other hand, for $\%RH > 33\%; \quad y_2 > 0.002; \quad x_1 < 0.2$, the adsorbed phase mixture is poorer in CH_4, i.e. richer in H_2O, than is anticipated by the IAST.

Figure S11d plots $\frac{G^{excess}}{RT} = x_1 \ln(\gamma_1) + x_2 \ln(\gamma_2)$ as function of $\%RH$. Figure S11e plots the activity coefficients γ_1, γ_2 as function of the mole fraction of CH_4 in the adsorbed phase mixture, x_1.

Figure S13 presents computational snapshots showing the location of guest CH_4 and H_2O molecules in CALF-20 at at 298 K. The total fugacity in the bulk gas phase is 500 kPa with partial fugacities f_1 = 499.1 kPa, and f_2 =0.9 kPa. The chosen conditions correspond to the scenario in Figure S11b with $\%RH < 33\%; \quad x_1 > 0.2$, i.e. the adsorbed phase mixture is richer in CH_4 than is anticipated by the IAST.

We note that the CH_4 and H_2O molecules do not occupy the same adsorption site. The preferred sites are the O atoms of the oxalate group, as established in our earlier work. Therefore, CH_4 faces less severe competition from H_2O than is anticipated by the IAST that mandates a homogeneous distribution of guest adsorbates within the pore landscape.

Figure S14 shows computational snapshots showing the location of guests CH_4 and H_2O molecules in CALF-20 at 298 K. The total fugacity in the bulk gas phase is 500 kPa with partial fugacities f_1 = 498.96 kPa, and f_2 =1.04 kPa. The chosen conditions to the scenario in Figure S11b with $\%RH > 33\%; \quad x_1 < 0.2$, i.e. the adsorbed phase mixture is poorer in CH_4 than is anticipated by the IAST. In this scenario, the channels of CALF-20 are predominantly occupied with H_2O molecules. CH_4 can only locate at sites adjacent to H_2O molecules.

The values of the fitted NRTL parameters are specified in Table S3.

To underscore the need for the correction factor, the CBMC data are used to determine the excess Gibbs free energy

$$\frac{G^{ex}}{RT} = x_1 \ln(\gamma_1) + x_2 \ln(\gamma_2) \tag{26}$$

The CBMC values for the campaign $f_t = 500\,\text{kPa};\quad \text{vary}\, y_2$ are plotted in 3D space as function of Φ and x_1 as red circles; see Figure S12. Also plotted are CBMC campaign $f_t = 100\,\text{kPa};\quad \text{vary}\, y_2$, indicated by the green squares. Both CBMC data sets reside on a 3D surface mesh determined from the fitted NRTL parameters in Table S3. For construction of the 3D surface mesh, we vary parameters in the range as follows: $0.0001 < y_2 < 0.016;\quad 0.5 < f_t < 500\,\text{kPa}$. The 3D surface plot clearly shows that $\Phi \to 0;\quad \gamma_i \to 1;\quad G^{ex}/RT \to 0$. Also, for a fixed value of the surface potential, Φ we have the limiting characteristics: $x_i \to 1;\quad \gamma_i \to 1;\quad G^{ex}/RT \to 0$.

6.5 Radial Distribution Functions

The first step is to appreciate the preferential location of the guest molecules. Toward this end we determined the Radial Distribution Function (RDF) of guest-to-framework-atom distances of (a) guest CO_2, and (b) guest H_2O for adsorption of $CO_2(1)/H_2O(2)$ mixture adsorption in CALF-20 at 298 K. See Figure S3 and Table S1, for explanation of the labels for the framework atoms. The total fugacity in the bulk gas phase is 15 kPa with partial fugacities f_1 = 14.4 kPa, and f_2 =0.6 kPa. The RDFs were determined by sampling a total of 10^6 equilibrated simulation steps, and monitoring the guest-framework distances. The plotted RDF data has been normalized such that the area under each of the curves is identical to one another; the results are presented in Figure S15a,b. The first peaks of the RDFs for both guests correspond to the guest-oxygen atoms in the CALF-20 framework, indicating that the oxygen atoms of the oxalate groups of the framework serve as the most favorable binding sites for CO_2, and H_2O.

To investigate the possibility of non-homogeneous distribution of adsorbate guests, CBMC simulation data on the spatial locations of the guest molecules were sampled to determine the inter-molecular distances; these distances are determined from the center of gravity of each guest molecule. By sampling a total of 10^6 simulation steps, the radial distribution function (RDF) were determined for CH_4-CH_4, CH_4-H_2O, and H_2O-H_2O separation distances. Figure S16a,b plots the RDFs of center-to-center distances of CH_4-CH_4, CH_4-H_2O, and H_2O-H_2O pairs of guest CH_4 and H_2O molecules in CALF-20 at at 298 with

total fugacity in the bulk gas phase is 500 kPa with partial fugacities f_1 = 499.1 kPa, and f_2 =0.9 kPa, and $y_2 = \frac{f_2}{f_1 + f_2} = 0.0018$.

The simulation box contains a total of $5 \times 3 \times 5 = 75$ unit cells. Under these conditions the number of molecules in the simulation box of 75 unit cells: CH_4 = 128; H_2O = 22. Recall that 10^6 different conformations of the total of 119 + 44 = 163 molecules are analyzed. The samples were taken up to a radial distance of 30 Å, but the *x*-axis has been truncated at 12 Å because only the first few peaks are of interest in the discussions to follow. The plotted RDF data has been normalized such that the area under each of the curves is identical to one another. If we compare the first peaks, it is noteworthy that H_2O-H_2O pairs are close together at typical distances of about 3 Å. The CH_4-CH_4 pairs are typically 6.5 Å apart, occupying adjacent adsorption sites of CALF-20. The CH_4-H_2O pairs are typically 8 Å apart, occupying adjacent adsorption sites. This implies that the CH_4 molecules face a less severe competitive adsorption with H_2O than is anticipated by the IAST. The segregated nature of adsorbate locations are visually observed in Figure S13. This explains the finding in Figure S11b that $\%RH < 33\%; \quad x_1 > 0.2$, i.e. the adsorbed phase mixture is richer in CH_4 than is anticipated by the IAST; this is a direct consequence of the fact that CH_4 faces negligible competition with H_2O.

The proximity of H_2O-H_2O pairs observed in Figure S16a suggest the possibility of hydrogen bonding. To investigate this possibility, CBMC simulation data on the spatial locations of the guest molecules were sampled to determine the $O \cdots H$ distances of H_2O-H_2O and CO_2-H_2O pairs of molecules. By sampling a total of 10^6 simulation steps, the radial distribution functions (RDF) of O···H distances were determined for H_2O-H_2O and CO_2-H_2O pairs. Figure S16c plots the $O \cdots H$ of H_2O-H_2O pairs. We note the first peak in the RDFs for H_2O-H_2O pairs occurs at a distance of 2 Å, that is characteristic of hydrogen bonding.[15, 45]

To investigate the reasons behind the fact in Figure S11b with $\%RH > 33\%; \quad x_1 < 0.2$, i.e. the adsorbed phase mixture is poorer in CH_4 than is anticipated by the IAST, we determined the RDF for center-to-

center and $O\cdots H$ distances for adsorption of CH_4(1)/H_2O(2) mixture adsorption in CALF-20 at 298 K; the total fugacity in the bulk gas phase is 500 kPa with partial fugacities f_1 = 498.96 kPa, and f_2 =1.04 kPa and $y_2 = \frac{f_2}{f_1 + f_2} = 0.00208$.

Figure S17a presents the data on RDF for center-to-center distances of CH_4-H_2O, and H_2O-H_2O pairs. We note that the first peaks for both CH_4-H_2O, and H_2O-H_2O pairs occurs at distances of about 3 Å. This implies that CH_4 faces stiffer competitive adsorption with partner H_2O molecules because of the preponderance of H_2O within the framework. Observe also the snapshots in Figure S14. This explains the fact that for $y_2 > 0.00208; \%RH > 33\%; \quad x_1 < 0.2$, the adsorbed phase mixture is poorer in CH_4 than is anticipated by the IAST.

Figure S17b presents the data on RDF for $O\cdots H$ distances of H_2O-H_2O pairs. We note the first peak in the RDFs for H_2O-H_2O pairs occurs at a distance of 2 Å, that is characteristic of hydrogen bonding.[15, 45] Strong hydrogen bonding manifests for H_2O-H_2O pairs and serves to suppress the uptake of CH_4 below values anticipated by the IAST that does not cater for molecular clustering due to hydrogen bonding.

For further examples on the violation of the tenets of the IAST, watch the presentations titled **Dependence of Adsorption Selectivity on Mixture Composition, Hydrogen Bonding Influences on Adsorption, How Reliable is the IAST?, The Real Adsorbed Solution Theory, Co-operative Mixture Adsorption in Zeolites & MOFs, Azeotropic Adsorption, What is Azeotropic Adsorption, The Spreading Pressure Concept for Microporous Membranes**

on YouTube https://www.youtube.com/@rajamanikrishna250/videos

6.6 CBMC simulations for N_2/H_2O mixture adsorption

Figure S18a shows CBMC simulations of component loadings, q_i, for N_2(1)/H_2O(2) mixture adsorption in CALF-20 at 298 K at a total fugacity = 100 kPa. The mole fraction of H_2O in the bulk gas mixture, $y_2 = \frac{f_2}{f_1 + f_2}$, is varied. The loadings are plotted against $\%RH$. We note that the N_2/H_2O binary mixture

adsorption exhibits significant departures from thermodynamic idealities. Another way to demonstrate the non-idealities is to plot the mole fraction of N_2 in the adsorbed phase mixture, x_1, as a function of the $\%RH$, and y_2 see Figure S18b, c. We note that for $\%RH < 15\%; \quad y_2 < 0.004; \quad x_1 > 0.3$, the adsorbed phase mixture is richer in N_2, i.e. poorer in H_2O, than is anticipated by the IAST. On the other hand, for $\%RH > 15\%; \quad y_2 > 0.004; \quad x_1 < 0.3$, the adsorbed phase mixture is poorer in N_2, i.e. richer in H_2O, than is anticipated by the IAST.

In Figure S18d, the excess Gibbs free energy, G^{ex}/RT, is plotted as a function of $\%RH$. Figure S18e plots the activity coefficients as function of the adsorbed phase mole fraction of N_2, x_1.

Figure S19 presents computational snapshots showing the location of guest N_2 in CALF-20 at 298 K. The total fugacity in the bulk gas phase is 100 kPa with partial fugacities f_1 = 99.985 kPa, and f_2 = 0.015 kPa. The chosen conditions correspond to the scenario in Figure S18b with $\%RH < 15\%; \quad x_1 > 0.3$, i.e. the adsorbed phase mixture is richer in N_2 than is anticipated by the IAST.

Figure S20 shows computational snapshots showing the location of guest H_2O in CALF-20 at 298 K. The total fugacity in the bulk gas phase is 100 kPa with partial fugacities f_1 = 99.4 kPa, and f_2 =0.6 kPa. The chosen conditions to the scenario in Figure S18b with $\%RH > 15\%; \quad x_1 < 0.3$, i.e. the adsorbed phase mixture is poorer in N_2 than is anticipated by the IAST.

The values of the fitted NRTL parameters are specified in in Table S3.The continuous solid lines in Figure S18 are RAST calculations.

6.7 CBMC simulations for CO_2/H_2O mixture adsorption

Figure S21a shows CBMC simulations of component loadings, q_i, for $CO_2(1)/H_2O(2)$ mixture adsorption in CALF-20 at 298 K at a total fugacity = 15 kPa. The mole fraction of H_2O in the bulk gas mixture, y_2, is varied. The loadings are plotted against $\%RH$.

The dashed lines in Figure S21a are the IAST estimations. We note that the CO_2/H_2O binary mixture adsorption exhibits significant departures from thermodynamic idealities. Another way to demonstrate the non-idealities is to plot the mole fraction of CO_2 in the adsorbed phase mixture, x_1, as a function of the $\%RH$, and the mole fraction of H_2O in the bulk gas mixture, y_2; see Figure S21b,c. We note that for $\%RH < 20\%; \quad y_2 < 0.05; \quad x_1 > 0.3$, the adsorbed phase mixture is richer in CO_2, i.e. poorer in H_2O, than is anticipated by the IAST. On the other hand, for $\%RH > 20\%; \quad y_2 > 0.05; \quad x_1 < 0.3$, the adsorbed phase mixture is poorer in CO_2, i.e. richer in H_2O, than is anticipated by the IAST.

In Figure S21d, the excess Gibbs free energy, G^{ex}/RT, is plotted as a function of $\%RH$. Figure S21e plots the activity coefficients as function of the adsorbed phase mole fraction of CO_2, x_1.

The continuous solid lines in Figure S21 are RAST calculations with fitted NRTL parameters specified in Table S3.

Additionally, CBMC simulations for $CO_2(1)/H_2O(2)$ mixture adsorption in CALF-20 at 298 K were determined for varying total fugacity f_t, maintaining the mole fraction of H_2O in the bulk gas mixture at a constant value $y_2 = f_2/f_t = 0.05$. Figure S22 presents 3D plots of CBMC data on excess Gibbs free energy $\frac{G^{ex}}{RT} = x_1 \ln(\gamma_1) + x_2 \ln(\gamma_2)$ for $CO_2(1)/H_2O(2)$ mixture adsorption in CALF-20 at 298 K for two different campaigns, plotted as function of the surface potential, Φ, and the mole fraction of CO_2 in the adsorbed phase mixture, x_1. The 3D mesh is constructed using the NRTL parameters provided in Table S3. Both CBMC campaigns reside on the 3D surface mesh.

6.8 CBMC simulations for $CO_2/H_2O/CH_4$ mixture adsorption

Figure S23a presents CBMC simulations of component loadings, q_i, for $CO_2(1)/H_2O(2)/CH_4(3)$ mixture adsorption in CALF-20 at 298 K at a total fugacity $f_t = f_1 + f_2 + f_3 = 500\ \text{kPa}$, and partial fugacity of $CH_4(3)$ $f_3 = 400\ \text{kPa}$, plotted as a function of $\%RH$. The mole fraction of H_2O in the bulk gas mixture,

$y_2 = f_2/f_t$, is varied. Figure S23b,c,d plots the mole fractions of CO_2, H_2O, and CH_4 in the adsorbed phase mixture, x_i, as a function of $\%RH$. The dashed lines are the IAST estimations. We note that for $\%RH < 38\%$, the adsorbed phase is considerably richer in both $CO_2(1)$, and $CH_4(3)$ but poorer in $H_2O(2)$ than anticipated by the IAST. In contrast, for $\%RH > 38\%$, the adsorbed phase is considerably poorer in both $CO_2(1)$, and $CH_4(3)$ but richer in $H_2O(2)$ than anticipated by the IAST, implying the suppression of $CO_2(1)$, and $CH_4(3)$ uptakes due to preponderance of $H_2O(2)$ that is subjected to hydrogen bonding.

The continuous solid lines in Figure S23 are RAST calculations using eq (S22). In these calculations the NRTL parameters $\tau_{12}, \tau_{21}, \alpha_{12}, \tau_{23}, \tau_{32}, \alpha_{23}$ are taken to the same as for the corresponding binary pairs as listed in Table S3. Noteworthily, since the binary $CO_2(1)/CH_4(3)$ behaves ideally, we assert that $\tau_{13} = 0; \quad \tau_{31} = 0$.

The ternary NRTL model provides a reasonably good estimation of the mole fractions of the three guests in the adsorbed phase as function of the $\%RH$.

6.9 List of Tables for CBMC Simulations in CALF-20

Table S2. Dual-site Langmuir-Freundlich parameters for CO_2, CH_4, N_2, and H_2O determined from fitting unary isotherms determined at 298K from CBMC simulations in CALF-20. The goodness of fits are quantified by the values of R^2.

	Site A			Site B		
	$\frac{q_{A,sat}}{\text{mol kg}^{-1}}$	$\frac{b_A}{\text{Pa}^{-\nu_A}}$	ν_A	$\frac{q_{B,sat}}{\text{mol kg}^{-1}}$	$\frac{b_B}{\text{Pa}^{-\nu_B}}$	ν_B
CO_2 $R^2 = 0.999316$	1	4.693E-07	1	2.8	3.507E-04	1
H_2O $R^2 = 0.98238$	10.1	4.854E-29	10.5	1.3	1.888E-04	1.12
CH_4 $R^2 = 0.99887$	2.75	1.470E-05	1			
N_2 $R^2 = 0.999123$	2.8	2.849E-06	1			

Table S3. Fitted NRTL non-ideality parameters for binary mixture adsorption at 298 K in CALF-20.

	C / kg mol^{-1}	τ_{12}	τ_{21}	α
CO_2/H_2O	0.250	2.000	0.900	0.250
N_2/H_2O	0.110	4.924	10.079	0.117
CH_4/H_2O	0.250	2.000	2.000	0.100

6.10 List of Figures for CBMC Simulations in CALF-20

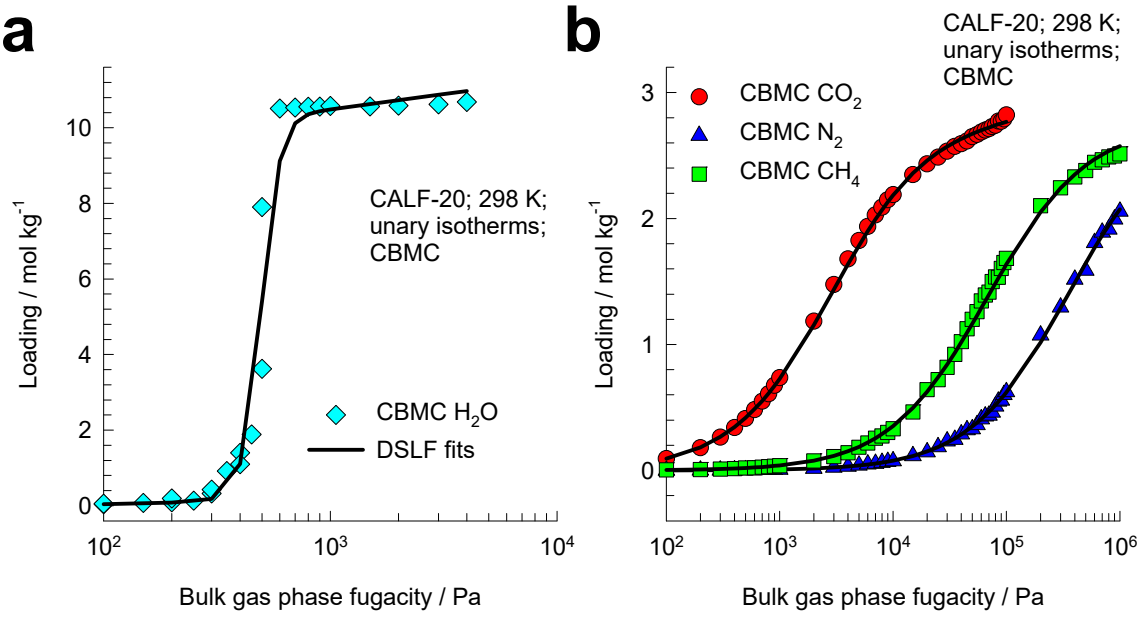

Figure S6. (a) CBMC simulations for unary CO_2, CH_4, N_2, and H_2O isotherms at 298 K. The unary isotherm dual-site Langmuir-Freundlich fit parameters are provided in Table S2.

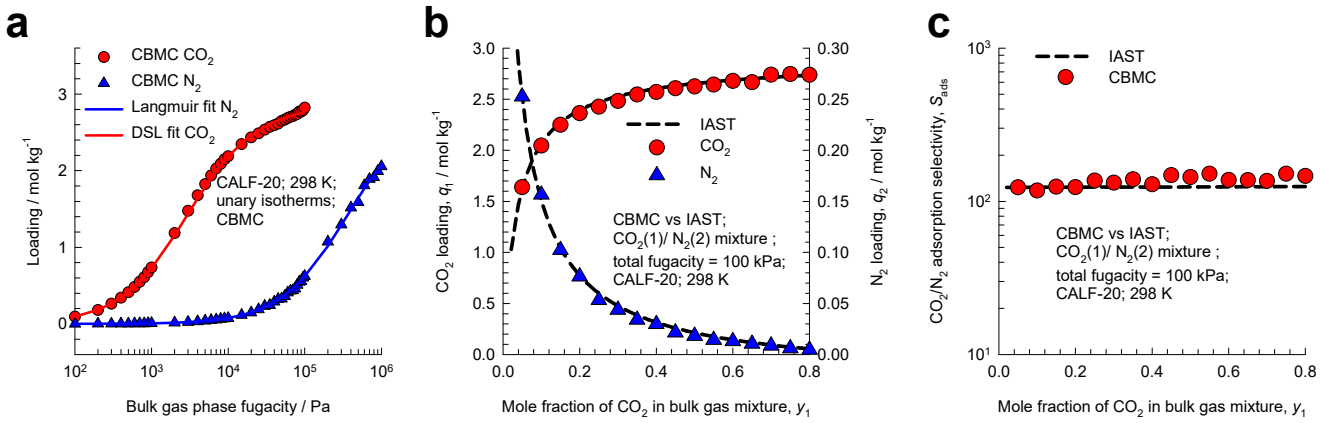

Figure S7. (a) CBMC simulations for unary CO_2 and N_2 isotherms at 298 K. (b) CBMC simulations of component loadings, q_i, for $CO_2(1)/N_2(2)$ mixture adsorption in CALF-20 at a total pressure of 100 kPa and 298 K; the mole fraction of $CO_2(1)$ in the bulk gas phase mixture, y_1, is varied from 0 to 1. The dashed lines are the IAST estimations. (c) Plot of $CO_2(1)/N_2(2)$ adsorption selectivity from CBMC simulations with IAST estimates.

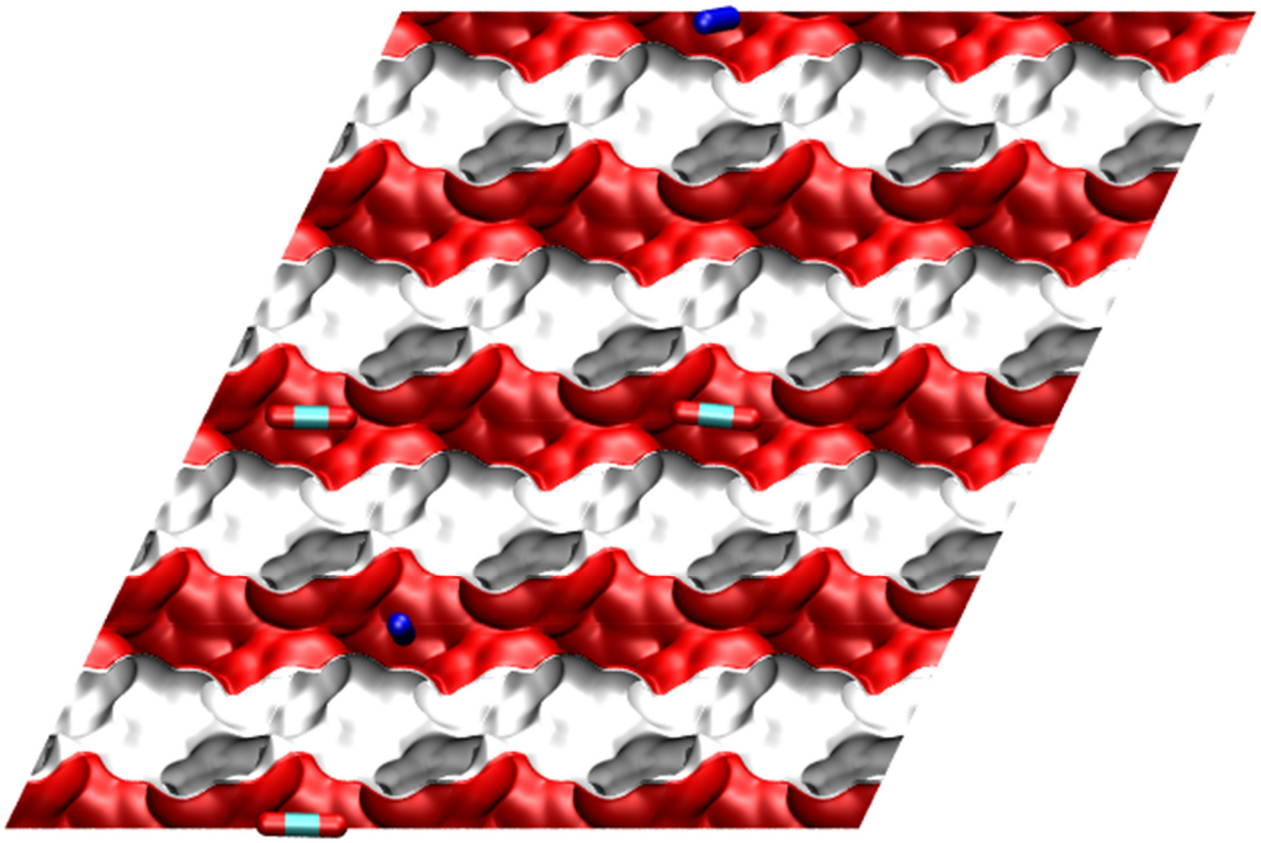

Figure S8. Computational snapshots showing the location of guest CO_2 and N_2 (blue pencil like molecule) in CALF-20 at 298 K. The total fugacity in the bulk gas phase is 100 kPa with partial fugacities f_1 = 5 kPa, and f_2 =95 kPa.

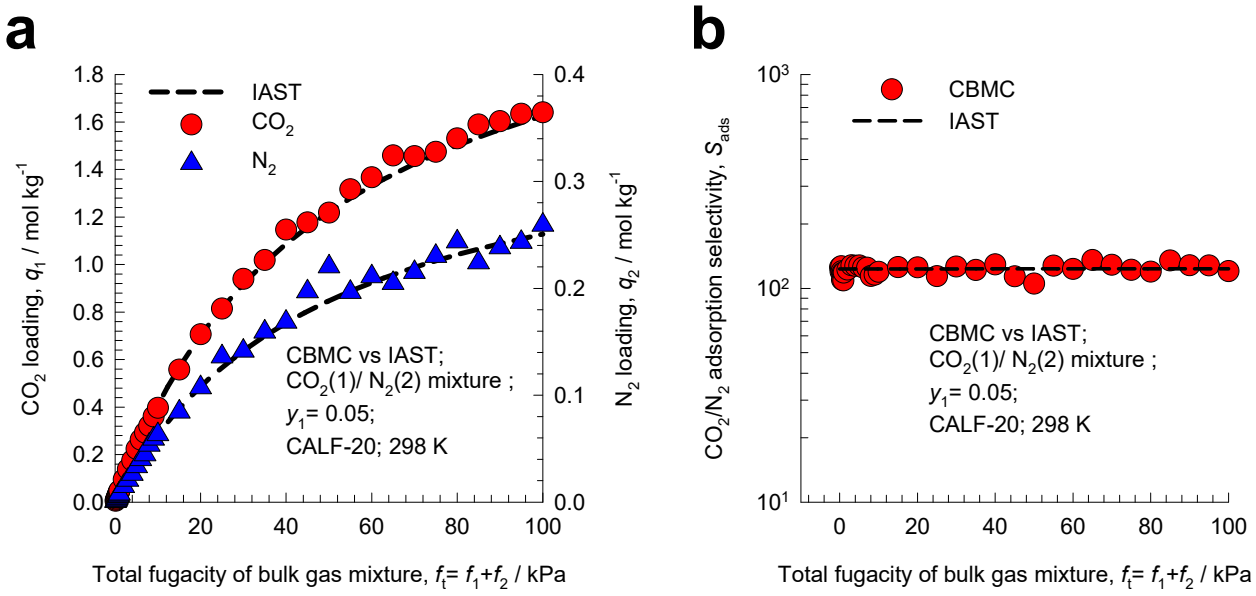

Figure S9. (a) CBMC simulations of component loadings, q_i, for CO2(1)/N2(2) mixture adsorption in CALF-20 at 298 K with varying total fugacity f_t, maintaining the mole fraction of CO2 in the bulk gas mixture at a constant value $y_2 = f_2/f_t = 0.05$. The dashed lines are the IAST estimations. (b) Plot of CO2(1)/N2(2) adsorption selectivity from CBMC simulations with IAST estimates.

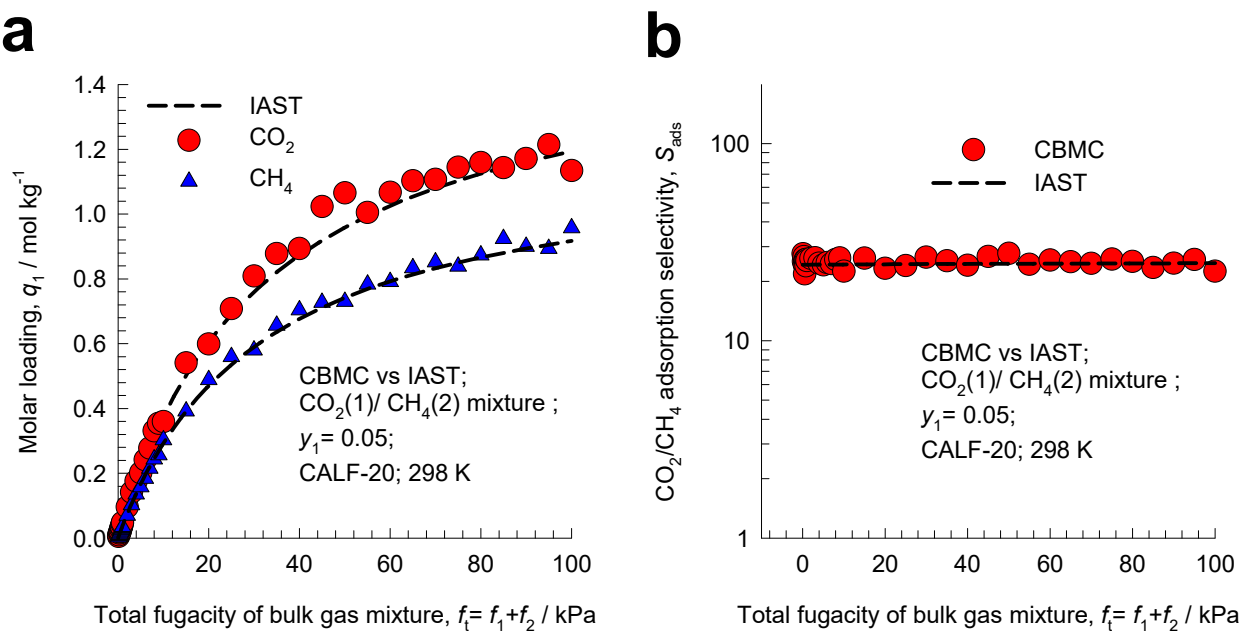

Figure S10. (a) CBMC simulations of component loadings, q_i, for CO_2(1)/CH_4(2) mixture adsorption in CALF-20 at 298 K with varying total fugacity f_t, maintaining the mole fraction of CO_2 in the bulk gas mixture at a constant value $y_2 = f_2/f_t = 0.05$. The dashed lines are the IAST estimations. (b) Plot of CO_2(1)/CH_4(2) adsorption selectivity from CBMC simulations with IAST estimates.

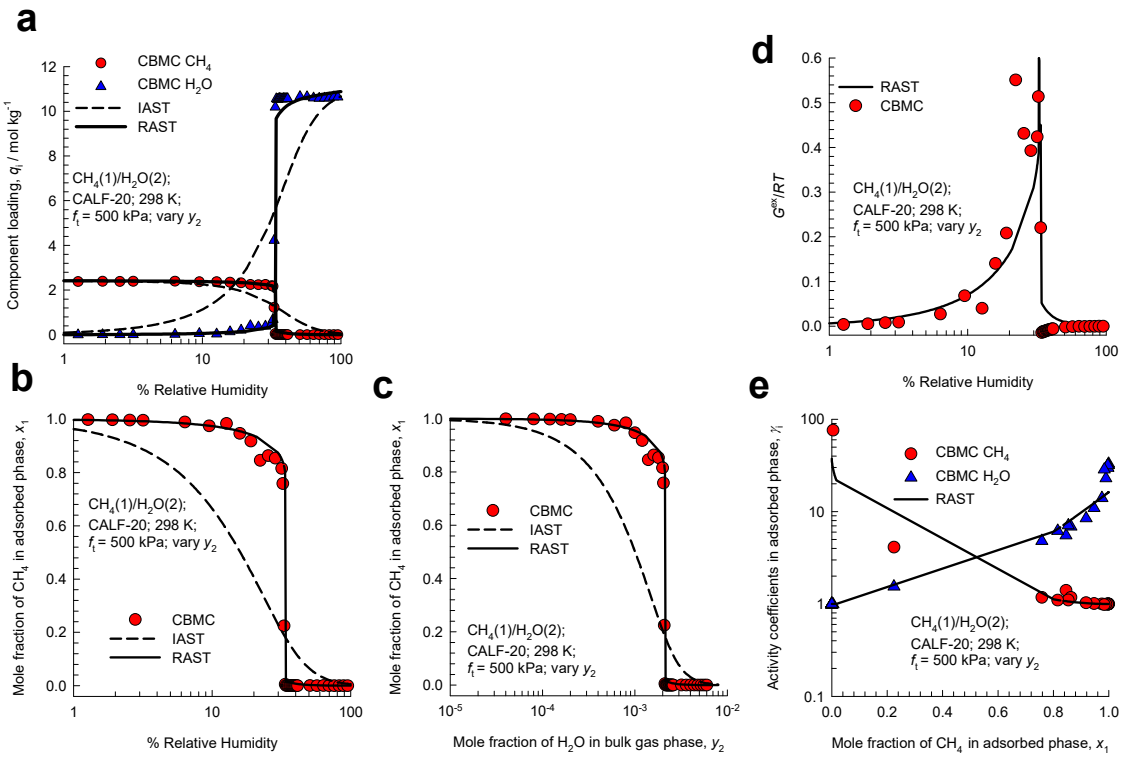

Figure S11. (a) CBMC simulations of component loadings, q_i, for CH4(1)/H2O(2) mixture adsorption in CALF-20 at 298 K at a total fugacity f_t = 500 kPa, plotted as a function of %RH. (b, c) Plot of the mole fraction of CH4 in the adsorbed phase mixture, x_1, as a function of the %RH, and y_2. (d) Plot of the G^{ex}/RT vs %RH. (e) Plot of γ_i as a function of x_1. The continuous solid lines are the RAST calculations; the fitted NRTL parameters are specified in Table S3. The dashed lines are the IAST estimations.

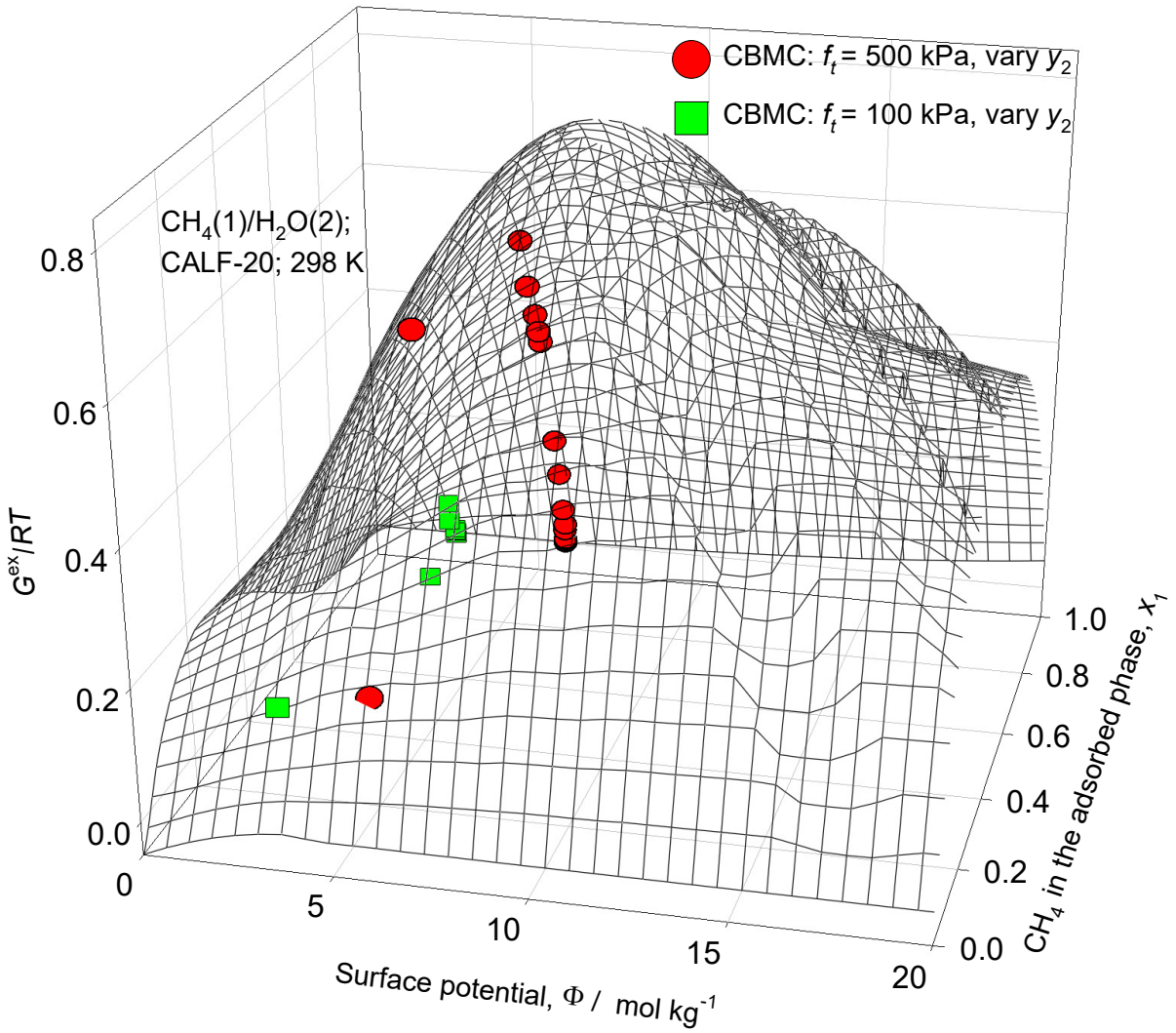

Figure S12. 3D plots of CBMC data on excess Gibbs free energy $\frac{G^{ex}}{RT} = x_1 \ln(\gamma_1) + x_2 \ln(\gamma_2)$ for CH_4(1)/H_2O(2) mixture adsorption in CALF-20 at a total fugacities f_t = 500 kPa, and f_t = 100 kPa, plotted as function of the surface potential, Φ, and the mole fraction of CH_4 in the adsorbed phase mixture, x_1. The 3D mesh is constructed using the NRTL parameters provided in Table S3.

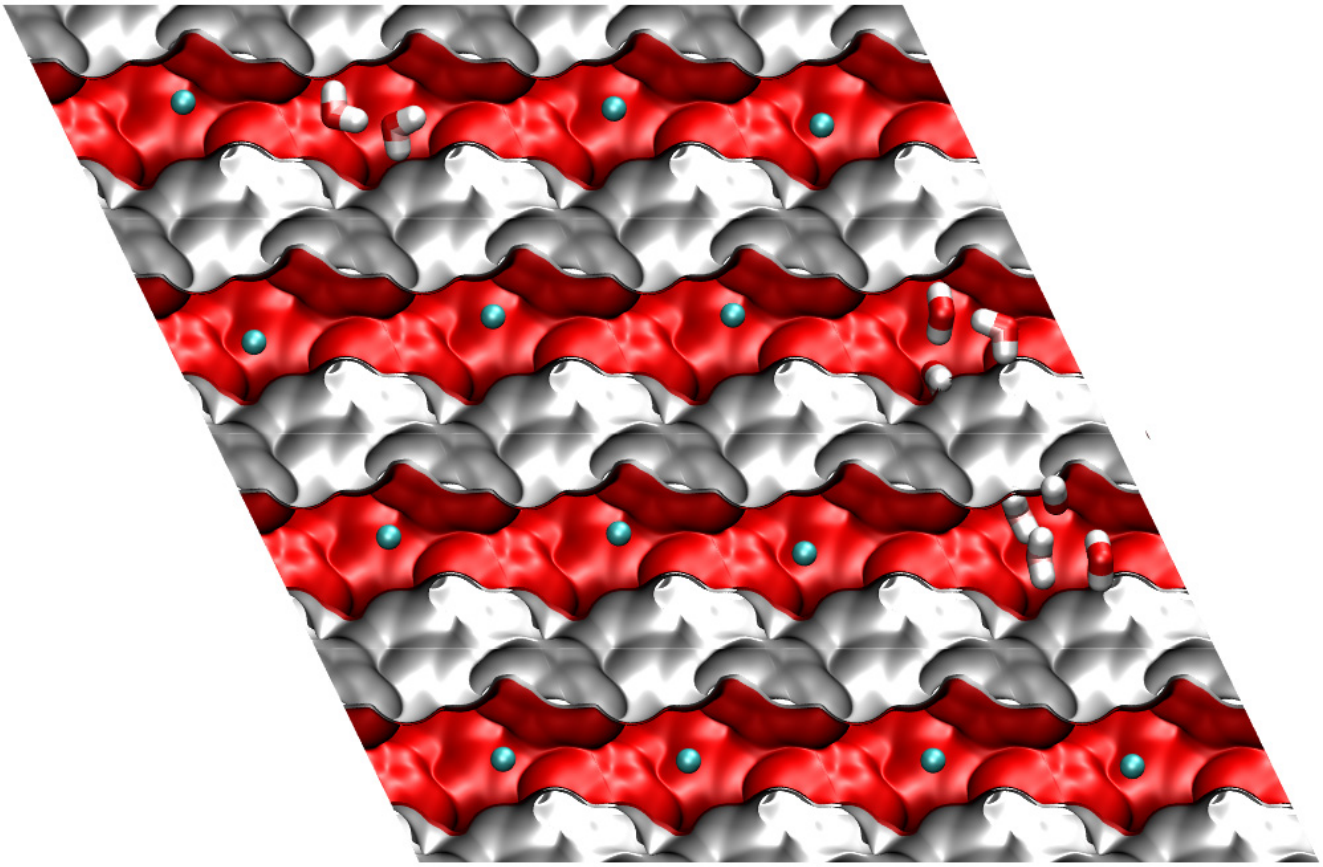

Figure S13. Computational snapshots showing the location of guest CH_4 and H_2O molecules in CALF-20 at at 298 K. The total fugacity in the bulk gas phase is 500 kPa with partial fugacities f_1 = 499.1 kPa, and f_2 =0.9 kPa.

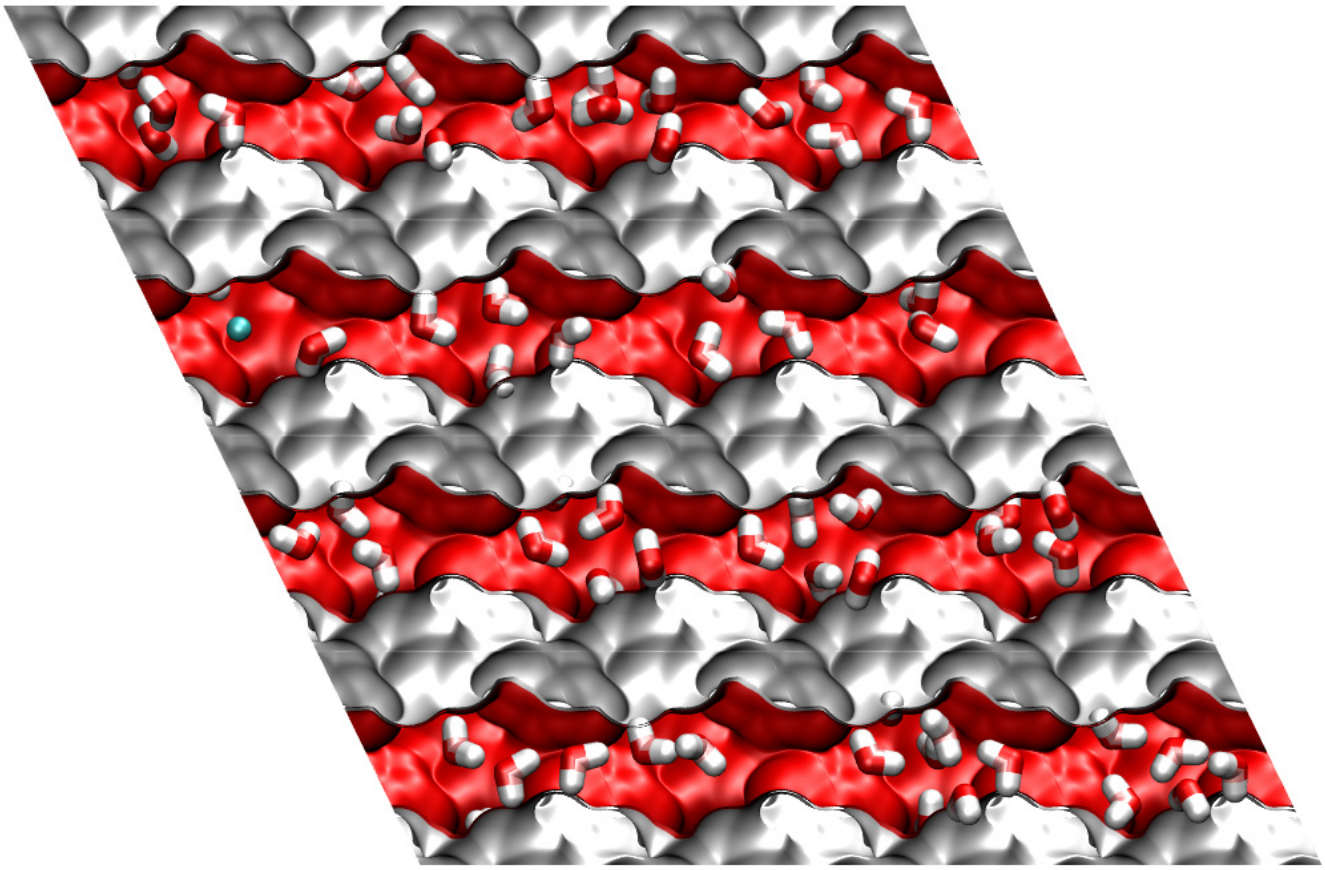

Figure S14. Computational snapshots showing the location of guest CH_4 and H_2O in in CALF-20 at 298 K. The total fugacity in the bulk gas phase is 500 kPa with partial fugacities f_1 = 498.96 kPa, and f_2 =1.04 kPa.

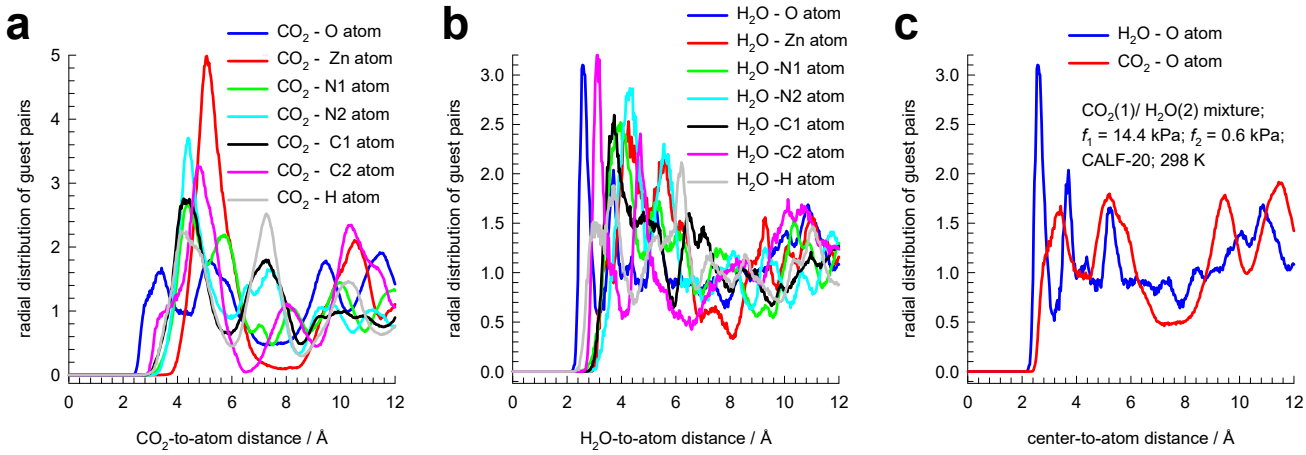

Figure S15. (a, b) Radial Distribution Function (RDF) of guest-to-framework-atom distances of (a) guest CO_2, and (b) guest H_2O for adsorption of CO_2(1)/H_2O(2) mixture adsorption in CALF-20 at 298 K. See Figure S3 and Table S1, for explanation of the labels for the framework atoms. The total fugacity in the bulk gas phase is 15 kPa with partial fugacities f_1 = 14.4 kPa, and f_2 =0.6 kPa. The plotted RDF data has been normalized such that the area under each of the curves is identical to one another. (c) Radial Distribution Function (RDF) of guest-to-oxygen atom distances of CO_2, and H_2O guests.

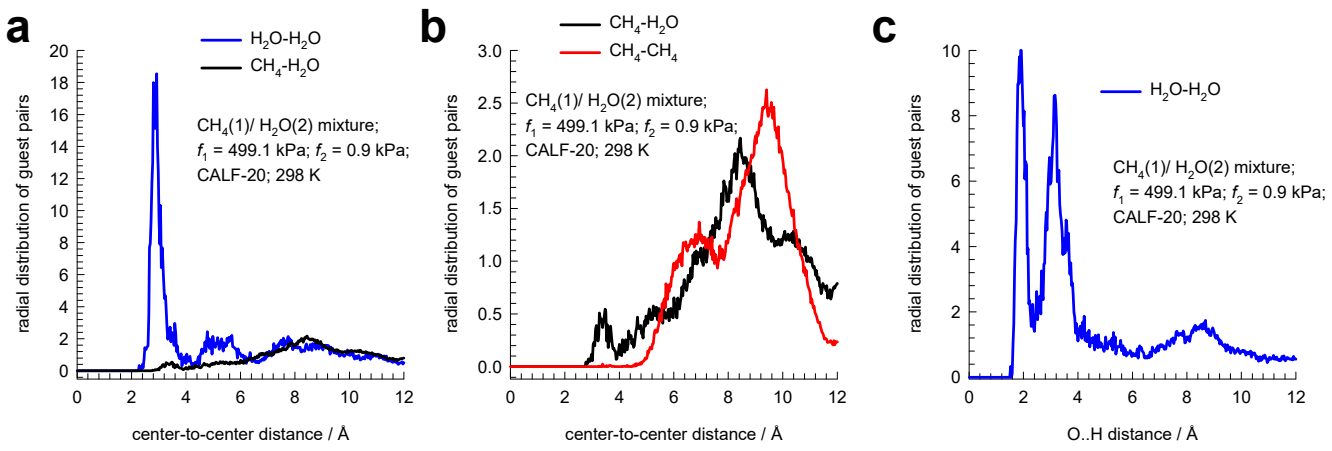

Figure S16. (a, b, c) Radial Distribution Function (RDF) of center-to-center distances of CH_4-CH_4, CH_4-H_2O, and H_2O-H_2O pairs, and (c) $O\cdots H$ of H_2O-H_2O pairs, determined from CBMC simulations for adsorption of CH_4(1)/H_2O(2) mixture adsorption in CALF-20 at 298 K. guest CH_4 and H_2O molecules in CALF-20 at at 298 K. total fugacity in the bulk gas phase is 500 kPa with partial fugacities f_1 = 499.1 kPa, and f_2 =0.9 kPa. The plotted RDF data has been normalized such that the area under each of the curves is identical to one another.

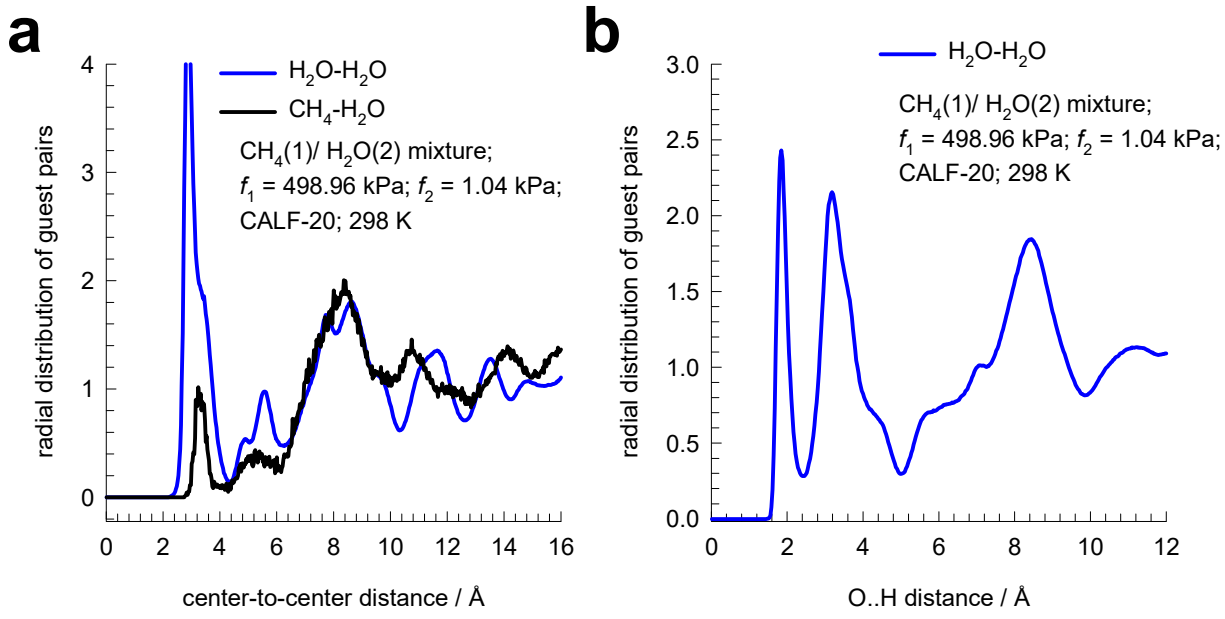

Figure S17. Radial Distribution Function (RDF) of (a) center-to-center distances, and (b) O···H of CH_4-H_2O, and H_2O-H_2O pairs, determined from CBMC simulations for adsorption of CH_4(1)/H_2O(2) mixture adsorption in CALF-20 at 298 K. The total fugacity in the bulk gas phase is 500 kPa with partial fugacities f_1 = 498.96 kPa, and f_2 =1.04 kPa. The plotted RDF data has been normalized such that the area under each of the curves is identical to one another.

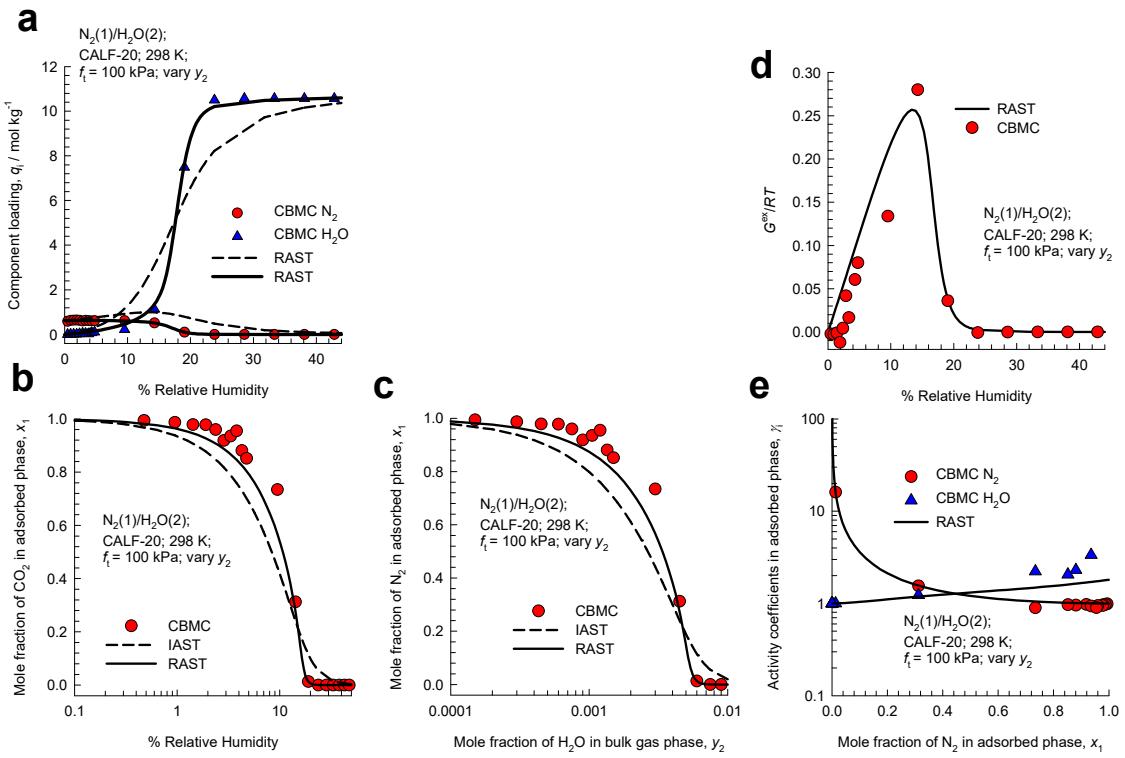

Figure S18. (c) CBMC simulations of component loadings, q_i, for N2(1)/H2O(2) mixture adsorption in CALF-20 at 298 K at a total fugacity f_t = 100 kPa, plotted as a function of %RH. (b, c) Plot of the mole fraction of N2 in the adsorbed phase mixture, x_1, as a function of the %RH, and y_2. (d) Plot of the G^{ex}/RT vs %RH. (e) Plot of γ_i as a function of x_1. The continuous solid lines are the RAST calculations; the fitted NRTL parameters are specified in Table S3. The dashed lines are the IAST estimations.

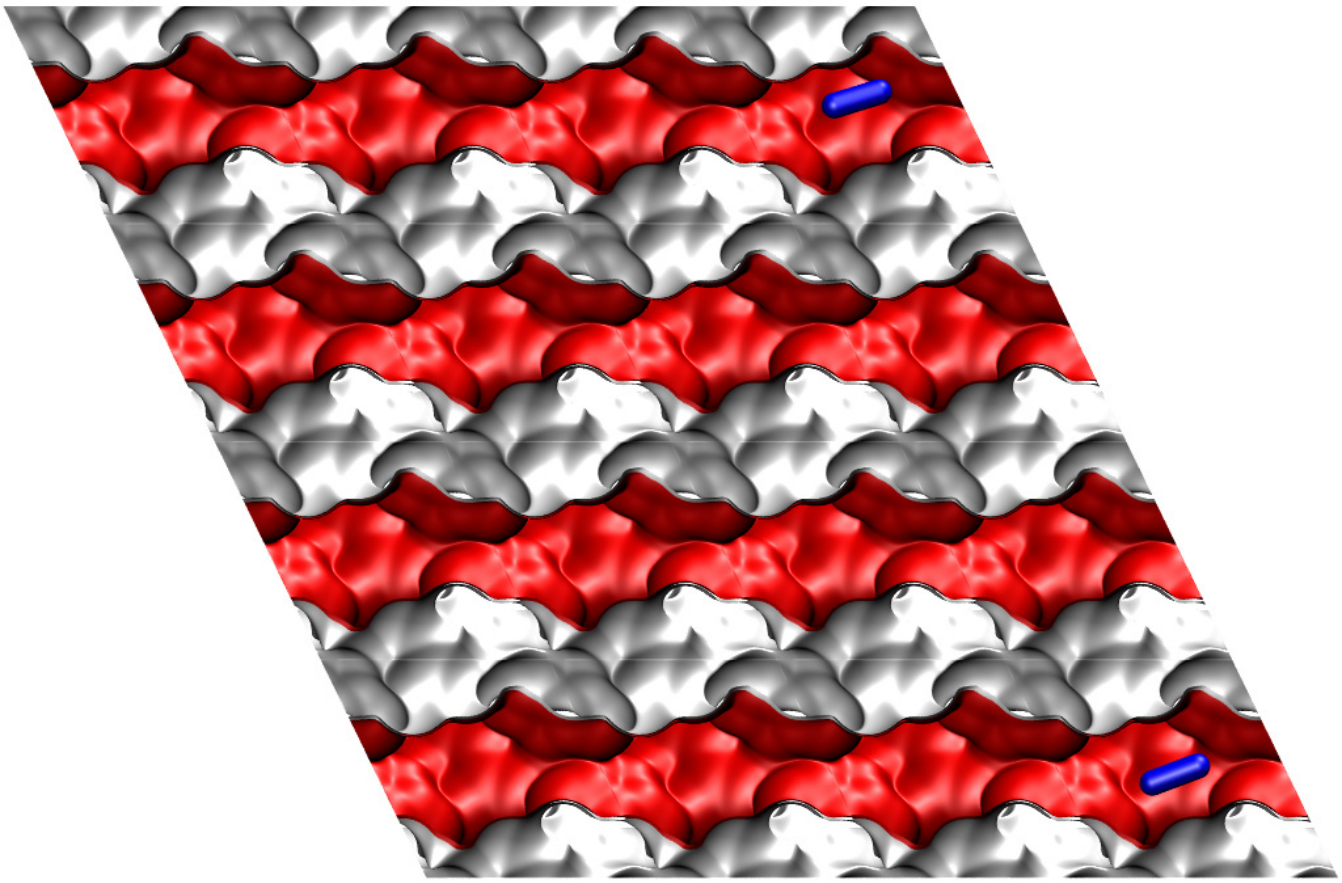

Figure S19. Computational snapshots showing the location of guest N_2 and H_2O in CALF-20 at 298 K. The total fugacity in the bulk gas phase is 100 kPa with partial fugacities f_1 = 99.985 kPa, and f_2 =0.015 kPa.

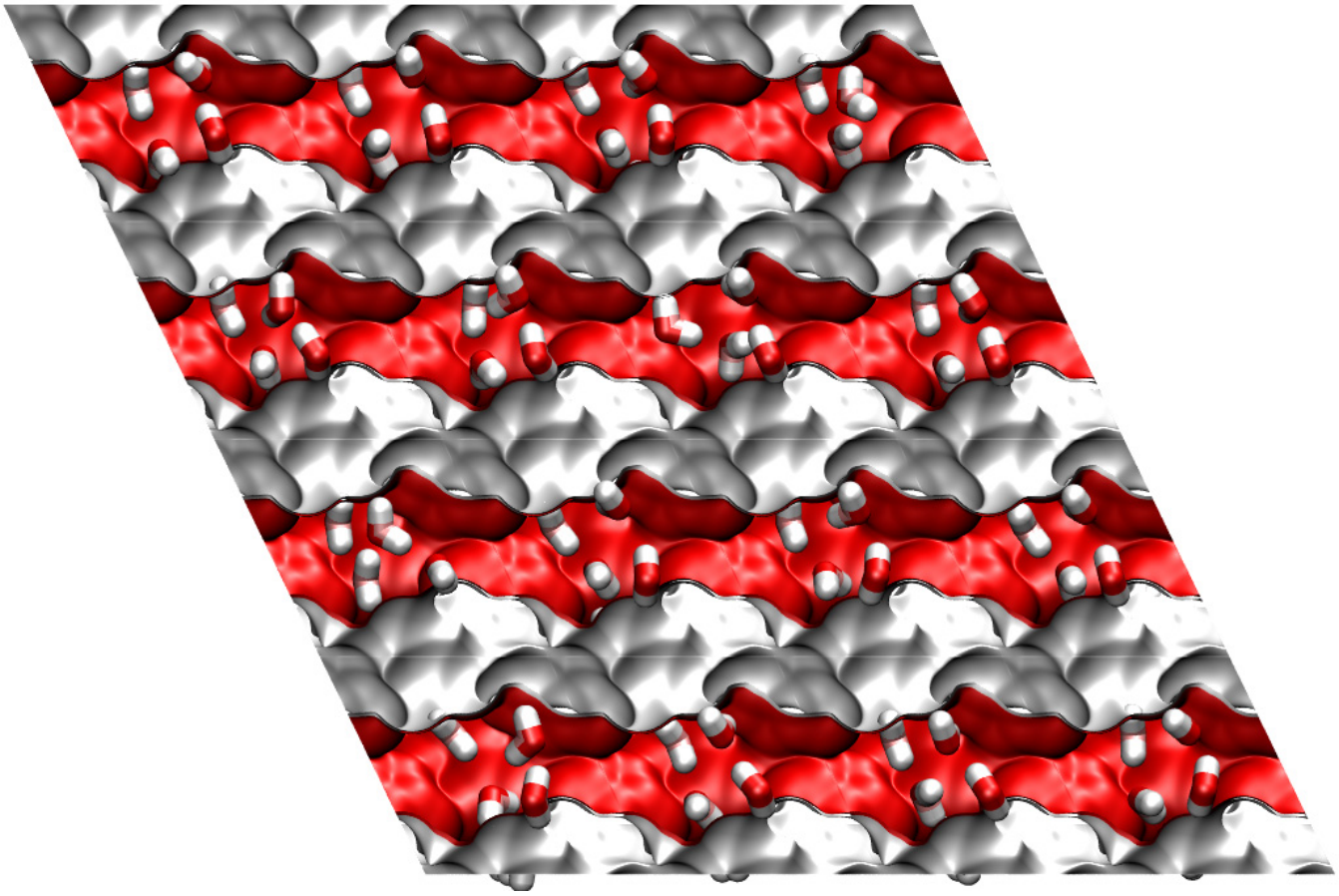

Figure S20. Computational snapshots showing the location of guest N_2 and H_2O in CALF-20 at 298 K. The total fugacity in the bulk gas phase is 100 kPa with partial fugacities f_1 = 99.4 kPa, and f_2 =0.6 kPa.

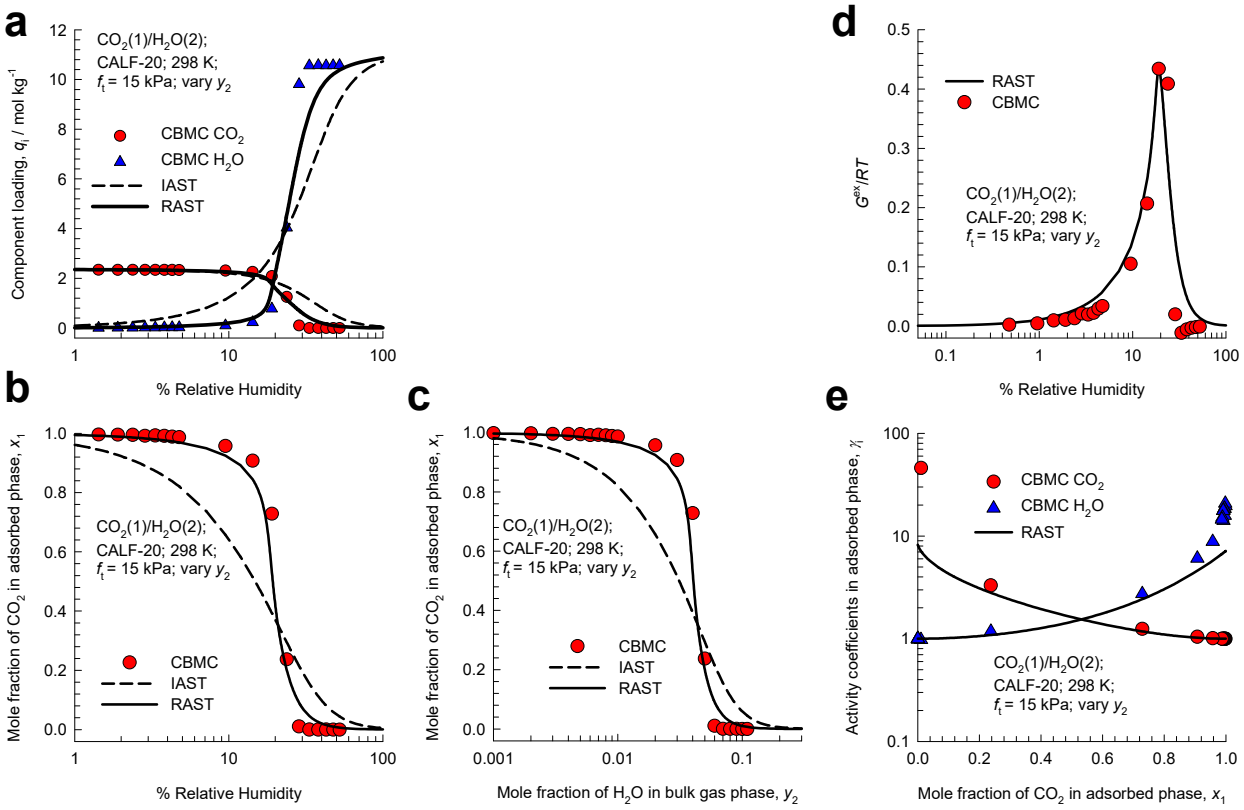

Figure S21. (a) CBMC simulations of component loadings, q_i, for CO2(1)/H2O(2) mixture adsorption in CALF-20 at 298 K at a total fugacity f_t = 15 kPa, plotted as a function of %RH. The mole fraction of H2O in the bulk gas mixture, $y_2 = f_2/f_t$, is varied. (b, c) Plot of the mole fraction of CO2 in the adsorbed phase mixture, x_1, as a function of the %RH, and y_2. (d) Plot of the G^{ex}/RT vs %RH. (e) Plot of γ_i as a function of x_1. The continuous solid lines are the RAST calculations; the fitted NRTL parameters are specified in Table S3. The dashed lines are the IAST estimations.

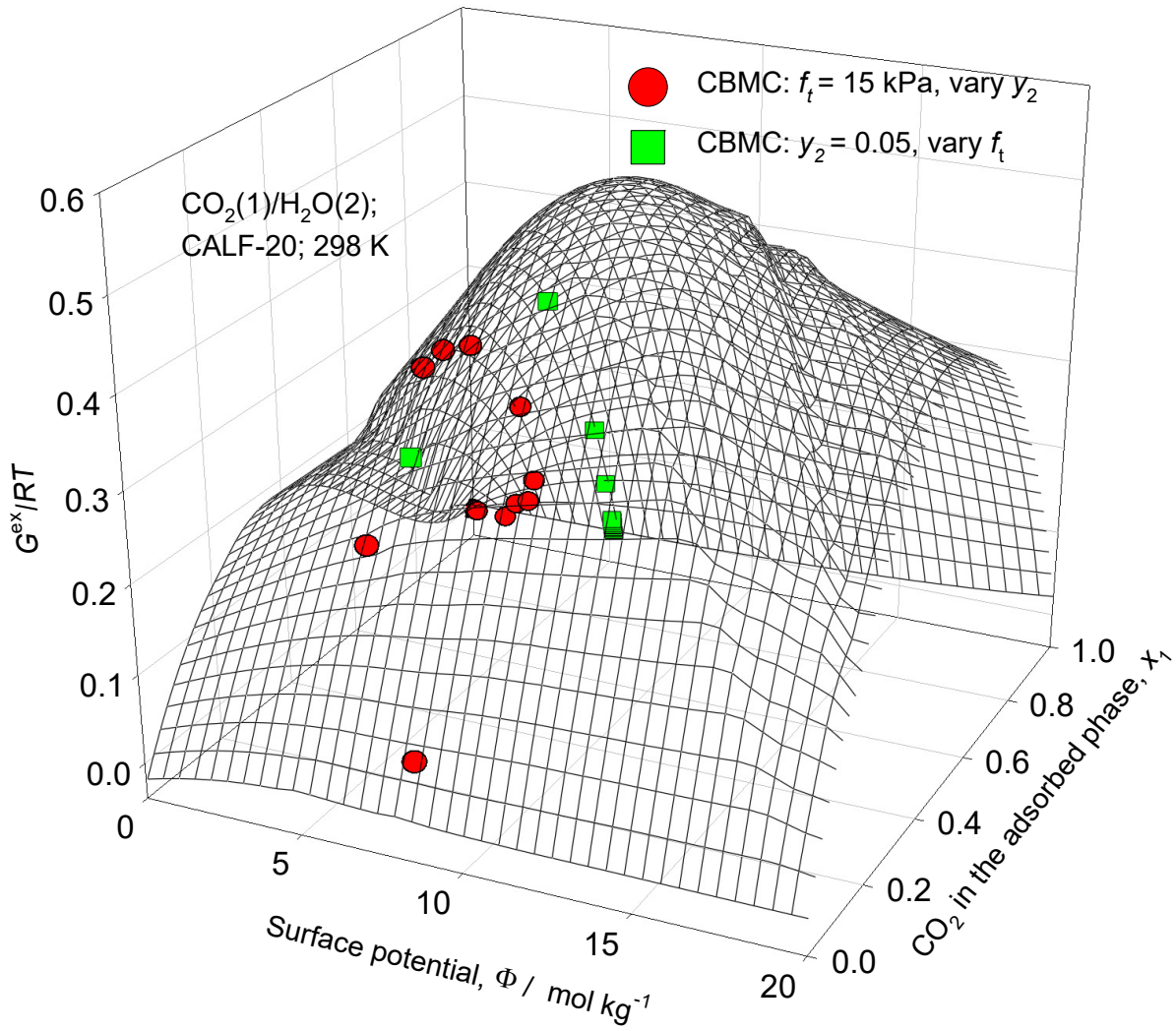

Figure S22. 3D plots of CBMC data on excess Gibbs free energy $\frac{G^{ex}}{RT} = x_1 \ln(\gamma_1) + x_2 \ln(\gamma_2)$ for CO_2(1)/H_2O(2) mixture adsorption in CALF-20 at 298 K for two different campaigns, plotted as function of the surface potential, Φ , and the mole fraction of CO_2 in the adsorbed phase mixture, x_1. The 3D mesh is constructed using the NRTL parameters provided in Table S3.

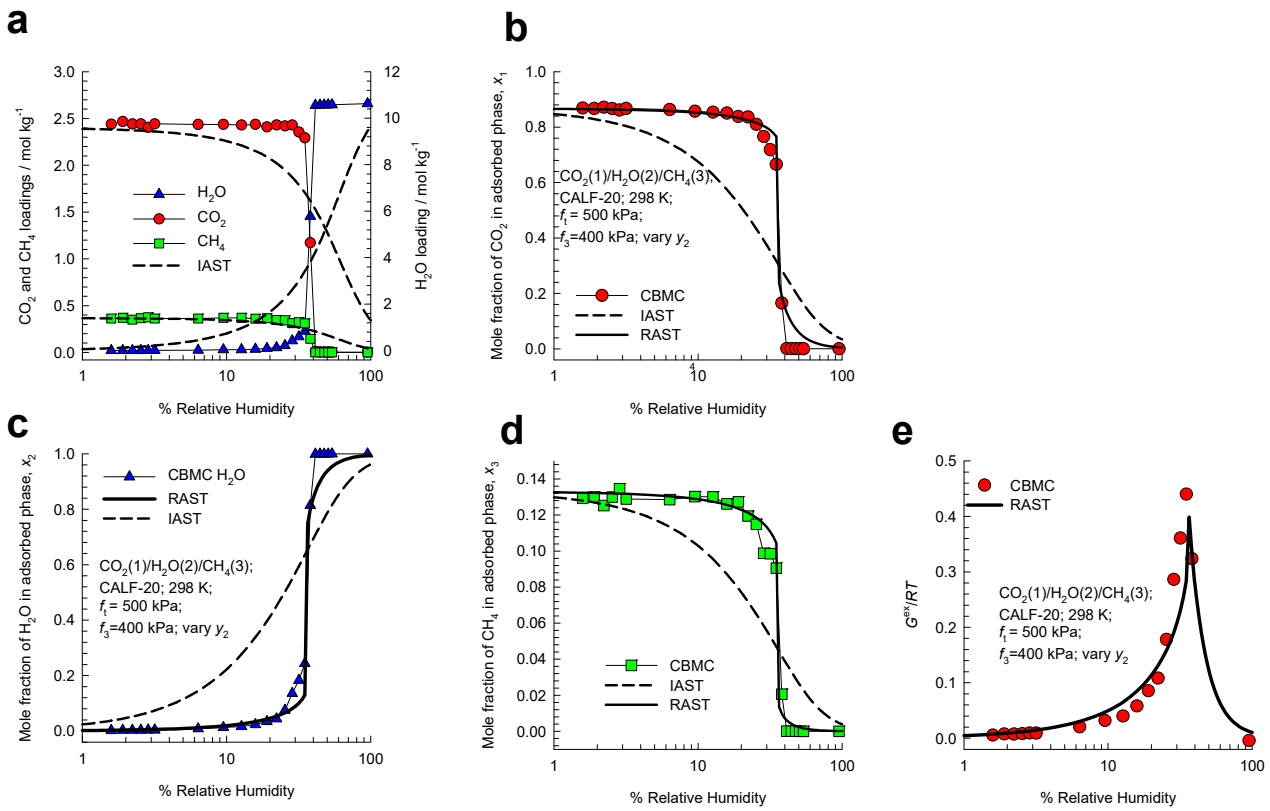

Figure S23. (a) CBMC simulations of component loadings, q_i, for CO2(1)/H2O(2)/CH4(3) mixture adsorption in CALF-20 at 298 K at a total fugacity $f_t = f_1 + f_2 + f_3 = 500\ \text{kPa}$, and partial fugacity of CH4(3) $f_3 = 400\ \text{kPa}$, of plotted as a function of %RH. The mole fraction of H2O in the bulk gas mixture, $y_2 = f_2 / f_t$, is varied. (b, c, d) Plot of the mole fractions of CO2, H2O, and CH4 in the adsorbed phase mixture, x_i, as a function of %RH. (e) Plot of the G^{ex}/RT as function of %RH. The continuous solid lines are the RAST calculations; the fitted NRTL parameters are specified in Table S3. The dashed lines are the IAST estimations.

7 RAST Modelling of Transient Breakthroughs in Fixed Beds

We summarize below the simulation methodology used to perform transient breakthrough calculations for fixed bed adsorbers. The simulation methodology is the same as described by Krishna. [46-49] Our earlier work[27] provides validation of the simulations methodology by comparison with experimental breakthrough data of Nguyen et al.[50] on the influence of %RH on transient CO_2/H_2O mixture breakthroughs in a laboratory scale fixed bed packed with CALF-20 composites (80% MOF:20% polysulfone).

In an *n*-component gas mixtures in plug flow through a fixed bed maintained under isothermal conditions, the molar concentrations in the gas phase at any position and instant of time are obtained by solving the following set of partial differential equations for each of the species *i* in the gas mixture

$$\frac{\partial c_i(t,z)}{\partial t}+\frac{\partial\left(v(t,z)c_i(t,z)\right)}{\partial z}+\frac{\left(1-\varepsilon\right)}{\varepsilon}\rho\frac{\partial \bar{q}_i(t,z)}{\partial t}=0;\quad i=1,2,...n \tag{S27}$$

In eq (S27), t is the time, z is the distance along the adsorber, ρ is the framework density, ε is the bed voidage, v is the interstitial gas velocity, and $\bar{q}_i(t,z)$ is the *spatially averaged* molar loading within the crystallites of radius r_c, monitored at position z, and at time t. At time, $t = 0$, the inlet to the adsorber, $z = 0$, is subjected to a step input of the *n*-component gas mixture and this step input is maintained till the end of the adsorption cycle when steady-state conditions are reached.

$$t\geq 0;\quad p_i(0,t)=p_{i0};\quad u(0,t)=u_0 \tag{S28}$$

The *interstitial* gas velocity is related to the *superficial* gas velocity by

$$v=\frac{u}{\varepsilon} \tag{S29}$$

where $u_0=v\varepsilon$ is the superficial gas velocity at the inlet to the adsorber. The superficial gas velocity is calculated from the flow rate of the gas mixture entering the breakthrough tube.

The radial distribution of molar loadings, q_i, within a crystallite of radius r_c, is obtained from a solution of a set of differential equations describing the uptake

$$\rho \frac{\partial q_i(r,t)}{\partial t} = -\frac{1}{r^2}\frac{\partial}{\partial r}\left(r^2 N_i\right) \tag{S30}$$

The intra-crystalline fluxes N_i in eq (S30) are related to gradients in the molar gradients of the loadings [33, 34, 46, 51]

$$N_i = -\rho Đ_i \frac{\partial q_i}{\partial r}; \qquad i = 1, 2, ..n \tag{S31}$$

In eqs (S30) and (S31), R is the gas constant, T is the temperature, ρ represents the framework density of the microporous crystalline material, r is the radial distance coordinate, and the component loadings q_i are defined in terms of moles per kg of framework. The $Đ_i$ characterize and quantify the interaction between species i and pore walls. The M-S diffusivity $Đ_i$ equals the corresponding diffusivity for a unary system, determined at the same pore occupancy.[51] Furthermore, the M-S diffusivity $Đ_i$ for any species i in a mixture remains invariant to choice of the partner(s) species.[51]

At any time, t, during the transient approach to thermodynamic equilibrium, the spatial-averaged component loading within the crystallites of radius r_c is calculated using

$$\bar{q}_i(t) = \frac{3}{r_c^3}\int_0^{r_c} q_i(r,t) r^2 dr \tag{S32}$$

Summing eq (S32) over all n species in the mixture allows calculation of the *total average* molar loading of the mixture within a crystallite

$$\bar{q}_t(t,z) = \sum_{i=1}^{n} \bar{q}_i(t,z) \tag{S33}$$

The term $\frac{\partial \bar{q}_i(t,z)}{\partial t}$ in eq (S27) is determined by solving the set of eqs (S30), (S31), (S32), and (S33). At any time t, and position z, the component loadings at the outer surface of the particle $q_i(r_c,t,z)$ is in equilibrium with the bulk phase gas mixture with partial pressures $p_i(t,z)$ in the bulk gas mixture. the

component loadings at the surface of the crystallites $q_i(r_c,t,z)$ where r_c is the radius of the crystallites are calculated using the RAST. To demonstrate the influence of thermodynamic non-idealities, we also perform simulations using the IAST.

If the value of $Đ_i/r_c^2$ is large enough to ensure that intra-crystalline gradients are absent and the entire crystallite particle can be considered to be in thermodynamic equilibrium with the surrounding bulk gas phase at that time t, and position z of the adsorber

$$\bar{q}_i(t,z) = q_i(t,z) \tag{S34}$$

In the simulations reported in this work, the value of $Đ_i/r_c^2$ = 1 s^{-1} for each of the guest molecules.

Further details of the numerical procedures used in solving the partial differential equations, are provided by Krishna and co-workers.[46-49] For further explanation, including video animations of breakthroughsm watch the presentations titled **Diffusional Influences on Breakthroughs, Transient Breakthrough Simulations, Modeling of Fixed Bed Adsorbers** on YouTube https://www.youtube.com/@rajamanikrishna250/videos

For the simulations presented here we take the following bed dimensions

Cross-sectional area of tube: $A = \left(\pi d^2/4\right)$ = 1 m^2

Effective length of packed column: L = 0.3 m

Voidage of packed bed; ε = 0.4

The interstitial gas velocity t the entrance to the tube $v = \frac{u}{\varepsilon} = \frac{Q_0}{A\varepsilon}$ = 0.1 m s^{-1}. The volumetric flow rate of the gas mixture at the inlet of the fixed bed Q_0 = 40 L s^{-1}.

The total volume of the bed is $V_{bed} = LA$. The volume of CALF-20 used in the simulations is $V_{ads} = LA(1-\varepsilon)$ = 0.18 m^3. The crystallite density of CALF-20 ρ = 1598.0 kg m^{-3}. The mass of the CALF-20 in the packed bed: $m_{ads} = \rho LA(1-\varepsilon)$ = 287.8 kg.

Simulations were performed for CO_2/H_2O and CH_4/H_2O mixtures at a temperature of 298 K with the values %Relative Humidity = 5%, 25%, and 40%. At 298 K, p_2^{sat} is determined from the Antoine equation: $p_2^{sat} = 3150$ Pa. The partial pressures of H_2O in the feed mixture is calculated using $\%\text{Relative Humidity} = \frac{p_2}{p_2^{sat}} \times 100$.

For description of thermodynamic non-idealities, we use a set of fitted NRTL parameters are specified in Table S3.

Figure S24a,b,c compares breakthrough simulations using RAST (continuous colored lines) and IAST (dashed lines) for CH_4/H_2O mixtures at 298 K and total fugacity f_t = 500 kPa, with three different values of %Relative Humidity. The transient breakthrough data for the dimensionless concentrations at the exit of the fixed bed, c_i/c_{i0}, are plotted as a function of a modified time parameter defined by

$$\frac{\left(Q_0 = \text{flow rate L s}^{-1}\right) \times \left(\text{time in s}\right)}{\left(\text{kg CALF-20 packed in tube}\right)} = \frac{Q_0 t}{m_{ads}} = \text{L kg}^{-1} \qquad \text{(S35)}$$

Noteworthily, the breakthrough characteristics of H_2O are particularly sensitive to thermodynamic non-idealities. To accentuate the differences between the IAST and RAST calculations of breakthroughs, the spatially-averaged component loadings in the bed are plotted in Figure S24d,e,f as function of $\frac{Q_0 t}{m_{ads}}$. For %RH = 5%, and 25% the RAST anticipates the adsorbed phase to be significantly richer in CH_4, i.e. poorer in H_2O, than predicted by the IAST. For %RH = 40 %, the RAST anticipates the adsorbed phase to be significantly poorer in CH_4, i.e. richer in H_2O, than predicted by the IAST. These findings rhyme with the data plotted in in Figure S11.

Figure S25a,b,c compares breakthrough simulations using RAST (continuous colored lines) and IAST (dashed lines) for CO_2/H_2O mixtures at 298 K and total fugacity f_t = 100 kPa, with three different values of %Relative Humidity. To accentuate the differences between the IAST and RAST calculations of breakthroughs, the averaged component loadings in the bed are plotted in Figure S25d,e,f as function of

$\frac{Q_0 t}{m_{ads}}$. For %RH = 5%, and 25% the RAST anticipates the adsorbed phase to be significantly richer in CO_2, i.e. poorer in H_2O, than predicted by the IAST. For %RH = 40 %, the RAST anticipates the adsorbed phase to be significantly poorer in CO_2, i.e. richer in H_2O, than predicted by the IAST. These findings rhyme with the data plotted in Figure S21.

7.1 List of Figures for RAST Modelling of Transient Breakthroughs in Fixed Beds

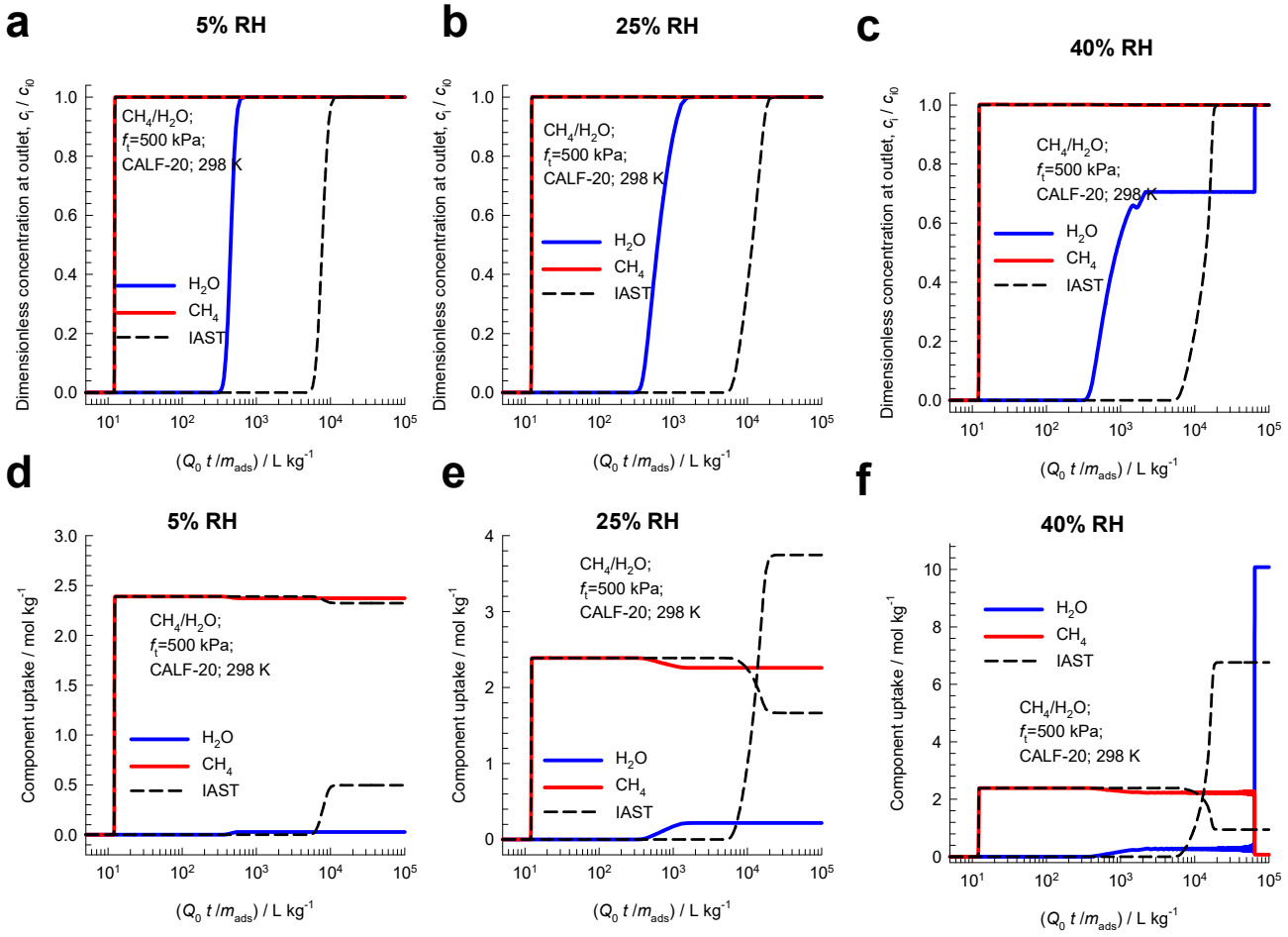

Figure S24. Comparison of breakthrough simulations using RAST (continuous colored lines) and IAST (dashed lines) for CH_4/H_2O mixtures at a total fugacity = 500 kPa, and temperature 298 K. Three different values of %Relative Humidity are considered.

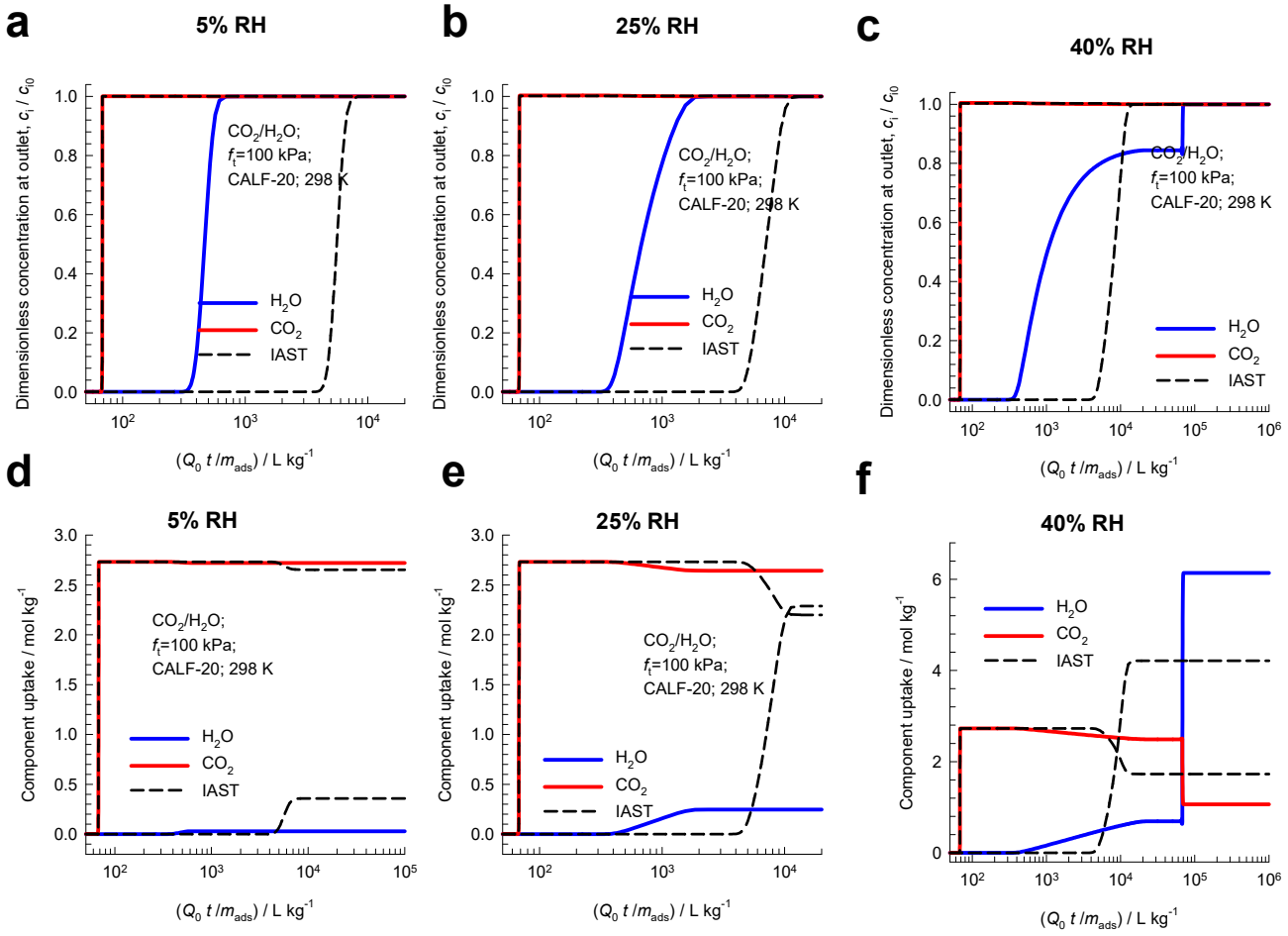

Figure S25. Comparison of breakthrough simulations using RAST (continuous colored lines) and IAST (dashed lines) for CO_2/H_2O mixtures at a total fugacity = 100 kPa, and temperature 298 K. Three different values of %Relative Humidity are considered.

8 Comparisons with RAST analysis of Kaur and Marshall

The manuscript of Kaur and Marshall[26] titled *The Real adsorbed solution theory model for the adsorption of CO2 from humid gas on CALF-20* is a preprint dated 17 November 2023 that has not been peer reviewed. The main focus of the Kaur-Marshall manuscript is on RAST modeling non-idealities in CO_2(1)/H_2O(2) mixture adsorption using published experimental data of Nguyen.[50]

We present below a critical analysis of the analysis of Kaur and Marshall[26] and compare with the results from this work, along with the results presented in our earlier publication[27] that used CBMC simulations of CO_2(1)/H_2O(2) mixture adsorption to provide fundamental reasons for the failure of the IAST.

8.1 Non-idealities for CO_2/H_2O mixture adsorption

The data on unary isotherms for CO_2, H_2O, and N_2 plotted in Figures 1, 2, 3 of Kaur and Marshall[26] in structured CALF-20 (80% MOF:20% polysulfone) are culled from literature sources. [44, 50, 52] The mixture adsorption data used in RAST modeling are determined from breakthrough experiments already reported in the published literature.[50] These breakthrough experiments of Nguyen [50] from which mixture adsorption data have been culled were not conducted under perfect isothermal conditions, corresponding to thermodynamic equilibrium. For the two highest values of %RH = 83%, and 92%, the H_2O loadings for mixture adsorption as plotted in Figure 5a of Kaur and Marshall exceed the unary H_2O isotherm data; see Figure S26; this characteristic cannot be modeled using the RAST. Consequently, the mixture adsorption data are not thermodynamically consistent. This has been clearly explained in the video presentation

Thermodynamic Non-Idealities in CO_2 Capture with CALF-20: Part VI

https://youtu.be/9tik1zuwo14

Noteworthily, RAST implementations of Kaur and Marshall,[26] using either the NRTL or Margules models also experience similar limitations at high values of %RH.

8.2 Non-idealities for CO_2/H_2O mixture adsorption: Dependence on %RH

The CBMC simulations for $CO_2(1)/H_2O(2)$ mixture adsorption as reported in this work in Figure S21 identifies two different regimes of thermodynamic non-idealities that prevail at low %RH and high %RH. The Kaur-Marshall preprint fails to recognize the two different regimes of thermodynamic non-idealities. In the Conclusions section, Kaur-Marshall state *It was demonstrated that RAST could reproduce the highly non-ideal binary adsorption of water/CO2 on CALF-20. The non-ideal behavior was a result of strong positive deviations from ideality. This is at odds with previous applications of RAST to adsorbing mixtures where both species exhibit Type I adsorption; for these cases negative deviations from ideality are the norm.*

In other words, Kaur-Marshall imply that thermodynamic non-idealities are the results of positive deviations from idealities. This is patently incorrect. In several published works on mixture adsorption in cation-exchanged zeolites [9, 10, 12, 14] it has been demonstrated that deviations from the IAST may also stem from negative deviations from thermodynamic non-idealities.

8.3 RAST modeling of CO_2/H_2O mixture adsorption

The RAST modeling of CO_2/H_2O mixture adsorption presented by Kaur ignores the correction factor for pore occupancies $\left(1-\exp\left(-C\Phi\right)\right)$, as emphasized in eq (S21); see also our earlier work.[27] The need for the correction factor $\left(1-\exp\left(-C\Phi\right)\right)$ in RAST modelling of CH_4/H_2O and CO_2/H_2O mixture adsorption has also been underscored by the data on $\frac{G^{ex}}{RT}=x_1\ln\left(\gamma_1\right)+x_2\ln\left(\gamma_2\right)$ plotted in Figure S12 and Figure S22. These data clearly demonstrate that the activity coefficients depend on both the surface potential, Φ, and the mole fractions of guest in the adsorbed phase, x_i. The RAST analysis of Kaur-Marshall ignore the dependence of activity coefficients on the surface potential, Φ. Consequently the activity coefficients reported by Kaur-Marshall do not obey the required limiting behaviors $\Phi\to 0;\quad \gamma_1\to 1;\quad \gamma_2\to 1$ as demanded by rigorous theories [13, 27] and confirmed by CBMC data in Figure S12 and Figure S22. This error in the Kaur-Marshall implementation has been highlighted in the video

presentation **Thermodynamic Non-Idealities in CO_2 Capture with CALF-20: Part II RAST modeling** available at https://youtu.be/ITmzyejlNXA

8.4 CO_2/N_2 mixture adsorption

In the analysis of Kaur and Marshall presented in their Figure 4 and Table 2, CO_2/N_2 mixture adsorption is treated as being non-ideal. The CBMC data in Figure S7 for CO_2/N_2 mixture adsorption show that this mixture behaves ideally. There is no evidence to suggest that non-ideality effects should be considered. See also **Thermodynamic Non-Idealities in CO_2 Capture with CALF-20: Part V** available at https://youtu.be/_bqQDBdd9x4

8.5 $CO_2/H_2O/N_2$ mixture adsorption

The CBMC simulations reported by Gopalsamy et al.[36] for $CO_2(1)/H_2O(2)/N_2(3)$ mixture adsorption in CALF-20 at 293 K and total fugacity 100 kPa are presented in Figure S27. The partial fugacity of $N_2(3)$ is held practically constant at the value of 80 kPa; the mole fraction of H_2O in the bulk gas mixture, y_2, is varied. The dashed lines are the IAST estimations; for this purpose, the unary isotherm fits used are those provided in Table S4. We note that the ternary mixture adsorption exhibits significant departures from thermodynamic idealities. Another way to demonstrate the non-idealities is to plot the mole fraction of guests in the adsorbed phase mixture, x_i, as a function of $\%\text{RH}$; see Figure S27b,c,d. We note that for $\%\text{RH} < 40\%$, the adsorbed phase mixture is richer in both CO_2 and N_2, i.e. poorer in H_2O, than is anticipated by the IAST. On the other hand, for $\%\text{RH} > 40\%$, the adsorbed phase mixture is poorer in both CO_2 and N_2, i.e. richer in H_2O, than is anticipated by the IAST.

The CBMC data of Gopalsamy et al.[36] can be matched with the set of NRTL parameters $C = 0.25 \text{ kg mol}^{-1}$; $\tau_{12} = 0.5; \tau_{21} = 2.55; \alpha_{12} = 0.363; \tau_{23} = 10; \tau_{32} = 15; \alpha_{23} = 0.287$. Noteworthily, since the binary $CO_2(1)/N_3(3)$ behaves ideally (cf. Figure S7), we assert that $\tau_{13} = 0; \quad \tau_{31} = 0$.

The RAST calculations for $CO_2/H_2O/N_2$ mixtures presented in Figure 7 of Kaur-Marshall are seriously flawed for two separate reasons. Firstly, these calculations ignore thermodynamic non-idealities for

N_2/H_2O mixture adsorption The molecular simulations presented in Figure S18 and Figure S27 clearly establish that N_2/H_2O mixture adsorption is analogous to CO_2/H_2O and subject to strong non-idealities. This point is also emphasized in the video presentation titled **Thermodynamic Non-Idealities in CO_2 Capture with CALF-20: Part III** available at https://www.youtube.com/watch?v=9nUjt9EK9ds.

8.6 List of Tables for Comparisons with RAST analysis of Kaur and Marshall

Table S4. Dual-site Langmuir-Freundlich parameters for CO_2 (1) and H_2O (2) determined from fitting unary isotherms determined at 293K from molecular simulations in CALF-20.[36] For calculation of the % Relative Humidity, the saturation vapor pressure of water, p_2^{sat}, at 293 K is determined from the Antoine equation; $p_2^{sat} = 2330$ Pa .The goodness of fits are quantified by the values of R^2.

	Site A			Site B		
	$\frac{q_{A,sat}}{\text{mol kg}^{-1}}$	$\frac{b_A}{\text{Pa}^{-\nu_A}}$	ν_A	$\frac{q_{B,sat}}{\text{mol kg}^{-1}}$	$\frac{b_B}{\text{Pa}^{-\nu_B}}$	ν_B
CO_2 $R^2 = 0.99966$	1.9	1.408E-11	2.15	3.3	3.194E-04	1
H_2O $R^2 = 0.997126$	10.8	2.095E-29	10.75	2.2	1.446E-04	1
N_2	2.8	2E-06	1			

8.7 List of Figures for Comparisons with RAST analysis of Kaur and Marshall

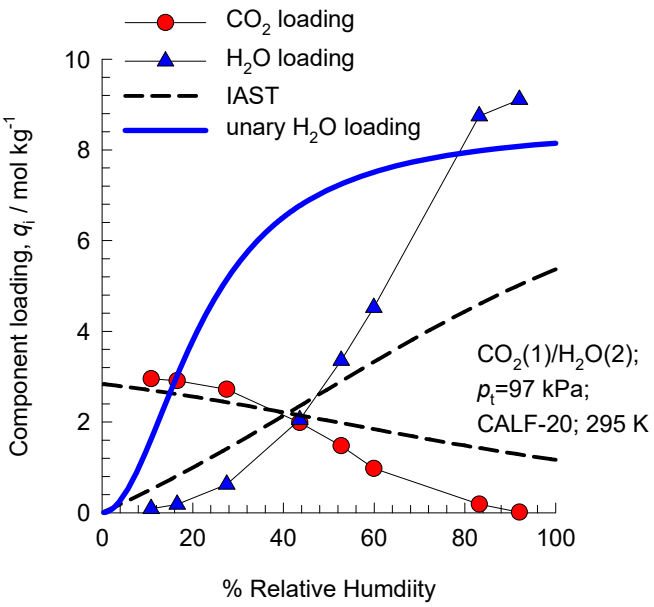

Figure S26. Experimental data of Lin et al.[52] (indicated by symbols) on component loadings for CO_2(1) and H_2O(2) mixture adsorption in structured CALF-20 (80% MOF:20% polysulfone) at 295 K. The total pressure in the bulk gas phase is 97 kPa with varying % relative humidity. The dashed lines are the IAST estimations; for this purpose, the unary isotherm fits are those provided in Table 1 of Kaur-Marshall.

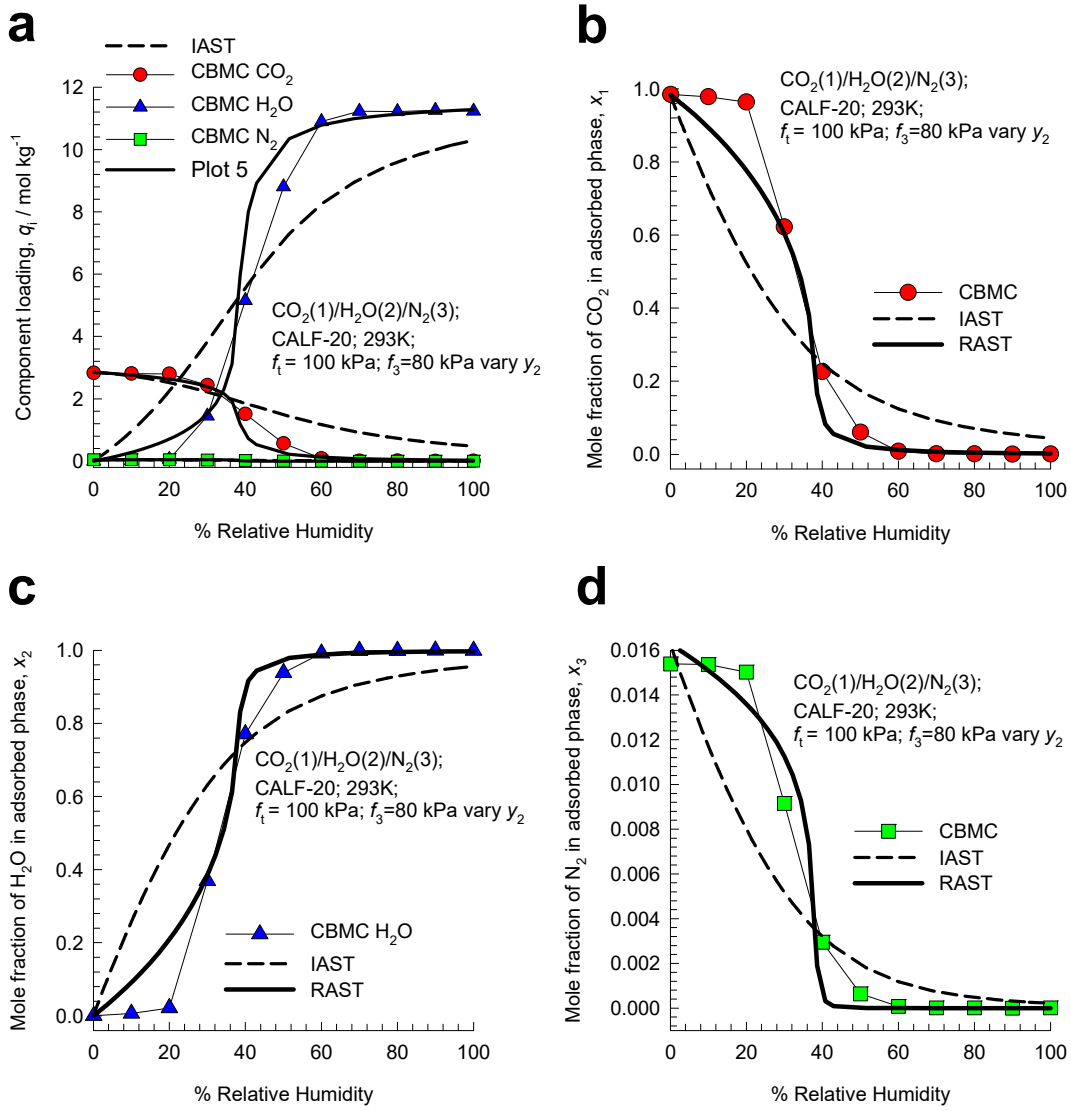

Figure S27. (a) CBMC simulations of component loadings, q_i, reported by Gopalsamy et al.[36] for CO2(1)/H2O(2)/N2(3) mixture adsorption in CALF-20 at 293 K at a total fugacity $f_t = f_1 + f_2 + f_3 = 100\ \text{kPa}$, and partial fugacity of N2(3) $f_3 = 80\ \text{kPa}$, of plotted as a function of %RH. The mole fraction of H2O in the bulk gas mixture, $y_2 = f_2 / f_t$, is varied. (b, c, d) Plot of the mole fractions of CO2, H2O, and N2 in the adsorbed phase mixture, x_i, as a function of %RH. The dashed lines are the IAST estimations. The continuous solid lines are the RAST estimations.

9 Nomenclature

Latin alphabet

A	surface area per kg of framework, $m^2\ kg^{-1}$
A_{12}, A_{21}	Margules parameters, dimensionless
b_i	Langmuir-Freundlich parameter, $Pa^{-\nu}$
c_i	molar concentration of species i, mol m^{-3}
c_{i0}	molar concentration of species i in fluid mixture at inlet to adsorber, mol m^{-3}
C	constant used in eq (S17), kg mol^{-1}
$Đ_i$	Maxwell-Stefan diffusivity for molecule-wall interaction, $m^2\ s^{-1}$
f_i	partial fugacity of species i, Pa
f_t	total fugacity of bulk gas phase mixture, Pa
G^{ex}	excess Gibbs free energy, J mol^{-1}
L	length of packed bed adsorber, m
m_{ads}	mass of adsorbent in packed bed, kg
n	number of species in the mixture, dimensionless
N_i	molar flux of species i with respect to framework, mol $m^{-2}\ s^{-1}$
p_2^{sat}	saturation vapor pressure of water, Pa
P_i^0	sorption pressure, Pa
q_i	component molar loading of species i, mol kg^{-1}
$q_{i,sat}$	molar loading of species i at saturation, mol kg^{-1}
q_t	total molar loading in mixture, mol kg^{-1}

$q_{sat,mix}$ saturation capacity of mixture, mol kg^{-1}

$\bar{q}_i(t)$ spatial-averaged component uptake of species *i*, mol kg^{-1}

Q_0 volumetric flow rate of gas mixture at inlet to fixed bed, m^3 s^{-1}

r radial direction coordinate, m

r_c radius of crystallite, m

R gas constant, 8.314 J mol^{-1} K^{-1}

%RH % relative humidity, dimensionless

$S_{ads} = \frac{q_1/q_2}{f_1/f_2}$ adsorption selectivity, dimensionless

t time, s

T absolute temperature, K

u superficial gas velocity in packed bed, m s^{-1}

v interstitial gas velocity in packed bed, m s^{-1}

x_i mole fraction of species *i* in adsorbed phase, dimensionless

y_i mole fraction of species *i* in bulk fluid mixture, dimensionless

z distance along the adsorber, m

T absolute temperature, K

Greek alphabet

α NRTL parameters, dimensionless

γ_i activity coefficient of component *i* in adsorbed phase, dimensionless

ε voidage of packed bed, dimensionless

Λ_{ij} Wilson parameters, dimensionless

μ_i molar chemical potential, J mol^{-1}

θ	fractional pore occupancy, dimensionless
ν	Freundlich exponent, dimensionless
π	spreading pressure, N m^{-1}
ρ	framework density, kg m^{-3}
τ_{ij}	NRTL parameters, dimensionless
Φ	surface potential, mol kg^{-1}

Subscripts

i	referring to component *i*
t	referring to total mixture
sat	referring to saturation conditions
0	referring to conditions at inlet to fixed bed

Superscripts

0	referring to pure component loading
ex	referring to excess parameter

10 References

(1) Peng, X.; Zhao, L.; Peng, Y.-L.; Deng, C.; Andaloussi, Y. H.; Pan, H.; Tian, Y.-J.; Zou, J.-S.; Krishna, R.; Liu, B.; Deng, C.; Xiao, P.; Sun, C.; Zaworotko, M. J.; Chen, G.; Zhang, Z. One-Step Ethylene Purification from a Seven-Component Cracking Gas Mixture with Sorbent-Sorbate Induced-fit. *CCS Chem.* **2024**, *xx*, xx. https://doi.org/10.31635/ccschem.024.202403977.

(2) Guo, X.-Z.; Li, B.; Xiong, G.-Z.; Lin, B.; Gui, L.-C.; Zhang, X.-X.; Qiu, Z.; Krishna., R.; Wang, X.; Yan, X.; Chen, S.-S. A stable ultramicroporous Cd-MOF with accessible oxygen sites for efficient separation of light hydrocarbons with high methane production. *Sep. Purif. Technol.* **2024**, *334*, 125987. https://doi.org/10.1016/j.seppur.2023.125987.

(3) Chen, Y.; Jiang, Y.; Li, J.; Hong, X.; Ni, H.; Wang, L.; Ma, N.; Tong, M.; Krishna, R.; Zhang, Y. Optimizing cask effect in multi-component natural gas purification with high methane productivity. *A.I.Ch.E.J.* **2024**, *70*, e18320. https://doi.org/10.1002/aic.18320.

(4) Zhang, Q.; Lian, X.; Krishna, R.; Yang, S.-Q.; Hu, T.-L. An ultramicroporous metal-organic framework based on octahedral-like cages showing high-selective methane purification from a six-component C1/C2/C3 hydrocarbons mixture. *Sep. Purif. Technol.* **2023**, *304*, 122312. https://doi.org/10.1016/j.seppur.2022.122312.

(5) Ruthven, D. M. *Principles of Adsorption and Adsorption Processes*. John Wiley: New York, 1984; pp 1-433.

(6) Myers, A. L.; Prausnitz, J. M. Thermodynamics of Mixed Gas Adsorption. *A.I.Ch.E.J.* **1965**, *11*, 121-130. https://doi.org/10.1002/aic.690110125.

(7) Talu, O.; Myers, A. L. Rigorous Thermodynamic Treatment of Gas-Adsorption. *A.I.Ch.E.J.* **1988**, *34*, 1887-1893.

(8) Siperstein, F. R.; Myers, A. L. Mixed-Gas Adsorption. *A.I.Ch.E.J.* **2001**, *47*, 1141-1159. https://doi.org/10.1002/aic.690470520.

(9) Krishna, R.; Van Baten, J. M. Elucidation of Selectivity Reversals for Binary Mixture Adsorption in Microporous Adsorbents. *ACS Omega* **2020**, *5*, 9031-9040. https://doi.org/10.1021/acsomega.0c01051.

(10) Krishna, R.; Van Baten, J. M. Using Molecular Simulations for Elucidation of Thermodynamic Non-Idealities in Adsorption of CO_2-containing Mixtures in NaX Zeolite. *ACS Omega* **2020**, *5*, 20535-20542. https://doi.org/10.1021/acsomega.0c02730.

(11) Krishna, R.; Van Baten, J. M. Water/Alcohol Mixture Adsorption in Hydrophobic Materials: Enhanced Water Ingress caused by Hydrogen Bonding. *ACS Omega* **2020**, *5*, 28393-28402. https://doi.org/10.1021/acsomega.0c04491.

(12) Krishna, R.; Van Baten, J. M. Investigating the Non-idealities in Adsorption of CO_2-bearing Mixtures in Cation-exchanged Zeolites. *Sep. Purif. Technol.* **2018**, *206*, 208-217. https://doi.org/10.1016/j.seppur.2018.06.009.

(13) Krishna, R.; van Baten, J. M. Fundamental Insights into the Variety of Factors that Influence Water/Alcohol Membrane Permeation Selectivity *J. Membr. Sci.* **2024**, *698*, 122635. https://doi.org/10.1016/j.memsci.2024.122635.

(14) Krishna, R.; Van Baten, J. M. How Reliable is the Ideal Adsorbed Solution Theory for Estimation of Mixture Separation Selectivities in Microporous Crystalline Adsorbents? *ACS Omega* **2021**, *6*, 15499–15513. https://doi.org/10.1021/acsomega.1c02136.

(15) Krishna, R.; van Baten, J. M. Hydrogen Bonding Effects in Adsorption of Water-alcohol Mixtures in Zeolites and the Consequences for the Characteristics of the Maxwell-Stefan Diffusivities. *Langmuir* **2010**, *26*, 10854-10867. https://doi.org/10.1021/la100737c.

(16) Krishna, R.; van Baten, J. M.; Baur, R. Highlighting the Origins and Consequences of Thermodynamic Nonidealities in Mixture Separations using Zeolites and Metal-Organic Frameworks. *Microporous Mesoporous Mater.* **2018**, *267*, 274-292. http://dx.doi.org/10.1016/j.micromeso.2018.03.013.

(17) Wilkins, N. S.; Rajendran, A. Measurement of competitive CO_2 and N_2 adsorption on Zeolite 13X for post-combustion CO_2 capture. *Adsorption* **2019**, *25*, 115-133. https://doi.org/10.1007/s10450-018-00004-2.

(18) Hefti, M.; Marx, D.; Joss, L.; Mazzotti, M. Adsorption Equilibrium of Binary Mixtures of Carbon Dioxide and Nitrogen on Zeolites ZSM-5 and 13X. *Microporous Mesoporous Mater.* **2015**, *215*, 215-228.

(19) van Zandvoort, I.; Ras, E.-J.; de Graaf, R.; Krishna, R. Using Transient Breakthrough Experiments for Screening of Adsorbents for Separation of C_2H_4/CO_2 Mixtures *Sep. Purif. Technol.* **2020**, *241*, 116706. https://doi.org/10.1016/j.seppur.2020.116706.

(20) van Zandvoort, I.; van der Waal, J. K.; Ras, E.-J.; de Graaf, R.; Krishna, R. Highlighting non-idealities in C_2H_4/CO_2 mixture adsorption in 5A zeolite. *Sep. Purif. Technol.* **2019**, *227*, 115730. https://doi.org/10.1016/j.seppur.2019.115730.

(21) Wang, Y.; LeVan, M. D. Adsorption Equilibrium of Binary Mixtures of Carbon Dioxide and Water Vapor on Zeolites 5A and 13X. *J. Chem. Eng. Data* **2010**, *55*, 3189-3195. https://doi.org/10.1021/je100053g.

(22) Talu, O.; Zwiebel, I. Multicomponent Adsorption Equilibria of Nonideal Mixtures. *A.I.Ch.E.J.* **1986**, *32*, 1263-1276.

(23) Sochard, S.; Fernandes, N.; Reneaume, J.-M. Modeling of Adsorption Isotherm of a Binary Mixture with Real Adsorbed Solution Theory and Nonrandom Two-Liquid Model. *A.I.Ch.E.J.* **2010**, *56*, 3109-3119.

(24) Mittal, N.; Bai, P.; Siepmann, I.; Daoutidis, P.; Tsapatsis, M. Bioethanol Enrichment using Zeolite Membranes: Molecular Modeling, Conceptual Process Design and Techno-Economic Analysis. *J. Membr. Sci.* **2017**, *540*, 464-476.

(25) Calleja, G.; Jimenez, A.; Pau, J.; Domínguez, L.; Pérez, P. Multicomponent Adsorption Equilibrium of Ethylene, Propane, Propylene and CO_2 on 13X Zeolite. *Gas Sep. Purif.* **1994**, *8*, 247-256.

(26) Kaur, H.; Marshall, B. D. Real adsorbed solution theory model for the adsorption of CO_2 from humid gas on CALF-20. *ChemRxiv* **2023**, 1-18. https://doi.org/10.26434/chemrxiv-2023-2cp2c.

(27) Krishna, R.; Van Baten, J. M. Elucidating the Failure of the Ideal Adsorbed Solution Theory for CO_2/H_2O Mixture Adsorption in CALF-20. *Sep. Purif. Technol.* **2025**, *352*, 128269. https://doi.org/10.1016/j.seppur.2024.128269.

(28) Krishna, R.; van Baten, J. M. In silico screening of metal-organic frameworks in separation applications. *Phys. Chem. Chem. Phys.* **2011**, *13*, 10593-10616. https://doi.org/10.1039/C1CP20282K.

(29) Krishna, R.; van Baten, J. M. In Silico Screening of Zeolite Membranes for CO_2 Capture. *J. Membr. Sci.* **2010**, *360*, 323-333. https://doi.org/10.1016/j.memsci.2010.05.032.

(30) Krishna, R.; van Baten, J. M. Describing Mixture Diffusion in Microporous Materials under Conditions of Pore Saturation. *J. Phys. Chem. C* **2010**, *114*, 11557-11563.

(31) Krishna, R.; van Baten, J. M. Diffusion of alkane mixtures in zeolites. Validating the Maxwell-Stefan formulation using MD simulations. *J. Phys. Chem. B* **2005**, *109*, 6386-6396.

(32) Krishna, R.; van Baten, J. M. Insights into diffusion of gases in zeolites gained from molecular dynamics simulations. *Microporous Mesoporous Mater.* **2008**, *109*, 91-108.

(33) Krishna, R. Describing the Diffusion of Guest Molecules inside Porous Structures. *J. Phys. Chem. C* **2009**, *113*, 19756-19781. https://doi.org/10.1021/jp906879d.

(34) Krishna, R. Diffusion in Porous Crystalline Materials. *Chem. Soc. Rev.* **2012**, *41*, 3099-3118. https://doi.org/10.1039/C2CS15284C.

(35) Mayo, S. L.; Olafson, B. D.; Goddard, W. A. DREIDING: A Generic Force Field for Molecular Simulations. *J. Phys. Chem.* **1990**, *94*, 8897-8909.

(36) Gopalsamy, K.; Fan, D.; S., N.; Magnin, Y.; Maurin, G. Engineering of an Iso-Reticular Series of CALF-20 MOF for CO_2 Capture. *ACS Appl. Eng. Mater.* **2024**, *2*, 96-103. https://doi.org/10.1021/acsaenm.3c00622.

(37) Ryckaert, J. P.; Bellemans, A. Molecular dynamics of liquid alkanes. *Faraday Discuss. Chem. Soc.* **1978**, *66*, 95-106.

(38) Dubbeldam, D.; Calero, S.; Vlugt, T. J. H.; Krishna, R.; Maesen, T. L. M.; Smit, B. United Atom Forcefield for Alkanes in Nanoporous Materials. *J. Phys. Chem. B* **2004**, *108*, 12301-12313.

(39) Harris, J. G.; Yung, K. H. Carbon Dioxide's Liquid-Vapor Coexistence Curve And Critical Properties as Predicted by a Simple Molecular Model. *J. Phys. Chem.* **1995**, *99*, 12021-12024.

(40) García-Sánchez, A.; Ania, C. O.; Parra, J. B.; Dubbeldam, D.; Vlugt, T. J. H.; Krishna, R.; Calero, S. Development of a Transferable Force Field for Carbon Dioxide Adsorption in Zeolites. *J. Phys. Chem. C* **2009**, *113*, 8814-8820. https://doi.org/10.1021/jp810871f.

(41) Horn, H. W.; Swope, W. C.; Pitera, J. W.; Madura, J. D.; Dick, T. J.; Hura, G. L.; Head-Gordon, T. Development of an improved four-site water model for biomolecular simulations: TIP4P-Ew. *J. Chem. Phys.* **2004**, *120*, 9665-9578. https://doi.org/10.1063/1.1683075.

(42) Murthy, C. S.; Singer, K.; Klein, M. L.; McDonald, I. R. Pairwise additive effective potentials for nitrogen. *Mol. Phys.* **1980**, *41*, 1387-1399.

(43) Makrodimitris, K.; Papadopoulos, G. K.; Theodorou, D. N. Prediction of permeation properties of CO_2 and N_2 through silicalite via molecular simulations. *J. Phys. Chem. B* **2001**, *105*, 777-788.

(44) Nguyen, T. T. T.; Lin, J.-B.; Shimizu, G. K. H.; Rajendran, A. Separation of CO_2 and N_2 on a hydrophobic metal organic framework CALF-20. *Chem. Eng. J.* **2022**, *442*, 136263. https://doi.org/10.1016/j.cej.2022.136263.

(45) Zhang, C.; Yang, X. Molecular dynamics simulation of ethanol/water mixtures for structure and diffusion properties. *Fluid Phase Equilib.* **2005**, *231*, 1-10.

(46) Krishna, R. Highlighting the Influence of Thermodynamic Coupling on Kinetic Separations with Microporous Crystalline Materials. *ACS Omega* **2019**, *4*, 3409-3419. https://doi.org/10.1021/acsomega.8b03480.

(47) Krishna, R. Metrics for Evaluation and Screening of Metal-Organic Frameworks for Applications in Mixture Separations. *ACS Omega* **2020**, *5*, 16987−17004. https://doi.org/10.1021/acsomega.0c02218.

(48) Krishna, R. Synergistic and Antisynergistic Intracrystalline Diffusional Influences on Mixture Separations in Fixed Bed Adsorbers. *Precision Chemistry* **2023**, *1*, 83-93. https://doi.org/10.1021/prechem.2c00003.

(49) Krishna, R. Fundamental Insights into Intra-Crystalline Diffusional Influences on Mixture Separations in Fixed Bed Adsorbers. *Chem Bio Eng.* **2024**, *1*, 53-66. https://doi.org/10.1021/cbe.3c00057.

(50) Nguyen, T. T. T.; Balasubramaniam, B. M.; Fylstra, N.; Huynh, R. P. S.; Shimizu, G. K. H.; Rajendran, A. Competitive CO_2/H_2O Adsorption on CALF-20. *Ind. Eng. Chem. Res.* **2024**, *63*, 3265-3281. https://doi.org/10.1021/acs.iecr.3c04266.

(51) Krishna, R. Occupancy Dependency of Maxwell−Stefan Diffusivities in Ordered Crystalline Microporous Materials. *ACS Omega* **2018**, *3*, 15743-15753. https://doi.org/10.1021/acsomega.8b02465.

(52) Lin, J.-B.; Nguyen, T. T. T.; Vaidhyanathan, R.; Burner, J.; Taylor, J. M.; Durekova, H.; Akhtar, F.; Mah, R. K.; Ghaffari-Nik, O.; Marx, S.; Fylstra, N.; Iremonger, S. S.; Dawson, K. W.; Sarkar, P.; Hovington, P.; Rajendran, A.; Woo, T. K.; Shimizu, G. K. H. A scalable metal-organic framework as a durable physisorbent for carbon dioxide capture. *Science* **2021**, *374*, 1464-1469. https://www.science.org/doi/abs/10.1126/science.abi7281.